

DISSERTATION  
submitted  
to the  
Combined Faculty for the Natural Sciences and Mathematics  
of  
Heidelberg University, Germany  
for the degree of  
Doctor of Natural Sciences

Put forward by

M. Sc. Andreea - Marieta Denițiu  
Born in: Sf. Gheorghe, Covasna, Romania

Date of the oral examination: .....



# Variational Methods for Discrete Tomography

Advisor 1: Prof. Dr. Stefania Petra  
Advisor 2: Prof. Dr. Christoph Schnörr



---

# ZUSAMMENFASSUNG

Die Rekonstruktion von Bildern anhand abgetasteter tomographischer Datenpunkte hat sich in vielen praktischen Situationen als allein stehendes Forschungsgebiet etabliert, wie etwa in den Bereichen der medizinischen Bildverarbeitung, der Seismologie, der Astronomie, der Flussanalyse, der industriellen Überprüfung und vielen anderen. Bestehende (kontinuierliche) Methoden scheitern daran das untersuchte Objekt korrekt zu modellieren. Daher untersuchen wir in dieser Arbeit diskrete tomographische Ansätze, welche zusätzliche Nebenbedingungen ermöglichen, die das zu analysierende Objekt besser beschreiben und somit das Endergebnis verbessern. Dabei legen wir einen besonderen Schwerpunkt auf die Annahmen der Abtastungs-Methodik des Signals, wofür wir uns mit dem kürzlich eingeführten Compressed Sensing (CS) Ansatz befassen, der zu bemerkenswerten Ergebnissen führte, abhängig davon, wie dünn besetzt das Signal ist. Allerdings lässt sich die Forschung im CS-Bereich nicht exakt auf alltägliche Probleme anwenden, weil angenommen wird, dass die Objekte, welche uns umgeben, stückweise konstant (und nicht automatisch dünn besetzt) sind. Darüber hinaus spiegeln, vom Standpunkt des CS, die Eigenschaften der Abtastungs-Matrix nicht die Bedingungen realer Datenerfassung wieder. Durch diese Mängel motiviert, untersuchen wir dünn besetzte Signale in einer gegebenen Darstellung, z.B. den Vorwärts-Differenzen Operator (Totale Variation) und entwickeln Rekonstruktions-Diagramme (Phasen-Übergänge) mit Hilfe linearer Programmierung, konvexer Analyse und Dualität, welche dem Anwender (mit Rücksicht auf die Sparsity) ermöglichen, den Typ des zu rekonstruierenden Objekts festzulegen, gegeben einer Menge von Erfassungsrichtungen. Ferner wird durch Hinzufügen verschiedener Störungen (entropisch, quadratisch) zum bereits eingeschränkten linearen Programm ein besonderer Augenmerk auf die Handhabung großer Datenmengen gelegt. In empirischen Bewertungen führten Störungen zu einer verbesserten Rekonstruktionsrate. Es ist unnötig zu sagen, dass das Thema dieser Arbeit durch indus-

---

trielle Anwendungen motiviert ist, bei denen der Datenerfassungsprozess auf maximal neun Kameras beschränkt ist und daher zu einem stark unterbestimmten inversen Problem führt.

---

# ABSTRACT

Image reconstruction from tomographic sampled data has contoured as a stand alone research area with application in many practical situations, in domains such as medical imaging, seismology, astronomy, flow analysis, industrial inspection and many more. Already existing algorithms on the market (continuous) fail in being able to model the analysed object. In this thesis, we study *discrete* tomographic approaches that enable the addition of constraints in order to better fit the description of the analysed object and improve the end result. A particular focus is set on assumptions regarding the signals' sampling methodology, point at which we look towards the recently introduced Compressive Sensing (CS) approach, that has shown to return remarkable results based on how sparse a given signal is. However, research done in the CS field does not accurately relate to real world applications, as objects usually surrounding us are considered to be piecewise constant (not sparse on their own) and the properties of the sensing matrices from the viewpoint of CS do not reflect real acquisition processes. Motivated by these shortcomings, we study signals that are sparse in a given representation, e.g. the forward-difference operator (total variation) and develop reconstruction diagrams (phase transitions) with the help of linear programming, convex analysis and duality that enable the user to pin-point the type of objects (with regard to their sparsity) which can be reconstructed, given an ensemble of acquisition directions. Moreover, a closer look is given to handling large data volumes, by adding different perturbations (entropic, quadratic) to the already constrained linear program. In empirical assessments, perturbation has lead to an increased reconstruction rate. Needless to say, the topic of this thesis is motivated by industrial applications where the acquisition process is restricted to a maximum of nine cameras, thus returning a severely undersampled inverse problem.



---

# ACKNOWLEDGEMENT

PhD time... a period which is seen with different eyes by people: i) those which are not pursuing this step in their life and that consider this to be a big waste of time and energy and ii) those that decide to follow this academic path and struggle with it for a given period of time, time in which they find themselves reaching their limits and beyond (intellectually and mentally).

My entry point in the research area was offered by Prof. Dr. Ing. Christoph Schnörr, my current PhD supervisor. The patience, advice and moral sustain I received from my supervisor and colleagues are uncountable. One memorable moment sticks to my mind. In an usual report meeting, the supervisor says towards me: "Are you disappointed with your work? You shouldn't. You did your best, the method does not work, we just have to orient to some other viewpoint and try again." It was a whole new attitude, to see that people can make mistakes and are not downgraded and put down for it. Many special thanks for this and for being more than just "a supervisor".

Guidance in my research domain is also very much appreciated and deep acknowledgements are oriented towards Prof. Dr. Stefania Petra. Likewise, for a whole bunch of patience and numerous answered e-mails late at night with maybe "routine" questions, trying to better understand this field.

Special collaboration with Hochschule Muenchen, through a very special person, Prof. Dr. Ing. Claudius Schnörr, is kindly recognized. From the "colleagues of suffering" category, thanks go to: Johannes Berger, my office colleague, for baring with me for so many years, given my different mood swings and childish behaviour; also for feeding me with jellos and soft cakes when my sugar count went very low and most importantly, helping with some mathematical issues and german language; Florian Becker, a mentor in crafting doctor hats and swimming activities; Fabian Rathke, Bernhard Schmitzer, Borislav Antic and Eva-Maria Didden, for integrating me in the first RTG generation and numerous

---

sport activities; Joerg Kappes and Paul Swoboda for their last 100 m interest in tomography which gave them a boost in their publication number and that eventually lead to a helpful feedback regarding my thesis content; the second RTG generation: Ecaterina Bodnariuc, Tabea Zuber, Mattia Desana, Robert Dalitz, Vera Trajkovska, Matthias Zisler, for the fresh breeze and always laughing and looking optimistic attitude (since they still have a while until they reach the end of their PhD) and of course, the beloved and always there when it came to real-life problems, out of the academia bubble: Barbara Werner and Evelyn Wilhelm.

Last, but not least, heartfelt thanks go out to my family members which guided me through advices and warmth when things got rough. Thank you for being there, although at times, distance really was a downside.

Funding by the "Bavarian State Ministry of Education, Science and the Arts" is gratefully acknowledged.

---

## LIST OF FIGURES

2.1	Convex sets . . . . .	7
2.2	Non-convex sets . . . . .	8
2.3	Different subgradients $g_1, g_2$ of the function $f$ . . . . .	11
2.4	Graphical illustration of the conjugate function. . . . .	12
2.5	Synthesis model . . . . .	21
2.6	Analysis model . . . . .	22
2.7	Example of a left regular bipartite graph with left degree 2. . . . .	23
2.8	<b>Left:</b> Undirected graph with 6 vertices and 5 edges. <b>Right:</b> Weighted directed graph. . . . .	26
2.9	Example of graphs with three connected components. . . . .	27
2.10	Example of a cut of a $3 \times 3$ image . . . . .	29
2.11	Cross-section through an object in the x-y plane. . . . .	31
2.13	Absorption processes introducing noise in tomography. . . . .	33
2.12	Exponential decrease of the X-ray intensity. . . . .	34
2.14	Acquisition geometry for first and second type generation of CT scanners. . . . .	35
2.15	Acquisition geometry for third and fourth type generation of CT scanners. . . . .	36
2.16	The Radon transform at a given angle $\theta$ and distance $\rho$ . . . . .	37
2.17	Interpolation schemes for modelling tomographic measurements . . . . .	39
2.18	Algebraic reconstruction technique for a $3 \times 3$ matrix . . . . .	41
2.19	ART methods . . . . .	45
2.20	SIRT methods . . . . .	46
2.21	Motorcycle engine cylinder <sup>1</sup> : 3D visualisation of whole and cut tomogram . . . . .	47
2.22	Motorcycle engine cylinder <sup>2</sup> : 3D CAD visualisation . . . . .	47

2.23	Motorcycle engine cylinder <sup>3</sup> : <b>Left</b> : CAD visualization - X cross section, <b>Right</b> : CAD visualization - Z cross section. . . . .	47
3.1	Class of compound bodies to test our reconstruction algorithms . . . . .	49
3.2	Eight different projecting directions . . . . .	53
3.3	Imaging set-up for three orthogonal projections of a cube. . . . .	53
3.4	Imaging set-up for four projecting directions . . . . .	54
3.5	Bivariate Haar-transformed nullspace basis vector along with its nullspace vector. . . . .	56
3.6	Edge sets $\Lambda$ that belong to the maximizers of $ \Lambda $ among all subsets $V(\Lambda) \subseteq V$ with fixed $s =  V(\Lambda) $ . . . . .	59
3.7	The bounds (3.20a) and (3.20b) shown in the left and right panel respectively, as dashed lines, for $d = 10$ , as a function of $\ell$ . . . . .	60
3.8	Random images with varying cosparsity $\ell = p - k$ in 2D . . . . .	65
3.9	Random images with varying cosparsity $\ell = p - k$ in 3D . . . . .	66
3.10	Phase transitions for the unperturbed matrix $A$ , 2D case, 3, 4, 5 and 6 projecting directions with unknown and known cosupport . . . . .	70
3.11	Phase transitions for the perturbed matrix $\tilde{A}$ , 2D case, 3, 4, 5 and 6 projections, with unknown and known cosupport . . . . .	71
3.12	Empirical probability of exact recovery by total variation minimization (3.7) via the unperturbed and perturbed matrices from Section 3.1.1, for $d = 31$ . . . . .	72
3.13	Empirical probability of exact recovery by total variation minimization (3.7) via the unperturbed and perturbed matrices from Section 3.1.1, for $d = 41$ . . . . .	73
3.14	Log-log plot of phase transitions in 3D for the unperturbed matrix $A$ and perturbed matrix $\tilde{A}$ for 3 and 4 projecting directions . . . . .	74
4.1	Phase transitions 2D, with MOSEK and our perturbed dual. . . . .	82
4.2	Comparison between the quadratic perturbation approach and entropic perturbation approach . . . . .	83
4.3	Experimental finite perturbation property of the entropic approach . . . . .	83
4.4	Phase transitions for the 3D case, with 3,4 cameras solving the entropic perturbed dual. . . . .	84
4.5	Slices through the 3D volume of an original Shepp-Logan image and the reconstructed image from 7 <i>noisy</i> projecting directions via the entropic perturbation approach . . . . .	85
4.6	Comparison between computation times of the proposed approach and MOSEK. . . . .	85
4.7	Graphical illustration of the residual along the computation lines of the Douglas-Rachford, FISTA and Chambolle-Pock algorithms. . . . .	87
4.8	Alternating continuous-discrete reconstruction of a cube with 2 gray levels . . . . .	94

## List of Figures

---

4.9	Alternating continuous-discrete reconstruction of a cube with 4 gray levels . . . . .	95
4.10	Alternating continuous-discrete reconstruction of a piston with 2 gray levels . . . . .	96
4.11	Alternating continuous-discrete reconstruction of 3D Shepp-Logan with 5 gray levels . . . . .	96
5.1	Illustration of taut-string method . . . . .	103
5.2	Structure aware regularization, considering separate minimization problems for gradient directions and for projection directions . . .	104



---

# LIST OF TABLES

2.1	Comparison of analytical vs. iterative reconstruction methods. . .	40
3.1	Dimensions of projection matrices in 2D. . . . .	52
3.2	The scaling factors of the theoretical curves (3.21a) and (3.22a) for known and unknown cosupport respectively. . . . .	68
3.3	The scaling factors of the theoretical curves (3.21b) and (3.22b) for known and unknown cosupport respectively. . . . .	68
4.1	Summary of the functions used in algorithms presented in Sect. 2.1.1.4. . . . .	86
4.2	Algorithm comparison: FISTA, DR, CP and our routines. . . . .	89
4.3	Parameters used for the discrete optimization routine, that enable accurate reconstruction. . . . .	94



---

# NOTATION

$\mathbb{N}$	Natural numbers, $0 \notin \mathbb{N}$ .
$\mathbb{R}$	Real numbers.
$\mathbb{R}_{\geq 0}$	Real numbers with only positive entries.
$[n] := \{1, 2, \dots, n\}$	Arbitrary set.
$[J]^c := [n] \setminus J$	Complement set $[J]^c$ for $J \subseteq [n]$ .
$[n]_0 := \{0, 1, \dots, n-1\}$	Another example of a set.
$ J $	Cardinality of a set, i.e. the # of elements it comprises.
$x$	Scalar value.
$\mathbf{x} := (x_1, \dots, x_n)^\top$	Vector, usually $\mathbf{x} \in \mathbb{R}^n, n \in \mathbb{N}$ .
$\mathbf{0} := (0, \dots, 0)^\top$	Vector containing only values of 0.
$\mathbf{1} := (1, \dots, 1)^\top$	Vector containing only values of 1.
$\mathbf{e}_i := (0, \dots, 0, 1, 0, \dots, 0)$	Vector with $i$ -th component 1 and 0 otherwise.
$\langle \mathbf{a}, \mathbf{b} \rangle := \mathbf{a}^\top \mathbf{b} = \sum_{i=1}^n a_i b_i$	Scalar product of two vectors $\mathbf{a}$ and $\mathbf{b}$ .
$\ \mathbf{x}\ _p := \sqrt[p]{\sum_{i=1}^n  x_i ^p}$	$p$ -norm of a vector $\mathbf{x}$ , $p \geq 1, p \in \mathbb{R}$ .
$\ \mathbf{x}\ _0 := \{i : x_i \neq 0\}$	Number of nonzero elements in $\mathbf{x}$ .
$\ \mathbf{x}\ _1 := \sum_{i=1}^n  x_i $	Manhattan norm.
$\ \mathbf{x}\ _2 := \sqrt{x_1^2 + \dots + x_n^2}$	Euclidean norm.
$\ \mathbf{x}\ _\infty := \max  x_1^2 , \dots,  x_n^2 $	Infinity norm.
$A := \begin{pmatrix} a_{11} & \cdots & a_{1n} \\ \vdots & & \vdots \\ a_{m1} & \cdots & a_{mn} \end{pmatrix}$	Matrix, $A \in \mathbb{R}^{m \times n}, m, n \in \mathbb{N}, a_{ij} \in \mathbb{R}, \forall i, j$ .

---

$\text{diag}(\mathbf{a}) := \begin{pmatrix} a_1 & 0 & \dots & 0 \\ 0 & a_2 & \dots & 0 \\ \vdots & \vdots & \ddots & \vdots \\ 0 & 0 & \dots & a_n \end{pmatrix}$	Diagonal matrix.
$B_\Lambda$	The submatrix of $B$ formed by the rows indexed by the set $\Lambda$ .
$B^\Lambda$	The submatrix of $B$ formed by the columns indexed by the set $\Lambda$ .
$\mathcal{N}(B)$	Denotes the nullspace of $B$ .
$\eta(i)$	Denotes the neighbourhood of vertex $i$ .
$\otimes$	Kronecker product.
$\mathbb{R}_+$	Set of all nonnegative real numbers.
$\mathbb{R}_{++}$	Set of all strictly positive real numbers.
$S_\lambda(x) = \begin{cases} x + \lambda, & x < -\lambda; \\ 0, & -\lambda < x < \lambda; \\ x - \lambda, & \lambda < x. \end{cases}$	Soft thresholding operator.
$\mathcal{F}_L^{1,1}(\mathbb{R}^n)$	Class of real continuously differentiable convex functions with Lipschitz continuous gradient $\mathcal{L}$ .
$\mathcal{F}_0(\mathbb{R}^n)$	Class of proper, closed, convex functions.

---

# CONTENTS

<b>Zusammenfassung</b>	<b>III</b>
<b>Abstract</b>	<b>V</b>
<b>Acknowledgement</b>	<b>VII</b>
<b>List of Figures</b>	<b>VIII</b>
<b>List of Tables</b>	<b>IX</b>
<b>Notation</b>	<b>XI</b>
<b>1 Introduction</b>	<b>1</b>
1.1 Motivation . . . . .	1
1.2 Related Work . . . . .	3
1.3 Contribution . . . . .	4
1.4 Outline . . . . .	5
<b>2 Background</b>	<b>7</b>
2.1 Mathematical Background . . . . .	7
2.1.1 Convex Analysis and Programming . . . . .	7
2.1.1.1 Convex Functions . . . . .	9
2.1.1.2 Subgradients and Conjugates . . . . .	11
2.1.1.3 Fenchel Duality . . . . .	13
2.1.1.4 Convex Programs with Linear Constraints . . . . .	14
2.1.2 Compressed Sensing . . . . .	17
2.1.2.1 Compressed Sensing . . . . .	18
2.1.2.2 Sparsity versus Cosparsity . . . . .	20
2.1.2.3 Theoretical Recovery Guarantees . . . . .	22

2.1.3	Graphical Models and Segmentation . . . . .	25
2.1.3.1	Elements of Graph Theory . . . . .	26
2.1.3.2	Graph-Cuts . . . . .	27
2.2	Computed Tomography . . . . .	30
2.2.1	Established CT . . . . .	32
2.2.1.1	Physics of CT . . . . .	32
2.2.1.2	Imaging Modalities . . . . .	33
2.2.2	Discretization and Basic Recovery Schemes . . . . .	35
2.2.2.1	Filtered Back-Projection . . . . .	35
2.2.2.2	Algebraic Reconstruction Technique . . . . .	37
2.2.3	Discrete Tomography . . . . .	39
2.2.3.1	Algebraic Reconstruction Technique . . . . .	39
2.2.3.2	Simultaneous Iterative Reconstruction Technique . . . . .	42
2.2.3.3	(Soft) Discrete Algebraic Reconstruction Technique . . . . .	43
2.2.3.4	Maximum a Posteriori X-ray Computed Tomography Using Graph Cuts . . . . .	43
2.2.4	Applications in Industry (Non-Destructive Testing) . . . . .	44
<b>3</b>	<b>Correct Recovery and Phase Transitions</b>	<b>49</b>
3.1	Tomographic Sensing Matrices . . . . .	51
3.1.1	Imaging Set-Up . . . . .	52
3.1.2	Application to Considered Scenarios . . . . .	54
3.2	Sparsity and TV-Based Reconstruction . . . . .	55
3.3	Cosparsity and TV-Based Reconstruction . . . . .	57
3.3.1	Basic Uniqueness Results . . . . .	57
3.3.2	Application to the Analysis Operator $\nabla$ . . . . .	58
3.4	Recovery by Linear Programming . . . . .	61
3.5	Numerical Experiments . . . . .	64
3.5.1	Set-Up . . . . .	64
3.5.2	Optimization . . . . .	66
3.5.3	Phase Transitions . . . . .	67
3.5.4	Discussion . . . . .	68
3.6	Conclusion . . . . .	69
<b>4</b>	<b>Recovery Algorithms: Perturbed Dual Approach</b>	<b>75</b>
4.1	TV-Recovery by Linear Programming . . . . .	76
4.1.1	Primal Linear Program and its Dual . . . . .	76
4.1.2	Uniqueness of Primal LP . . . . .	77
4.2	Recovery by Perturbed Linear Programming . . . . .	78
4.2.1	Entropic Perturbation and Exponential Penalty. . . . .	78
4.2.2	Quadratic Perturbation . . . . .	81
4.2.3	Numerical Experiments . . . . .	82

4.3	Algorithm Comparisons . . . . .	86
4.4	Continuous / Discrete Interplay . . . . .	89
4.4.1	Continuous minimization . . . . .	89
4.4.2	Discrete minimization . . . . .	91
4.4.3	Numerical Experiments . . . . .	93
4.5	Conclusion . . . . .	95
<b>5</b>	<b>Nearly Isotropic Priors and Problem Splitting</b>	<b>99</b>
5.1	Approach . . . . .	99
5.1.1	Minimizing gradient directions . . . . .	101
5.1.2	Minimizing projection directions . . . . .	102
5.2	Numerical Experiments . . . . .	103
<b>6</b>	<b>Conclusion</b>	<b>105</b>



---

---

# CHAPTER 1

---

## INTRODUCTION

### 1.1 Motivation

Industry thrives. Product demand increases daily and detail, accuracy and speed are the main sought-after words in the current market. Whether we talk about material science, medical applications, seismology, astrophysics or archaeology, tomography plays an important role. Although its use in these areas are rather recent, except in the medical field, the method is becoming increasingly popular due to its non-invasive properties.

As a general definition, tomography is an imaging modality that acquires cross-sections of an object, through means of various penetrating waves that interact with the media comprising the object:

1. ultrasound tomography - sound waves;
2. optical coherence tomography - light waves;
3. computed tomography - X-rays;
4. single photon emission computed tomography -  $\gamma$ -rays;
5. magnetic resonance imaging - radio frequency waves;
6. positron emission tomography - positron-emitting tracer;
7. hydraulic tomography - fluid flow.

This thesis focuses its work in the field of Computed Tomography.

Because media differ in densities, recorded images may have either a clear display of the object (regions are sharp, perfectly contoured, no ambiguities) or can be damaged by artefacts (beam hardening, metal, ringing or motion artefacts), thus diminishing their practical usefulness. The absorption coefficients that are in a one to one connection with densities of each media, i.e. the amount of energy that can be absorbed from the incoming wave, are the quantities that need to be

retrieved from already existing tomographic measurements. The process of recovering these absorption coefficients is a highly *ill-posed* linear inverse problem.

Ill-posedness of the problem stems from i) the limited number of projections that can be taken and/or ii) the low range of angles from which the object can be viewed from. These limitations may occur either because of strict requirements on the structural behaviour of the object that need to be met, either by the fact that there simply is not enough space or financial possibilities to create the "perfect" setup.

From a mathematical point of view, these short-comings can be tackled by: i) restricting the space of solutions ( [4, 5] ) and ii) adding a regularizer to the objective function, based on some additional a-priori knowledge ( [116, 114, 73, 102, 105, 106] ).

Solutions that are currently implemented on the market employ continuous reconstruction methods, which have the deficit of requiring a high amount of data in order to deliver plausible results. Common approach in signal recovery is to sample the continuous signal at a given rate and then try to reconstruct it from its discrete measurements. Up to a recent time, the only guarantees to assure perfect signal reconstruction was by using the Shannon-Nyquist sampling theorem, which states that *given a perfectly band limited signal with a bandwidth  $f$ , it is possible to accurately reconstruct it by acquiring samples at discrete times, as long as the sampling rate is greater or equal than twice the frequency of the signal, i.e.  $2f$* . This however, leads to a huge amount of data to be acquired and for signals with a very high bandwidth, proper signal processing turns out to be expensive, due to storage and computation requirements.

Recently, a new paradigm of signal sampling has emerged, named *Compressive Sensing (CS)* [20, 16, 35]. It relies on the low complexity property of the signals, e.g. they are sparse, possibly after transformation to a suitable basis, like e.g. wavelets, and it is seen as an attractive alternative to handling high bandwidth signals, compared to the Shannon-Nyquist procedure. Research done in this area [21] tried to relate the number of measurements to the signals' sparsity, such that accurate reconstruction can be achieved. However, assumptions on the sensor's properties are quite strong and the theory behind Compressive Sensing seems not to be suitable for practical applications, such as it is the case in this thesis.

Motivated by industrial applications concerning non-destructive quality inspection testing, e.g. [23, 58], we focus on the reconstruction of compound solid bodies in 2 and 3 dimensions, where the underlying assumption is that they are *piecewise constant*. That is, we look into the problem of reconstructing discrete signals with a sparse range, comprising more than two but not too many gray levels, in the area of Computed Tomography, keeping a close relation to Compressive Sensing theory. Our objective is to relate the required number of measurements per object complexity, given that standard CS assumptions do not hold and to establish sampling rates that enable perfect reconstruction of signals.

## 1.2 Related Work

Recent work illustrates that the focus of corresponding research in *compressed sensing (CS)* is shifting - in contrast to discrete tomography [63] - from a *worst-case analysis* [56] towards an *average-case analysis* [79, 80, 64]. As for many other difficult combinatorial problems, the probabilistic approach is a plausible, and often the only possible way, to make well-founded statements that go beyond idealistic mathematical assumptions and that are also relevant for real-world applications. Theoretical recovery guarantees, expressed as thresholds on the critical parameters, relate the solution sparsity to the solution degrees of freedom and to the number of measurements.

In the work of Donoho and Tanner [40], a thorough analysis is performed - under the aforementioned strong assumptions on the sensor - to determine the *universality* of these thresholds, presented as phase transitions, with regard to different optimization problems occurring in data and signal processing. Among cases considered for analysis, lies also the problem of reconstructing a signal  $x$  from its random Fourier coefficients. In effect, they construct the phase transition by solving numerous instances of the  $\ell_1$  minimization problem on  $x$ , subject to equality constraints. Moreover, they tie the connection between these phase transitions and applications in combinatorial geometry, as the face counts of a convex polytope are in strong connection with the probability of accurately reconstructing a sparse vector, by solving a linear program (LP). For more work on the subject of sparse solution recovery by solving underdetermined systems of linear equations using LPs with random polytopes, we refer the reader to the papers [39, 41, 36].

Another perspective of phase transitions in convex programs is given by Amelunxen et. al. [1]. They solve the same minimization problem,  $\ell_1$  applied to the signal, directly, and relate the optimality conditions of the convex program to the notion of statistical dimension of descent cones, using Gaussian sensing matrices.

In discrete tomography, however, images to be reconstructed are sampled along lines. Thus, sampling patterns are quite different from random and non-adaptive measurements that are favourable from the viewpoint of Compressed Sensing. In [94], it has been showed that structured sampling patterns as used in commercial *computed tomography (CT)* scanners do not satisfy the CS conditions, like the *nullspace property* and the *restricted isometry property (RIP)*, that guarantee accurate recovery of sparse (or compressible) signals. In fact, these recovery conditions predict a quite poor worst-case performance of tomographic measurements, due to the high nullspace sparsity of a tomographic projection matrix  $A$ . Moreover, the gap between available *worst-case* recovery results of CS [42] and *worst-case* results from tomographic projections in [94] is dramatic.

In [96, 95], an average-case relation between image sparsity and sufficient number of measurements for recovery was presented, and it was also showed that the

transition from non-recovery to recovery is sharp for specific sparse images. The analysis is based on the non-negativity of the coefficient matrix and of the signal itself and utilizes new mathematical tools from CS via expander graphs.

In Jorgensen et.al. [69], empirical findings on an average-case relation between image sparsity and the adequate number of measurements in a fan-beam CT setting are reported. The analysis is performed on images that are "sparse" in the image domain and is based on solving a series of  $\ell_1$  minimization problems subject to equality constraints, for varying sparsity levels. Results are presented as *phase transitions*, revealing a fine crossing between recoverable and non-recoverable images.

Empirical evidence for the recovery of *piecewise constant* functions from few tomographic measurements was already observed in [105, 62, 68]. The first theoretical guarantees that have been obtained for recovery from noiseless samples of images with exactly sparse gradients via total variation minimization, date back to the beginnings of CS [21, 20]. However, the measurements considered were incomplete Fourier samples, and images were not sampled along lines in the spatial domain, but along few radial lines in the frequency domain. Such measurements ensembles are known to have good CS properties as opposed to the CT setup, and are almost isometric on sparse signals for a sufficient number of samples. As a result, recovery is stable in such scenarios. Stable recovery of the image gradient from incomplete Fourier samples was shown in [93], while Needell [91] showed that stable image reconstruction via total variation minimization is possible also beyond the Fourier setup, provided the measurement ensemble satisfies the RIP condition.

## 1.3 Contribution

Earlier work done in the field of tomography and compressive sensing have focused on signal reconstruction based on  $\ell_1$  minimization problems, considering only signal sparsity priors. The focus of our work relies on objects which have a *sparse gradient* representation. This led to the development of currently presented routines and the theoretical analysis of tomographic image reconstruction based on total variation and gradient sparsity priors. The main contributions of the thesis are:

- Theoretical bounds on the required number of measurements necessary for accurate signal reconstruction, by adopting the *cosparse analysis model* and relying on the viewpoint that measurement matrices in tomography can be modelled as adjacency matrices of expander graphs.
- Phase transitions for Total Variation in Compressive Sensing.

- Two algorithmic approaches to accurately recover a signal from undersampled data, using duality theory and anisotropic total variation minimization subject to linear and non-negativity constraints. We consider additional perturbations (entropic, quadratic) to the primal objective function, in order to obtain an unconstrained and differentiable dual problem, that is easier to solve.
- Model the tomographic problem as a graphical model, considering image pixels as unary terms and pixel neighborhood as pairwise terms, and solve it using duality, by an iterative method (L-BFGS) and Graph Cuts.
- The concept of splitting the reconstruction problem according to projection and gradient directions. This led to the development of the approach mentioned in Sect. 5. No requirement on the number of gray levels is required, the method is highly parallelizable and it involves solving smaller easier problems such as least squares and proximal operators.

## 1.4 Outline

**Chapter 2** summarizes important aspects on convex analysis, compressed sensing and graphical models, to sustain the mathematics involved in the upcoming chapters. Likewise, introductory notions about Computed Tomography are mentioned in the second part of this chapter. They range from the physics behind the acquisition process, up to existing methodologies in reconstructing tomographic signals, from a continuous and discrete point of view.

In **Chapter 3** we start with a short presentation of the imaging set-up considered in all work encountered in this thesis (unless stated otherwise) and further in, we employ the concept of signal *cosparsity* together with notions of expander graphs to derive lower bounds on the required number of measurements for signal reconstruction, using total variation, linear programming and non-negativity priors.

**Chapter 4** addresses the problem of tomographic signal reconstruction by considering perturbed (entropic, quadratic) linear programs, in such a way that the dual becomes unconstrained and differentiable, thus easing the mathematical problem to be solved. These approaches are suitable for large-scale optimization problems, where the stand-alone solvers such as MOSEK or CPLEX fail, due to the high-dimensionality of the signal. Moreover, in Sect. 4.3 we conduct an experiment meant to compare well-known algorithms used in practice for solving linear constrained problems with the routines we developed up to this point in the thesis. We conclude in Sect. 4.4 with a routine that looks to blend a continuous approach and a discrete minimization step, in order to handle large data volumes.

Lastly, **Chapter 5** considers a splitting approach of the tomographic problem. Disentangling the projection and gradient directions as mentioned in the paper of [110] and using  $\ell_1$  minimization, we obtain a convex objective function which is known to have a global optimum. In effect, we end up solving smaller problems (least squares, proximity operators) that can be easily parallelizable.

We conclude in **Chapter 6** with a final discussion.

---

---

# CHAPTER 2

---

## BACKGROUND

The content of this chapter oversees mathematical definitions and concepts of convex theory, compressive sensing, graph theory, as well as fundamental notions regarding computed tomography and imaging sensors, thus offering the reader elementary tools and notions to ease the comprehension of the present thesis.

### 2.1 Mathematical Background

#### 2.1.1 Convex Analysis and Programming

In every mathematical research domain, there is a high possibility to encounter an optimization problem, where one wants to find the optimum solution of his model. By expressing the objective function in terms of *convex* functions, the minimization problem is simplified due to the property of convex functions that the *local optimum* is actually the *global optimum* of the objective function. The notion of convexity in terms of sets is illustrated in Fig. 2.1 and Fig. 2.2.

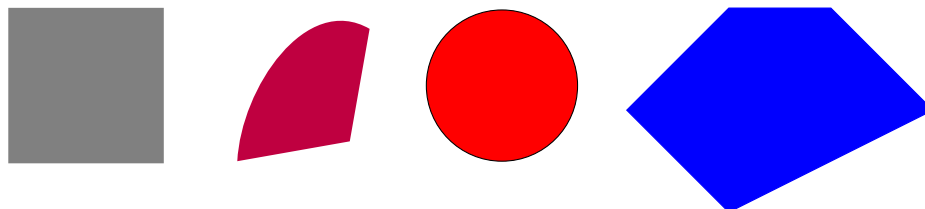


Figure 2.1: Convex sets

That is, considering any 2 points belonging to the set, every other point lying

on the segment that connects these end points have to lie in the same set. Note that this is valid even for *non-closed* sets.

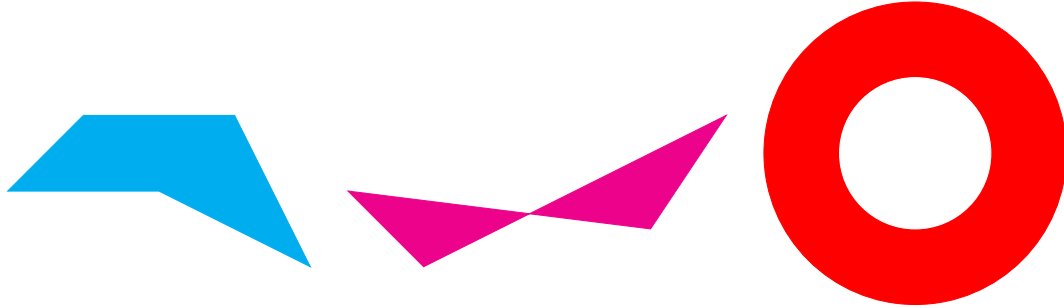


Figure 2.2: Non-convex sets

**Definition 1** (Convex set). *A subset  $C$  of  $\mathbb{R}^n$  is said to be convex if*

$$(1 - \lambda)x + \lambda y \in C,$$

*whenever  $x, y \in C$  and  $0 \leq \lambda \leq 1$ .*

Convexity is kept under addition, scaling and intersection [12]. We mention a few well known examples of convex sets:

- the  $(n - 1)$ - dimensional simplex generated by  $\{e^1, \dots, e^n\}$ , known also as the **probability simplex**

$$\Delta_n = \{x \in \mathbb{R}^n : x \geq 0, \langle \mathbf{1}, x \rangle = 1\},$$

with  $e^i$  the canonical unit vectors.

- **half-spaces**,  $H = \{x : a^\top x \leq b\}$ . They divide the entire space in two parts. The boundary of a half-space is a **hyperplane**,  $H = \{x : a^\top x = b\}$ , where  $a \in \mathbb{R}^n, a \neq 0, b \in \mathbb{R}$ .
- **hyperslabs**,  $S = \{x : |a^\top x - b| \leq \epsilon\}$ , for a given tolerance  $\epsilon \geq 0$  and  $a \in \mathbb{R}^n, a \neq 0, b \in \mathbb{R}$ .
- **polyhedra**,  $P = \{x : a_i^\top x \leq b_i, i = 1, \dots, m\}$ , where  $a_i \in \mathbb{R}^n, b_i \in \mathbb{R}, i = 1, \dots, m$ . A polyhedron could also be written in terms of intersecting half-spaces:

$$P = \cap_{i=1}^m H_i, \quad H_i = \{x : a_i^\top x \leq b_i, i = 1, \dots, m\}.$$

In this work, we will make use of a special case of a polyhedron, namely affine subspaces

$$x : Ax = b.$$

- **ellipsoids**,  $\|Ax - b\|_2 \leq \varepsilon$ .

**Definition 2** (Convex hull). *Given any subset  $C$  of  $\mathbb{R}^n$ , the intersection of all convex sets containing  $C$ , is called the convex hull of  $C$ .*

### 2.1.1.1 Convex Functions

Let  $\bar{\mathbb{R}} := [-\infty, \infty]$  be the **extended real line** with the arithmetic

$$\begin{aligned} a + \infty &= \infty + a = \infty && \text{for } -\infty < a \leq \infty, \\ a - \infty &= -\infty + a = -\infty && \text{for } -\infty \leq a < \infty, \\ a\infty &= \infty a = \infty, \quad a(-\infty) = (-\infty)a = -\infty, && \text{for } 0 < a \leq \infty, \\ a\infty &= \infty a = -\infty, \quad a(-\infty) = (-\infty)a = \infty && \text{for } -\infty \leq a < a, \\ 0\infty &= \infty 0 = 0 = 0(-\infty) = (-\infty)0, \quad -(-\infty) = \infty, \\ \inf \emptyset &= +\infty, \quad \sup \emptyset = -\infty. \end{aligned}$$

Then, functions  $f : \mathbb{R}^n \rightarrow \bar{\mathbb{R}}$  are called **extended real-valued** functions.

**Definition 3** (Effective domain). *The set*

$$\text{dom } f = \{x \in X : f(x) < \infty\} \tag{2.1}$$

*is the **effective domain** of  $f$ .*

**Definition 4** (Convex function). *A function  $f$  defined on  $X$ , is called convex if for any  $x, y \in X$  and any  $0 \leq \lambda \leq 1$  such that  $\lambda x + (1 - \lambda)y \in X$ , we have*

$$f(\lambda x + (1 - \lambda)y) \leq \lambda f(x) + (1 - \lambda)f(y), \quad \forall x, y \in \text{dom } f.$$

**Definition 5** (Strictly convex functions). *A function  $f$  is called strictly convex if*

$$f(\lambda x + (1 - \lambda)y) < \lambda f(x) + (1 - \lambda)f(y).$$

*whenever  $x \neq y$ .*

The properties of convex sets also apply to convex functions. We further mention:

- Adding a linear function: If  $f_i$  are convex functions, then  $g(x) = \sum_i \alpha_i f_i(x)$  is convex, with  $\alpha_i$  a scalar;
- Pointwise maximum: If  $f_i$  are convex, then  $g(x) = \max_i f_i(x)$  is also convex;

**Definition 6** (Lower-semicontinuous functions). *A function  $f : C \rightarrow \bar{\mathbb{R}}$  is lower-semicontinuous if and only if for every real number  $\lambda$ , the set*

$$\{x \in C : f(x) \leq \lambda\}$$

*is closed.*

**Definition 7** (Proper functions). *A function  $f : C \rightarrow \bar{\mathbb{R}}$  is called proper if it takes nowhere the value  $-\infty$  and is not identical to  $+\infty$ .*

There exist several connections between convex sets and convex functions. The simplest associates with each set  $X \in \mathbb{R}^n$  the *indicator function*  $\delta_X(\cdot)$  of  $X$ , where

$$\delta_X(x) = \begin{cases} 0, & \text{if } x \in X, \\ +\infty, & \text{if } x \notin X. \end{cases}$$

By adding indicator functions to objective functions, we are able to enforce constraints on the analyzed problem,

$$\inf_{x \in X} f(x) = \inf_{x \in \mathbb{R}^n} \{f(x) + \delta_X(x)\}.$$

Throughout this thesis, we will make extensive use of the *support function*  $\sigma_X(\cdot)$  of a set  $X$ , defined by:

$$\sigma_X(y) = \sup_{x \in X} \langle y, x \rangle,$$

where "sup" denotes the *supremum* of the inner product  $\langle y, x \rangle$ , as  $x$  ranges over  $X$ . If the set  $X$  is the probability simplex,  $\Delta_n \subset \mathbb{R}^n$ , then for every  $y \in \mathbb{R}^n$  and  $x \in \Delta_n$

$$\sigma_{\Delta_n}(y) = \sup_{x \in \Delta_n} \langle y, x \rangle = \sup_{x \in \Delta_n} \sum_{i=1}^n \langle y_i, x_i \rangle = \text{vecmax}(y) \sum_{i=1}^n x_i = \text{vecmax}(y). \quad (2.2)$$

**Definition 8** (First order differentiability). *If  $f : X \rightarrow \mathbb{R}$  is differentiable, then  $f$  is convex if and only if*

$$f(y) \geq f(x) + \langle y - x, \nabla f(x) \rangle, \quad \forall x, y \in \text{dom } f.$$

In other words, a lower bound on the convex function is given by the first order Taylor approximation.

**Definition 9** (Second order differentiability). *If  $f$  is twice differentiable, then  $f$  is convex if and only if its Hessian is positive semi-definite. That is:*

$$\nabla^2 f(x) \succeq 0, \quad \forall x \in \text{dom } f.$$

One common way to check if the matrix is *positive semi-definite* is to consider the eigenvalues of the matrix. If *all* are non-negative, the condition is satisfied. Likewise, for twice differentiable *strictly convex functions*, the Hessian matrix is *positive definite*, if  $\nabla^2 f(x) \succ 0$ .

**Definition 10** (Lipschitz gradient function). *We say that a smooth convex function  $f$  is continuously differentiable with Lipschitz continuous gradient  $L$  if the following inequality holds:*

$$\|\nabla f(x) - \nabla f(y)\| \leq L\|x - y\|, \forall x, y \in \mathbb{R}^n,$$

and we denote it by  $f \in \mathcal{F}_L^{1,1}(\mathbb{R}^n)$ .

### 2.1.1.2 Subgradients and Conjugates

For a function  $f : \mathbb{R}^n \rightarrow \overline{\mathbb{R}}$ , in order to establish if a point  $x \in \text{dom } f$  is a local minimum or maximum, the first derivative test is performed, i.e.  $\nabla f(x) = 0$ . This is possible if and only if the function is smooth (continuously differentiable). But what happens if the function is non-smooth? In this case, the generalization of the gradient comes into place, namely the subgradient.

**Definition 11** (Subgradient). *A vector  $g \in \mathbb{R}^n$  is a subgradient of  $f : \mathbb{R}^n \rightarrow \overline{\mathbb{R}}$  at  $x \in \text{dom } f$  if*

$$f(y) \geq f(x) + \langle g, y - x \rangle, \forall y \in \text{dom } f.$$

The collection of all subgradients defines the *subdifferential* and is denoted by

$$\partial f(x) = \{g \in \mathbb{R}^n \mid f(y) \geq f(x) + \langle g, y - x \rangle\}. \quad (2.3)$$

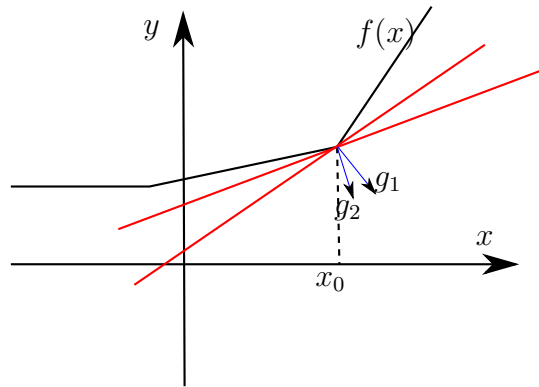


Figure 2.3: Different subgradients  $g_1, g_2$  of the function  $f$ .

#### Properties of subgradients:

1. The subdifferential set  $\partial f(x)$  is closed and convex.
2.  $\partial f(x)$  can be empty, a singleton or a set with infinitely many elements.
3. If  $f$  is convex and differentiable, then  $\{\nabla f(x)\} = \partial f(x)$ .

Next, we introduce the notion of conjugate functions, as it is closely related to the notion of subgradients and to the concept of duality, that will be presented in the following lines.

**Definition 12** (Conjugate function). *The conjugate of a function  $f : \mathbb{R}^n \rightarrow [-\infty, +\infty]$  is defined as:*

$$f^*(p) := \sup_{x \in \mathbb{R}^n} \{\langle p, x \rangle - f(x)\}. \quad (2.4)$$

Note that  $f^*$  is convex and lower-semicontinuous (lsc), because it is the supremum of the family of affine continuous functions  $(\langle \cdot, x \rangle - f(x))_{x \in X}$ . If  $f$  is a lsc, proper convex function, then  $f^*$  is also lsc, proper convex and the following holds:

$$(f^*)^* = f.$$

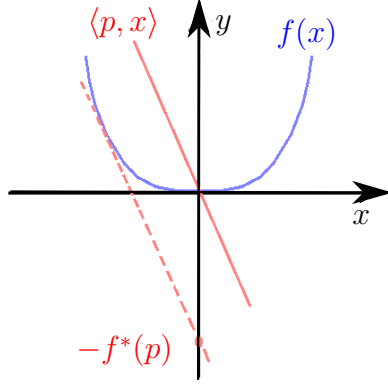


Figure 2.4: Graphical illustration of the conjugate function.

**Definition 13** (Preimage). Let  $f : A \rightarrow B$  be a map between sets  $A$  and  $B$  with  $Y \subseteq B$ . We call the preimage of  $Y$  under  $f$  to be the set of all elements of  $A$  that map to elements in  $Y$  under  $f$ . Thus

$$f^{-1}(Y) = \{a \in A \mid f(a) \in Y\}.$$

**Proposition 1** (Inversion rule of subgradients [99]). For any proper, lower-semicontinuous, convex function  $f$ , one has  $\partial f^* = (\partial f)^{-1}$  and  $\partial f = (\partial f^*)^{-1}$ .

**Note:**  $f^{-1}$  in Prop. (1) denotes the preimage of a function, in the sense that

$$y \in \partial f(x) \quad \Leftrightarrow \quad x \in \partial f^*(y),$$

and not the inverse of a function.

For indicator functions, the conjugate is nothing else than the support function:

$$\delta_C^*(p) = \sup_{x \in \mathbb{R}^n} \{\langle p, x \rangle - \delta_C(x)\} = \sup_{x \in C} \langle p, x \rangle = \sigma_C(p). \quad (2.5)$$

### 2.1.1.3 Fenchel Duality

The subject of duality is frequently used in the context of convex minimization. Being able to express a problem in its dual form, offers the user several benefits:

- the dual program is always convex, even if the primal is not;
- the number of constraints in the primal problem equals the number of variables in the dual problem. Consequently, the dual problem may have less number of variables than the primal problem.
- the primal-dual formulation often results in efficient splitting optimization schemes, whose solutions can be reached by solving a series of smaller and easier subproblems. Such formulations are known to lead to methods that are highly parallelizable, thus increasing efficiency when problem sizes are very large.

### Fenchel Duality of Convex Problems

We give the definition of duality in terms of Legendre-Fenchel conjugates.

**Theorem 2.1.1** ([99]). *Let  $f : \mathbb{R}^n \rightarrow \bar{\mathbb{R}}$ ,  $g : \mathbb{R}^m \rightarrow \bar{\mathbb{R}}$  and  $A \in \mathbb{R}^{m \times n}$ . Consider the two problems*

$$\inf_{x \in \mathbb{R}^n} \varphi(x), \quad \varphi(x) = \langle c, x \rangle + f(x) + g(b - Ax), \quad (2.6a)$$

$$\sup_{y \in \mathbb{R}^m} \psi(y), \quad \psi(y) = \langle b, y \rangle - g^*(y) - f^*(A^\top y - c) . \quad (2.6b)$$

where the functions  $f$  and  $g$  are proper, lower-semicontinuous (lsc) and convex. Suppose that

$$b \in \text{int}(A \text{ dom } f + \text{ dom } g), \quad (2.7a)$$

$$c \in \text{int}(A^\top \text{ dom } g^* - \text{ dom } f^*) . \quad (2.7b)$$

Then the optimal solutions  $\bar{x}, \bar{y}$  are determined by

$$0 \in c + \partial f(\bar{x}) - A^\top \partial g(b - A\bar{x}), \quad 0 \in b - \partial g^*(\bar{y}) - A \partial f^*(A^\top \bar{y} - c) \quad (2.8a)$$

and connected through

$$\bar{y} \in \partial g(b - A\bar{x}), \quad \bar{x} \in \partial f^*(A^\top \bar{y} - c), \quad (2.9a)$$

$$A^\top \bar{y} - c \in \partial f(\bar{x}), \quad b - A\bar{x} \in \partial g^*(\bar{y}) . \quad (2.9b)$$

In optimization, the primal objective is always lower bounded by the dual objective. If  $\varphi(\bar{x})$ ,  $\psi(\bar{y})$  would be the optimal value of the primal, respectively

the dual problem, then the following inequality holds  $\psi(\bar{y}) \leq \varphi(\bar{x})$ ; also called *weak duality*. The difference  $\varphi(\bar{x}) - \psi(\bar{y})$  is referred to as the *duality gap*. The notion of *strong duality* occurs when  $\varphi(\bar{x}) = \psi(\bar{y})$  and the conditions (2.7) hold. It is desirable that all primal-dual problems have the strong duality property, because in such cases one can often solve the dual problem in a simpler way and recover the primal solution from (2.9).

For a more detailed reference of duality notions, we point the reader to the well known book of [99].

#### 2.1.1.4 Convex Programs with Linear Constraints

We consider the following special case of convex optimization:

$$\min_x f(x) \quad \text{s.t.} \quad Ax = b, \quad x \geq 0, \quad (2.10)$$

where the function  $f(x) : \mathbb{R}^n \rightarrow \mathbb{R}$  is convex, proper and lsc.

In order to take cases of noisy data into account, the following relaxed formulation of constraints is appropriate:

$$\min_x f(x) \quad \text{s.t.} \quad \|Ax - b\|_2 \leq \varepsilon, \quad x \geq 0. \quad (2.11)$$

Likewise, an alternative form can be analysed, by introducing a regularization parameter  $\lambda$

$$\min_x f(x) + \lambda \|Ax - b\|_2^2 \quad \text{s.t.} \quad x \geq 0. \quad (2.12)$$

In theory, there will always exist a pair  $(\varepsilon, \lambda)$  such that (2.11)  $\Leftrightarrow$  (2.12).

By using regularizers, one replaces the initial ill-posed problem with a "better" conditioned problem, that is able to return an approximate solution which in addition of being continuously, it depends on the given data, and in this sense, is robust.

We describe next few algorithms that can be applied to the problems (2.10), (2.11), or (2.12).

#### Fast Iterative Soft-Thresholding Algorithm (FISTA)

Introduced by Beck and Teboulle [7], FISTA is an extension of Iterative Soft-Thresholding Algorithm (ISTA) [28, 33, 52, 59], that belongs to the class of first order methods, i.e. it relies only on function and gradient evaluations. The algorithm considers the minimization problem of a sum of two convex functions

$$\min_x f(x) + g(x), \quad g \in \mathcal{F}_L^{1,1}(\mathbb{R}^n), \quad f \in \mathcal{F}_0(\mathbb{R}^n) \quad (2.13)$$

with  $f$  a possibly nonsmooth, but "simple" function, in the sense that one can compute its proximal mapping in closed form, which is defined as

$$\text{Prox}_{\lambda f}(x) = \operatorname{argmin}_{y \in \mathbb{R}^n} \frac{1}{2} \|x - y\|^2 + \lambda f(y),$$

for any  $\lambda > 0$ . In this work, we consider  $f$  to be the anisotropic total-variation, i.e.  $f(x) = \|\nabla x\|_1$ , with  $\nabla$  the gradient operator:

$$\nabla = \begin{pmatrix} \partial_1 \otimes I_2 \\ I_1 \otimes \partial_2 \end{pmatrix} \in \mathbb{R}^{p \times n}.$$

$\otimes$  denotes the Kronecker product,  $I_i$ ,  $i = 1, 2$ , are identity matrices with appropriate dimensions and  $\partial_i$  denotes the one-dimensional discrete derivative operator

$$\partial: \mathbb{R}^m \rightarrow \mathbb{R}^{m-1}, \quad \partial_{i,j} = \begin{cases} -1, & i = j, \\ +1, & j = i + 1, \\ 0, & \text{otherwise.} \end{cases}$$

For solving (2.13), one can apply the Forward-Backward splitting algorithm [81], whose procedure is to update the iterates by computing

$$x_k = \text{Prox}_{\lambda f}(x_k - \frac{1}{L} \nabla g(x_k)), \quad \text{with } \lambda \in \left(0, \frac{2}{L}\right), \quad k = 0, 1, 2, \dots; \quad x_0 \in \mathbb{R}^n,$$

or the Over-relaxed Forward-Backward splitting, that introduces an additional relaxation parameter  $-1 < \mu < 1$  to average the current iterate

$$\begin{aligned} x_k &= \text{Prox}_{\lambda f}(z_k - \frac{1}{L} \nabla g(z_k)) \\ z_{k+1} &= x_k + \mu(x_k - x_{k-1}). \end{aligned}$$

A specific feature of FISTA is the possibility to adaptively update the relaxation parameters  $\mu_k$ , which tend to the limit  $\mu_k \rightarrow 1$ , as  $k \rightarrow \infty$  and the introduction of an extrapolation point  $z_k$ . The entire procedure is given in Alg. 1.

---

**Algorithm 1** FISTA algorithm

---

- 1:  $z_1 = x_0 \in \mathbb{R}^n, t_1 = 1, L$  – Lipschitz constant.
  - 2: **for**  $k \geq 1$  **do**
  - 3:    $x_k = \text{Prox}_{\lambda f}(z_k - \frac{1}{L} \nabla g(z_k))$
  - 4:    $t_{k+1} = \frac{1 + \sqrt{1 + 4t_k^2}}{2}$    and    $\mu_{k+1} = \frac{t_k - 1}{t_{k+1}}$
  - 5:    $z_{k+1} = x_k + \mu_{k+1}(x_k - x_{k-1})$
  - 6: **end for**
- 

For this scheme, one cannot prove convergence of the iterates, but one can prove that it reaches an optimal convergence rate of the iterates, namely

$$f(x_k) + g(x_k) - f(x^*) - g(x^*) = O(1/k^2),$$

while the convergence rate for the usual Forward-Backward splitting is only  $O(1/k)$ , with  $k$  representing the number of iterations in the algorithm. This routine can be applied to problems of type (2.12).

### Douglas - Rachford (DR)

The foundations of the Douglas-Rachford method lay in the field of differential equations [43]. Brought into attention a few years later by the work of Lions and Mercier [81], the algorithm proved to be suitable for a broader spectra of applications, different from the initial ones. Since then, numerous variations of the DR approach have been developed, among which we sketch below the most known, ADMM (alternating direction method of multipliers) [13].

---

#### Algorithm 2 Douglas-Rachford algorithm

---

- 1:  $z_0 \in \mathbb{R}^n, \lambda > 0$
  - 2: **for**  $k \geq 1$  **do**
  - 3:    $x_k = \text{Prox}_{\lambda g}(z_k) = \arg\min_{x \in \mathbb{R}^n} \frac{1}{2\lambda} \|x - z_k\|^2 + g(x),$
  - 4:    $v_k = \text{Prox}_{\lambda f}(2x_k - z_k) = \arg\min_{v \in \mathbb{R}^n} \frac{1}{2\lambda} \|v - (2x_k - z_k)\|^2 + f(v),$
  - 5:    $z_{k+1} = z_k + v_k - x_k$
  - 6: **end for**
- 

The approach given in Alg. 2, considers the problem of minimizing the sum of two functions

$$\min_{x \in \mathbb{R}^n} f(x) + g(x), \quad f, g \in \mathcal{F}_0(\mathbb{R}^n). \quad (2.14)$$

The convergence rate of this algorithm is known to be  $O(1/k)$ , as proved in the work of He and Yuan [61], with  $k$  being the iteration counter.

### Alternating Direction Method of Multipliers (ADMM)

Closely related to the Douglas - Rachford algorithm, ADMM solves problems of the type

$$\min f(x) + g(z) \quad \text{s.t. } Ax + Bz = c, \quad \text{with } f, g \in \mathcal{F}_0(\mathbb{R}^n). \quad (2.15)$$

Compared to what has been presented up to now, the variable over which optimization is being performed is split in two parts  $x$  and  $z$ , with the objective function separable across the splitting. In addition, conditions on the functions  $f, g$  are not very restrictive, e.g. are allowed to be non-differentiable, thus covering a large number of optimization problems. ADMM iteratively solves (2.15), via the following procedure:

---

#### Algorithm 3 ADMM [13] algorithm

---

- $x_0 \in \mathbb{R}^n, z_0 \in \mathbb{R}^m, u \in \mathbb{R}^n, \rho > 0$
  - for**  $k \geq 1$  **do**
  - $x_{k+1} = \arg \min_x \left( f(x) + \frac{\rho}{2} \|Ax + Bz_k - c + u_k\|_2^2 \right)$
  - $z_{k+1} = \arg \min_z \left( g(z) + \frac{\rho}{2} \|Ax_{k+1} + Bz - c + u_k\|_2^2 \right)$
  - $u_{k+1} = u_k + Ax_{k+1} + Bz_{k+1} - c,$
  - end for**
-

with  $u$  the scaled dual variable of the *augmented Lagrangian* of problem (2.15). Although it has been reported that ADMM converges slowly to a solution with high accuracy, often it is the case that modest accuracy suffices and this has been empirically proven to happen in a few tens of iterations. Moreover, the algorithm is bound to converge even though inexact minimizations are performed in the  $x, z$  updates. All these characteristics make ADMM very appealing to large-scale applications where a balance between accuracy and computational load is desired. For a more detailed description of this approach, we refer the reader to the tutorial of Boyd and Vandenberghe [13].

### Primal-Dual Algorithm [29]

This algorithm is a slight (but clever) modification of the method of Polyak developed in the 60s. It tackles the problem of minimizing the sum of two convex, possibly non-smooth functions, from a primal-dual perspective. The general form of the primal minimization reads

$$\min_x f(Kx) + g(x),$$

and its corresponding dual maximization

$$\max_y -(f^*(y) + g^*(-K^\top y)),$$

where the operator  $K$  may not be a square matrix. Moreover, the two functions  $f, g$  need to be chosen such that their proximal operators can easily be computed.

One advantage of this approach, given in Alg. 4, over the ones presented earlier, lies in the robust convergence guarantees.

---

**Algorithm 4** Chambolle-Pock primal-dual algorithm

---

- 1:  $L = \|K\|_2, \tau = \sigma = \frac{1}{L}, \theta = 1, k = 0, x_0 = \bar{x}_0 = 0$ ;
  - 2:  $y_{k+1} = \text{Prox}_\sigma(f^*)(y_k + \sigma K \bar{x}_k)$ ,
  - 3:  $x_{k+1} = \text{Prox}_\tau(g)(x_k - \tau K^\top y_{k+1})$ ,
  - 4:  $\bar{x}_{k+1} = x_{k+1} + \theta(x_{k+1} - x_k)$ ,
  - 5:  $k = k + 1$ ,
- 

Later, in Sect. 4.3 we will give a comparison between these methods and our approaches.

## 2.1.2 Compressed Sensing

Reconstruction routines of current sensing devices rely on the well-known Shannon-Nyquist sampling theorem. The assertion of this theorem has been the prevailing

principle in electrical and optical engineering. It states that a signal can be perfectly reconstructed if the sampling rate is higher than twice the highest frequency content of the signal in its Fourier transform.

In the last decade, however, a new sensing approach has been advocated to give remarkable results, being able to accurately reconstruct a signal from a highly incomplete number of *linear* and *non-adaptive* measurements. It is known as *Compressive Sampling* or *Compressed Sensing* (CS).

### 2.1.2.1 Compressed Sensing

The general assumption behind Compressed Sensing (CS) is that a signal can be **sparse** represented (i.e. having a small number of non-zero coefficients) in a general basis (e.g. wavelets) or that it belongs to a distinct class of functions (e.g. piecewise constant functions). A similar relation underlies lossy compression techniques used in JPEG, JPEG2000. Compression routines require beforehand a lengthy and costly procedure to acquire full information of a signal, which in the end, is almost entirely discarded in the compression stage, thus resulting in a **sparse** measured signal.

In a nutshell, what CS wants to achieve is to sample and compress a signal at the same time. Unlike JPEG or JPEG2000, however, in CS information is not lost by "squeezing" the signal, leaving the user the possibility to return to the original sample from its compressed version. The non-trivial part of the problem is how to know beforehand the signal locations where to sample.

What is beneficial in CS is its practicality, in the sense that efficient algorithms can be employed to perform reconstruction, using convex optimization routines and even greedy algorithms. In order to recover a signal  $x \in \mathbb{R}^m$ , one of the basic optimization problems that CS applies is

$$\bar{x} = \underset{x}{\operatorname{argmin}} \|x\|_0 \quad s.t. \quad Ax = b, \quad (2.16)$$

where the linear system of equations is *underdetermined*, with the compressive sampled signal given by the vector  $b$ . However, due to its combinatorial nature, solving (2.16) is in general NP-hard. Therefore, a common approach is to relax the objective function to the  $\ell_1$  norm, that is known to promote sparsity and to be convex:

$$\bar{x} = \underset{x}{\operatorname{argmin}} \|x\|_1 \quad s.t. \quad Ax = b. \quad (2.17)$$

Perfect reconstructions as minimizers have been shown to exist only for suitable matrices  $A$ , that fit into the theoretical optimal bounds. Such matrices should have high spark, also known as complete rank, high nullspace property order, and a high RIP order with a relatively small RIP constant.

Before we go further and detail these properties, let us formally introduce the notion of *sparsity* in the context of Compressive Sensing.

**Definition 2.1.1** (Sparsity). A signal  $x \in \mathbb{R}^n$  is said to be  $k$ -sparse if it has  $k$  non-zero entries:

$$k = \|x\|_0 := \|\{i : x_i \neq 0\}\|. \quad (2.18)$$

**Definition 2.1.2** (Spark, [44]). Let  $A \in \mathbb{R}^{m \times n}$  be an arbitrary matrix. Then the *spark* of  $A$  denoted by  $\text{spark}(A)$  is the minimal number of linearly dependent columns of  $A$ .

**Proposition 2.1.2** ([38]). *Any  $k$ -sparse solution  $\bar{x}$  of a linear system  $Ax = b$  is unique if  $\|\bar{x}\|_0 = k < \text{spark}(A)/2$ .*

With  $A$  being underdetermined in tomography applications, the nullspace of  $A$  also plays a particular role in the analysis of uniqueness of the minimization problem (2.17). The related so-called *nullspace property (NSP)* is defined as follows.

**Definition 2.1.3** (Nullspace property). Let  $A \in \mathbb{R}^{m \times n}$  be an arbitrary matrix. Then  $A$  has the *nullspace property (NSP) of order  $k$*  if, for all  $v \in \mathcal{N}(A) \setminus \{0\}$  and for all index sets  $|S| \leq k$ ,  $\|v_S\|_1 < \frac{1}{2}\|v\|_1$ .

**Proposition 2.1.3** ([54]). *Any  $k$ -sparse solution  $\bar{x}$  of a linear system  $Ax = b$  is the unique solution of (2.17), if  $A$  satisfies the nullspace property of order  $k$ .*

**Proposition 2.1.4** ([95, 115, 75]). *Every  $k$ -sparse nonnegative vector  $\bar{x}$  is the unique positive solution of  $Ax = A\bar{x}$  if and only if every nonzero nullspace vector has at least  $k + 1$  negative (and positive) entries.*

The *Restricted Isometry Property (RIP)* defined next, characterizes matrices which are well conditioned when operating on sparse vectors. This is probably the most popular CS condition since it also enables *stable* recovery.

**Definition 2.1.4.** A matrix  $A$  is said to have the *Restricted Isometry Property  $RIP_{\delta,k}$*  if, for any  $k$ -sparse vector  $x$ , the relation

$$(1 - \delta)\|x\|^2 \leq \|Ax\|^2 \leq (1 + \delta)\|x\|^2, \quad \delta \in (0, 1) \quad (2.19)$$

holds.

This property implies that every submatrix  $(A^{i_1}, \dots, A^{i_k})$  formed by keeping at most  $k$ -columns of  $A$  has nonzero singular values bounded from above by  $1 + \delta$  and from below by  $1 - \delta$ . In particular, (2.19) implies that a matrix  $A$  cannot satisfy  $RIP_{\delta,k}$ , if  $k \geq \text{spark}(A)$ .

**Proposition 2.1.5** ([17], Thm. 1.1). *Candès has shown that if  $A \in RIP_{\delta,2k}$  with  $\delta < \sqrt{2} - 1$ , then all  $k$ -sparse solutions  $\bar{x}$  of (2.17) are unique.*

In [17, Thm. 1.2], the RIP condition also implies *stable* recovery even in case of observation errors.

**Proposition 2.1.6** ([17], Thm. 1.2). *When measurements are corrupted with noise*

$$b = A\bar{x} + \nu,$$

where  $\nu$  is an unknown noise term, recovery of  $\bar{x}$  is usually performed by

$$\min \|x\|_1 \quad \text{s.t.} \quad \|Ax - b\|_2 \leq \varepsilon, \quad (2.20)$$

with  $\varepsilon$  an upper bound on the size of  $\nu$ . Provided that the observation error is small enough,  $\|\nu\|_2 \leq \varepsilon$ , and  $A \in \text{RIP}_{\delta, 2k}$  with  $\delta < \sqrt{2} - 1$ , then the solution  $x$  of (2.20) obeys

$$\|x - \bar{x}\|_2 \leq C_0 k^{-\frac{1}{2}} \|\bar{x} - (\bar{x})_k\|_2 + C_1 \varepsilon,$$

where  $C_0$  and  $C_1$  are explicit constants depending on  $\delta$ , and  $(\bar{x})_k$  is the vector  $\bar{x}$  with all but the  $k$ -largest entries set to zero.

Moreover, it has been known since from the beginning in the field of compressed sensing that *random matrices*, like Gaussian and Bernoulli matrices with i.i.d. sampled entries, satisfy well the theoretical requirements for perfect recovery. Specifically, given a random entry type matrix  $A \in \mathbb{R}^{m \times n}$ , there is a high-probability to reconstruct all  $k$ -sparse vectors  $x$ , from  $b = Ax$ , provided that

$$m \geq Ck \ln(n/k), \quad (2.21)$$

where  $C > 0$  is a constant. This condition on the number  $m$  of measurements required for perfect recovery, reveals a lower bound that essentially depends on the sparsity  $k$  of the analysed signal  $x$ , while the size of the signal  $n$  has only a mild logarithmic influence.

We have given a brief review of Compressed Sensing along with its properties and recovery conditions. What is to be retained from these lines, is that *sparsity* of the problem plays an important role in the reconstruction process and convex optimization routines can be efficiently employed to model the problem at hand.

### 2.1.2.2 Sparsity versus Cosparsity

The content of this section relies on the papers of [87] and [71].

The problem of signal recovery from an incomplete set of measurements has been long researched in the image and signal processing communities, with the help of the compressed sensing theory. The assumption lying at the base of this theory is that the signal is sparse, i.e. it has very few non-zero coefficients. The set of indices  $i$ , form the *support* of the signal  $x$ . One example of such a signal

would be  $x = [1, 0, 0, 2, 0, 3, 0, 0, 9, 0, 0]$ . This is a 4-sparse vector. Many signals that arise in practice are sparse with respect to a basis or dictionary. That is

$$x = Dz, \quad z \in \mathbb{R}^d, \quad (2.22)$$

where  $z$  is  $k$ -sparse and  $D \in \mathbb{R}^{q \times d}$ ,  $d \geq q$  is an overcomplete matrix whose columns form the dictionary. In this case, one solves the following optimization problem

$$\tilde{z} = \underset{z}{\operatorname{argmin}} \|z\|_1 \quad \text{s.t.} \quad ADz = b. \quad (2.23)$$

This approach is referred to as the *synthesis model*. Commonly, the dictionary is chosen to be an orthogonal matrix  $D \in \mathbb{R}^{n \times n}$ , so as to obtain sparsity with respect to an orthonormal basis. Other choices are also possible, such as wavelets (see Fig. 2.5), etc.

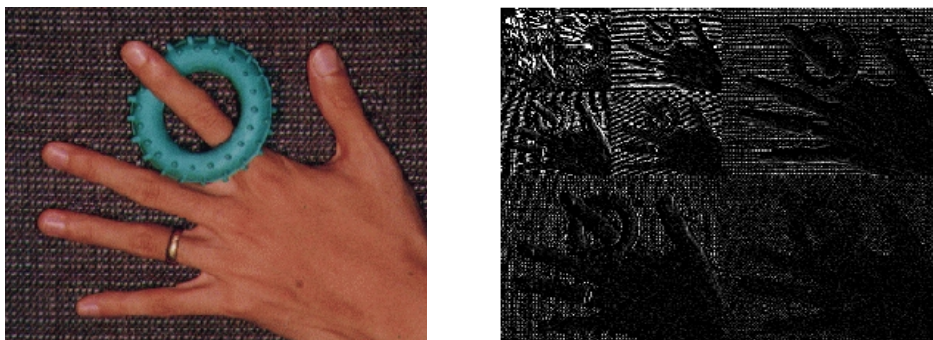


Figure 2.5: Synthesis model. Two-dimensional Haar wavelet of "Hand" with horizontal, vertical and diagonal (detail) coefficients. Notice the higher sparsity level in the detail coefficients (the images on the lower right corner of each scale). Black represents 0 and white represents a value different than 0. The darker the image is (more black), the more sparse it is.

An alternative viewpoint to this model is to consider *cosparse* signals. That is, for a possibly overcomplete analysis operator  $\Omega \in \mathbb{R}^{p \times n}$ , with  $p \geq n$ , the quantity  $\|\Omega x\|_0$  is small. This is referred to as the *analysis model* [45]. Instead of (2.23), the optimization problem reads

$$\underset{x}{\operatorname{argmin}} \|\Omega x\|_1 \quad \text{s.t.} \quad Ax = b, \quad \text{with } \Omega \in \mathbb{R}^{p \times n}, \quad A \in \mathbb{R}^{m \times n}, \quad b \in \mathbb{R}^m, \quad (2.24)$$

which is able to return a good estimate depending on how "cosparse"  $x$  is. Cosparcity of a signal is defined as

$$\ell = p - \|\Omega x\|_0, \quad (2.25)$$

i.e. the interest lies in the number of zeros the analysed vector  $\|\Omega x\|_0$  contains. Typical examples of analysis operators are the finite difference operators, shift invariant wavelet transform, etc.

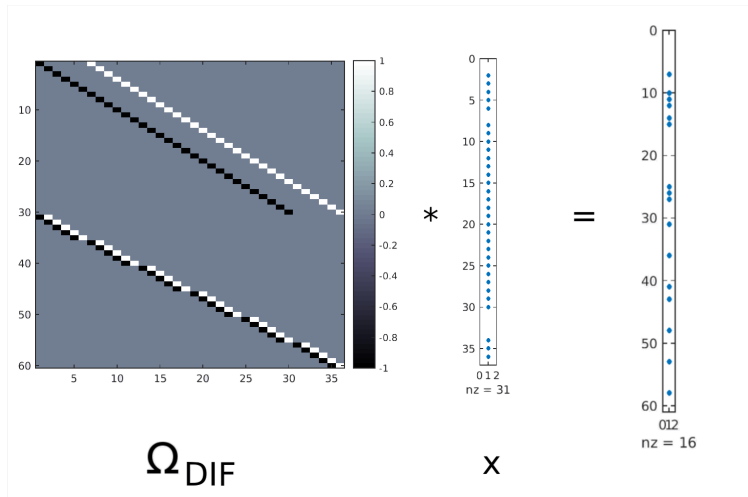


Figure 2.6: Visualization of the analysis model. The analysis operator is taken to be the forward difference operator in the X and Y direction, stacked together, named  $\Omega_{DIF}$ . Applied to a signal of interest, which is dense, i.e. # of nonzeros is 31 in this example, it returns a *cosparse signal*, having an increased # of zeros, see right side of the illustration.

**Definition 2.1.5** (Cosupport). Similarly to sparse signals, we introduce the notion of *cosupport* of  $x$  with respect to  $\Omega \in \mathbb{R}^{p \times n}$

$$\Lambda := \{r \in [p] : (\Omega x)_r = 0\}, \quad |\Lambda| = \ell. \quad (2.26)$$

With the cosupport, i.e. the index set of the zero entries in  $\Omega x$ , one is able to define a corresponding subspace of  $\ell$ -cosparse signals:

$$\bigcup_{\Lambda \subset [p]: |\Lambda|=\ell} W_\Lambda,$$

where  $W_\Lambda = \text{span}(\omega_j, j \in \Lambda)^\perp$ , with  $\omega_j$  being the rows of the matrix  $\Omega$ . For the specific case of square and invertible dictionaries, it has been shown that the two models, synthesis and analysis, are equivalent, i.e.  $D = \Omega^{-1}$ , [87].

### 2.1.2.3 Theoretical Recovery Guarantees

In most applications, properties such as RIP, see Def. 2.1.4, do not hold. We introduce the notion of **bipartite graphs** and **lossless expanders** in the following. Looking at the problem from this perspective, offers the user alternative criteria for reconstructing sparse vectors from a small number of measurements.

### Expander Graphs

Expander graphs are a certain family of graphs that are at the same time sparse (looking at the ratio between the number of edges and the number of vertices) and highly connected. In this work, expander graphs will be used in connection with bipartite graphs, that represent the incidence geometry of tomographic imaging later on.

**Definition 14** (Bipartite graph). *A bipartite graph  $G = (L \cup R, E)$  is a graph comprised of two disjoint sets of vertices  $L$  and  $R$ , where edges  $E \subseteq L \times R$  only correspond to pairs  $(l, r)$  of left nodes  $l \in L$  and right nodes  $r \in R$ .*

**Definition 15** (Degree of a vertex). *Given a graph,  $G = (L \cup R, E)$ , the degree of a vertex  $v \in L \cup R$  is the number of incident edges, i.e.*

$$\text{deg}(v) = |\{u \in L \cup R : (v, u) \in E\}|$$

**Definition 16** ( $d$ -regular graph). *We call a graph to be  $d$ -left regular if and only if all vertices in  $L$  have the same degree  $d$ . A right-regular graph is defined analogously.*

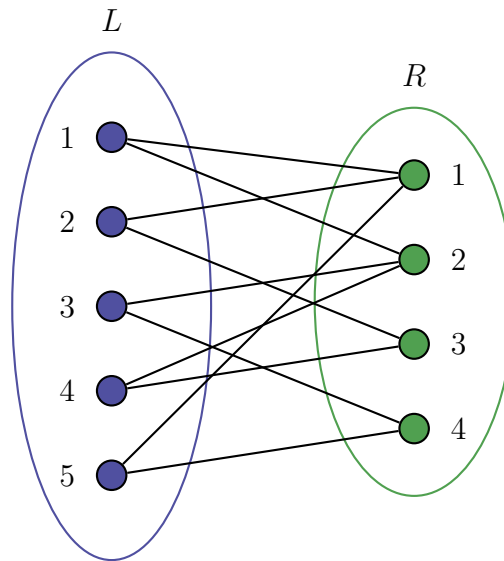


Figure 2.7: Example of a left regular bipartite graph with left degree 2.

Let us define the set of right vertices connected to the set  $J$ , i.e. the neighbourhood of the set  $J$ , to be

$$\eta(J) = \{i \in R : \text{there is a } j \in J \subseteq L \text{ with } (j, i) \in E\}.$$

We are now ready to introduce the notion of *lossless expanders*.

**Definition 17** (Lossless expanders [54], Def. 13.1). *Given a set  $J \subset L$  of left vertices, a left regular bipartite graph with left degree  $d$  is called  $(s, d, \theta)$ -lossless expander, if it satisfies the expansion property*

$$|\eta(J)| \geq (1 - \theta)d|J|, \quad (2.27)$$

for all sets  $J$  of left vertices such that  $|J| \leq s$ . The smallest  $\theta \geq 0$  for which the expansion property holds is called the  $s$ -th restricted expansion constant and is denoted by  $\theta_s$ .

**Definition 18** (Existence of Lossless Expanders, [54], Th.13.6). *For  $0 < \varepsilon < 1/2$ , the proportion of  $(s, d, \theta)$ -lossless expanders among all left  $d$ -regular bipartite graphs with  $|L| = N$  left vertices and  $|R| = m$  right vertices exceeds  $1 - \varepsilon$  provided that*

$$d = \left\lceil \frac{1}{\theta} \ln \left( \frac{eN}{\varepsilon s} \right) \right\rceil \quad \text{and} \quad m \geq c_\theta s \ln \left( \frac{eN}{\varepsilon s} \right), \quad (2.28)$$

where  $c_\theta$  is a constant depending only on  $\theta$ .

Moreover, the adjacency matrix of such bipartite graphs offers robust results when applied to sparse recovery  $\ell_1$ -minimization problems, such as basis pursuit. The following theorem backs up the ones just stated.

**Theorem 2.1.7** ([54], Th 13.10). *Suppose that  $A \in \{0, 1\}^{m \times N}$  is the adjacency matrix of a left  $d$ -regular bipartite graph satisfying*

$$\theta_{2s} < \frac{1}{6}.$$

For  $x \in \mathbb{C}^N$  and  $e \in \mathbb{C}^m$  with  $\|e\|_1 \leq \eta$ , if  $y = Ax + e$ , then a solution  $\tilde{x}$  of

$$\min_{z \in \mathbb{C}^N} \|z\|_1 \quad \text{s.t.} \quad \|Az - y\|_1 \leq \eta$$

approximates the vector  $x$  with  $\ell_1$ -error

$$\|x - \tilde{x}\|_1 \leq \frac{2(1 - 2\theta)}{(1 - 6\theta)} \sigma_s(x)_1 + \frac{4}{(1 - 6\theta)d} \eta.$$

**Definition 19** (Adjacency matrix, [54], Def. 13.9). *The adjacency matrix of a bipartite graph  $G = (L \cup R, E)$  is the  $m \times N$  matrix  $A$  with entries*

$$A_{(i,j)} = \begin{cases} 1, & \text{if } (i, j) \in E \\ 0, & \text{otherwise.} \end{cases}$$

The corresponding adjacency matrix for the bipartite graph in Fig. 2.7 is

$$A = \begin{bmatrix} 1 & 1 & 0 & 0 & 1 \\ 1 & 0 & 1 & 1 & 0 \\ 0 & 1 & 0 & 1 & 0 \\ 0 & 0 & 1 & 0 & 1 \end{bmatrix}.$$

The connection between tomography and the adjacency matrix of expander graphs is attributed to the incidence relation of the image pixels with incoming rays. If the  $i$ -th ray intersects the  $j$ -th pixel, then the  $A_{ij}$  entry will be valued 1, 0 otherwise. In correspondence, the number of rows and columns in matrix  $A$  stand for the number of rays and pixels used in modelling the acquisition process. Letting the measurement matrix  $A$  have such a sparse structure, makes it easy for storage purposes and allows more accurate computations, having less drawbacks when it comes to precision in calculations. More on tomography and the acquisition process, can be read in Sect. 2.2.3.

An in-depth analysis on uniqueness of recovery of non-negative signals using expander graphs related to the context of compressive sensing have been reported by Petra et. al. [95], Xu and Hassibi [117] and Wang et. al. [115]. Interpreting the problem from the viewpoint of bipartite expander graphs, one is able to determine relations bounding the required number of measurements  $m$  with respect to the size  $n$  of the signal, necessary to obtain a unique non-negative solution to the analysed system of equations.

The work in [95] inspects appropriate bounds for *exact* reconstruction of sparse signals, with application in tomography, where the measurement matrix is known to be badly scaled and does not fulfil the assumptions needed to apply compressed sensing theory.

The paper of Wang [115], focused on general expander matrices, i.e. whose entries are not restricted to binary values, and looked into the matter of finding a unique non-negative solution to underdetermined linear systems, by relating the support of the sparse signal to its dimension, through a constant ratio. We report next the corresponding result of Wang et. al.

**Theorem 2.1.8** (Th.4, [115]). *For an adjacency matrix  $A$  of an  $(s, \theta)$  expander with left degrees in the range  $[d_l, d_u]$ , if  $s\theta > (\sqrt{5}-1)/2 \approx 0.618$ , then for any non-negative  $k$ -sparse vector  $x_0$  with  $k \leq s/(1 + \theta\rho)N$ , the set  $\{x | Ax = Ax_0, x \geq 0\}$  is a singleton.*

The quantities  $d_l, d_u$  represent the minimum, respectively the maximum of the left degrees, with  $\rho$  defined as  $\rho = d_l/d_u$ ,  $0 < \rho \leq 1$ .

Continuing on the idea of structured representations, we turn our attention to a widely known field in machine learning, called graphical models.

### 2.1.3 Graphical Models and Segmentation

The task of segmenting an image into meaningful parts has been long researched and yet, no unified approach has shown to give satisfactory results for a wide range of images. Graphical models, through their ability to handle uncertainty by use of probability theory and to handle large complex problems with the help of graph theory, have become an important framework in the field of image processing.

They solve energy functions of the type

$$\mathcal{E}(f) = \sum_{v \in V} D_v(f_v) + \sum_{p, q \in E} V_{p, q}(f_p, f_q), \quad (2.29)$$

where the first term, called *unary* term can be interpreted as a fidelity or distance measure to the observed data  $f$  and the second term, the *pairwise* term, as a regularization or smoothness term. By representing image pixels as vertices in a graph, it is possible to partition an image into foreground and background by making a "cut" through the graph (binary labelling case).

In the upcoming lines, we give a brief introduction in the terminology used in graph theory in Sect. 2.1.3.1, followed by a concise presentation of how graphical models can be applied to labelling problems, in Sect. 2.1.3.2.

#### 2.1.3.1 Elements of Graph Theory

A graph  $G$  is an ordered pair  $G = (V, E)$  consisting of a nonempty set  $V(G)$  of *vertices* and a set  $E(G) \subset V \times V$  of *edges*, that is disjoint from  $V(G)$ . For  $n = |V|$  vertices, there is a number of  $m = |E| \leq \binom{n}{2}$  edges.

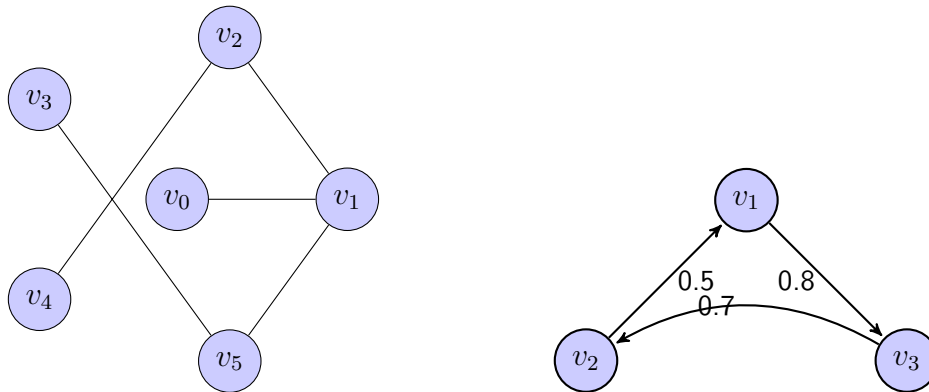


Figure 2.8: **Left:** Undirected graph with 6 vertices and 5 edges. **Right:** Weighted directed graph.

Commonly, two types of graphs are being used in practice: **undirected** and **directed** graphs. In the former type, no distinction is made between edges

$(v_3, v_5)$  and  $(v_5, v_3)$ , for example (see Fig. 2.8 left). Vertices  $v_3, v_5 \in V$  are called **neighbouring** vertices. The set of all neighbouring vertices of a given vertex  $i$ , is denoted by  $\eta(i)$ .

In a **directed** graph, however, each edge from the set  $E(G)$  has an associated direction (see Fig. 2.8 right). It is also possible to distinguish these edges not only by their direction, but also by the weights associated to them, in which case the graph is called a **weighted directed** graph and we denote it as  $G_w = (V, E, w_c)$ .

Let  $V'$  be a nonempty subset of  $V$ . The subgraph of  $G$  whose vertex set is  $V'$  and whose edge set is the set of those edges of  $G$  that have both ends in  $V'$  is called the subgraph of  $G$  *induced* by  $V'$  and is denoted by  $G[V']$ . We say that  $G[V']$  is an *induced subgraph* of  $G$ .

In a simple graph, a *walk*  $\mathcal{W}$  is determined by the sequence of its vertices. If the edges of the walk are distinct, and the same is true for its vertices, then  $\mathcal{W}$  is called a *path*.

**Definition 20** (Connected vertices). *Two vertices  $u$  and  $v$  of  $G$  are said to be connected if there is a  $(u, v)$ - path in  $G$ .*

**Definition 21** (Connected graph). *A graph is connected if there is a path between every pair of its vertices.*

**Definition 22** (Connected component). *A connected subgraph  $G[V']$  is referred to as a connected component .*

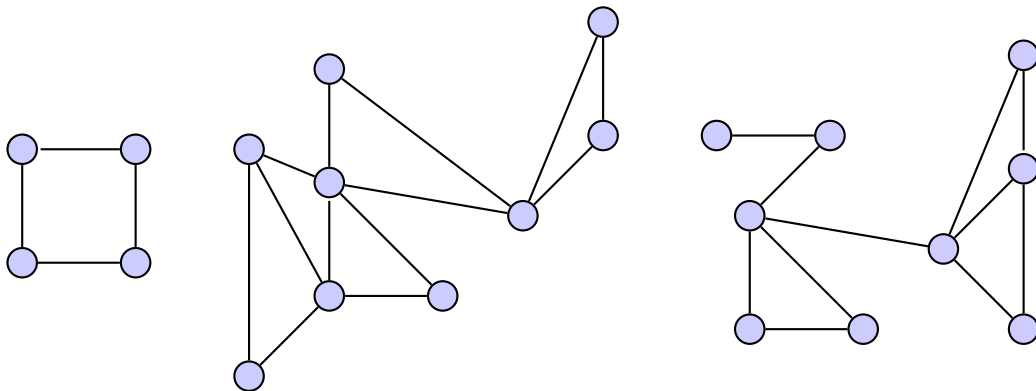


Figure 2.9: Example of graphs with three connected components.

We will make use of the notion of connected components later on, in Sect. 3.3.2, where we derive theoretical bounds for uniqueness of the solution of our reconstruction problem.

### 2.1.3.2 Graph-Cuts

Initially introduced by Kolmogorov and Boykov [14] in the field of computer vision, graph-cuts have proven to be an efficient method to perform image labelling, object detection or tracking. They are approximation algorithms that have shown to find the global optimum of an energy function in polynomial time, for a restricted class of energy functions of binary variables, see Def. 24.

In graph theory, *networks* are *specific* graphs, as detailed below. Considering a directed graph  $G = (\tilde{V}, \tilde{E})$ , the image pixels correspond to the set  $\tilde{V}$  of nodes and the directed edges  $\tilde{E}$  to the neighbourhood used when describing the coherence between neighbouring pixels, either 4 - or 8 - connected neighbourhood. Set  $\tilde{V}$  is enlarged with two extra nodes, the source  $\mathbf{s}$  and sink  $\mathbf{t}$ ,  $V = \tilde{V} \cup \{\mathbf{s}, \mathbf{t}\}$ . Common approach is to represent the **object** by the  $\mathbf{s}$  node and the **background** by the  $\mathbf{t}$  node. Likewise, the edge set  $\tilde{E}$  is increased by the presence of these two nodes accordingly;  $E := \{\tilde{E} \cup \{(s, i), (i, t) | i \in \tilde{V}\}$ . Edges connecting neighbouring pixels with terminal nodes  $\mathbf{s}$  and  $\mathbf{t}$  are called **t-links**, while edges connecting only neighbouring image pixels are known as **n-links**. Moreover, a non-negative weight or a cost  $w_c$  is applied to each edge in the graph.

**Definition 23** (Network). *We call a directed weighted graph  $G = (V, E, w_c)$ , containing the terminal nodes  $\mathbf{s}$  and  $\mathbf{t}$ , with each edge having assigned a cost  $w_c(i, j) : E \rightarrow \mathbb{R}^+$ , a network. We denote this by  $N = (G, \mathbf{s}, \mathbf{t})$ .*

For binary labelling problems which can be expressed as max-flow problems, graph-cuts represent an efficient algorithm. If the energy function comprises of binary variables and it is submodular, then the instance can be solved using *graph-cuts* [76].

**Definition 24** (Submodularity). *We call a binary function of the form (2.29) submodular, if the following condition holds for every  $V_{p,q}$  term:*

$$V_{p,q}(0, 0) + V_{p,q}(1, 1) \leq V_{p,q}(0, 1) + V_{p,q}(1, 0).$$

When referring to a cut, we will refer to a subset of edges  $E_c \subset E$ . Each cut will have a different cost, defined by the sum of the weights on the edges of  $E_c$ :

$$\text{cost}(E_c) = \sum_{e \in E_c} w_c.$$

By performing a cut, the graph will be divided in two disjoint sets  $s$  and  $t$ , which contain all nodes connected to the source and sink, respectively. Fig. 2.10 gives a visual interpretation of such a cut.

Now, the question is how to find the best cut that minimizes a defined cost. This is known as the *s-t min-cut* problem.

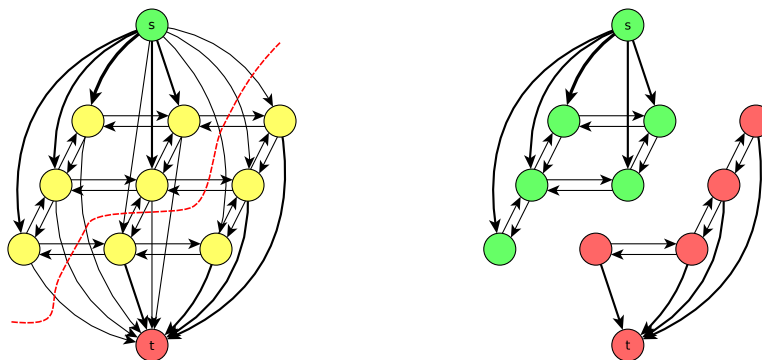


Figure 2.10: **Left**:example of a cut of a  $3 \times 3$  image. **Right**: resulting segmented image given the cut on the left side.

**Definition 25** (s-t min-cut problem). Let  $N = (G, s, t)$  be a network with a weighted directed graph  $G(V, E, w_c)$ .

An s-t **cut**  $C = (S, T)$  is a partition of  $V$  with  $s \in S$ ,  $t \in T$ ,  $S \cup T = V$  and  $S \cap T = \emptyset$ .

The **cut set**  $E_c$  of an s-t cut  $C$  is the set  $E_c := \{(i, j) \in E \mid i \in S, j \in T\} = (S \times T) \cap E$  with all outgoing edges from  $S$ .

The **min-cut problem** is finding the s-t cut  $E_c$  with minimum cost,  $\text{cost}(E_c)$ , among all possible s-t cuts, i.e.

$$\min_{E_c} \text{cost}(E_c).$$

The min-cut problem is closely related to the max-flow problem, the two being dual to each other [53].

### $\alpha$ -Expansion

Closely related to graph-cuts is the  $\alpha$ -expansion algorithm. It iteratively solves problems, by reducing a multi-valued variable optimization problem to a simpler, binary variable one. It is a *move* making method, in the sense that it allows for a large number of pixels to change their labels to a new label value  $\alpha$ . Finding the optimal multi-labelling of an image can be solved, if the associated energy function is submodular and if the pairwise term of (2.29) fulfils 3 constraints:

- $V(\alpha, \beta) = 0 \Leftrightarrow \alpha = \beta$  or  $V(\alpha, \beta) \neq 0 \Leftrightarrow \alpha \neq \beta$
- $V(\alpha, \beta) = V(\beta, \alpha) \geq 0$
- $V(\alpha, \beta) \leq V(\alpha, \gamma) + V(\gamma, \beta)$ .

If the pairwise term only meets the first two constraints, then it is called a *semi-metric* term. If all three are satisfied, the term is a *metric*.  $\alpha$  - expansion can be used only when the pairwise term is a *metric* term. If this is the case, then Boykov et. al. [15] showed that it is able to find a locally optimal solution at a known factor of the global minimum:

$$2c = 2 \max_{p,q \in E} \frac{\max_{\alpha \neq \beta} V(\alpha, \beta)}{\min_{\alpha \neq \beta} V(\alpha, \beta)}.$$

This factor,  $c$ , given as the ratio between the maximum and the minimum of the pairwise term  $V$ , implies that the local minimum found by  $\alpha$  - expansion will be at most double the global minimum  $\mathcal{E}^*$ .

---

**Algorithm 5**  $\alpha$ -expansion
 

---

- 1: Begin with arbitrary labelling  $f$ .
  - 2: Define a test variable  $change = false$ .
  - 3: **for** each label  $\alpha \in \mathcal{L}$  **do**
  - 4:   Find  $\hat{f} = \operatorname{argmin}_{f' \in S(f, \alpha)} E(f')$ ;
  - 5:   **if**  $E(\hat{f}) < E(f)$  **then**
  - 6:      $f = \hat{f}$ ;
  - 7:      $change = true$ ;
  - 8:   **end if**
  - 9: **end for**
  - 10: If  $change = true$ , go to 2.
  - 11: Return  $f$ .
- 

where  $S(f, \alpha)$ , represents the set of all possible labellings within one  $\alpha$  - expansion of  $f$ .

The overall idea of  $\alpha$  - expansion is to start with an initial arbitrary labelling. At the first iteration, one instance of graph cuts is performed, so as to arrive at the labelling that best minimizes the energy function. If the energy is lower than the current labelling, then this becomes the current labelling. When energy is no longer decreased, then the algorithm stops and returns the last known labelling  $f$ , that represents a local optimum. Alg. 5 summarizes as pseudocode this procedure.

## 2.2 Computed Tomography

Computed Tomography (CT) is a method of acquiring and processing cross-sectional images ("slices") in order to visualize the inner parts of spatial bodies without damaging their overall structure. For a "light-weight" interpretation of CT, one can consider the studied object to consist of a finite number of such

slices, each comprised of a predefined number of elements. For 3D cases, the notion of "volume elements" (or voxels) will be used, while for 2D cases, we will refer to "pixel elements". Each of these elements hold a particular information (gray value, absorption coefficient, etc.), that is stored in a digital image matrix (in the rest of this thesis, we name this matrix the "projection" or "measurement" matrix). In principle, a slice through an object can be obtained at any random orientation, as shown in Fig. 2.11 [72].

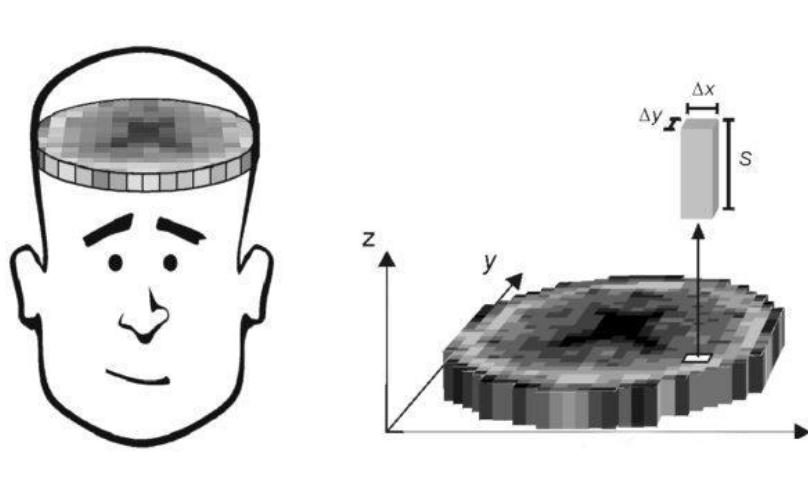


Figure 2.11: Cross-section through an object in the x-y plane. The slice has a thickness of  $s$  and each voxel is  $\Delta x$ ,  $\Delta y$  in size.

Every newly computed slice is considered to bring additional information about the object, thus the ideal set-up would consist of an increased number of these cross-sections. However, in numerous fields there are limitations to acquiring image data from a large number of angles (due to low exposure times to radiation allowed, the cost of the equipment involve), e.g. astronomic measurements of planets, seismic data, industrial quality inspection, etc. Reason for which, the amount of information available is diminished and the reconstruction suffers from artefacts. The area of research that focuses on the recovery of functions from few tomographic projections is called *Discrete tomography*. Feasibility of this severely ill-posed problem rests upon assumptions that: i) restrict the degrees of freedom of functions to be reconstructed and ii) these functions can only attain values from a finite set. Such problems are more suitable to be solved using iterative reconstruction algorithms, as it is possible to incorporate a-priori knowledge in order to better model the object that is studied. In recent period, *Discrete tomography* has shown potential for large-scale applications in various areas [97, 57] which also stimulates theoretical research. As advocated in [94], considering the problem of discrete tomography from the broader viewpoint of *compressive sensing* [2, 22]

enables to consider more general scenarios and to employ additional methods for investigating theoretical and practical aspects of discrete tomography. While the set of measurements (tomographic projections) is still “discrete” as opposed to the “continuous” theory of established tomographic settings [89], functions to be reconstructed are required to be compressible: a *sparse* representation exists such that few measurements of any function of some admissible class capture the degrees of freedom and enable recovery. Establishing corresponding sampling rates in connection with a given sparse representation and a model of the imaging sensor constitutes the main problem of mathematical research, which we deal with from Ch. 3 onwards. Before we dive into more theoretical aspects, we give in this chapter a short introduction into tomography, regarding the acquisition process in Sect. 2.2.1.1 and available imaging modalities in Sect. 2.2.1.2. In Sect. 2.2.2, a few words about two main algorithms (one continuous, *Filtered Back-Projection*, and one discrete, *Algebraic Reconstruction Technique*) that lay at the foundation of current reconstruction methods, are given. Continuing on the note of discrete reconstruction techniques, we outline in Sect. 2.2.3 several advances done in this area, from the 80’s until recently, in 2014, with approaches varying from iterative methods, to heuristics and even statistical methods to solve different tomography problems. The chapter concludes in Sect. 2.2.4 with an overview of tomography in industry, a place where it is becoming more and more attractive due to its non-invasive properties.

## 2.2.1 Established CT

### 2.2.1.1 Physics of CT

The CT acquisition process provides the user with data collected from different media, composing or surrounding the targeted area. Each of these media have particular physical properties that influence, in a positive or negative manner, the data to be processed.

For instance, a material having a high atomic number will possess a large *attenuation coefficient*, as well as for high density objects, due to their porous nature. Mathematically, intensity attenuation of an X-ray beam passing through an object, can be expressed according to the Beer-Lambert law:

$$I_t = I_0 \exp\left(-\sum_{i=1}^N \mu_i \Delta x\right), \quad (2.30)$$

where  $I_0$  represents the incident X-ray intensity,  $I_t$ , the outgoing X-ray intensity at a given time  $t$ ,  $\mu_i$  stands for the linear attenuation coefficient corresponding to each material and  $\Delta x$  gives the thickness of the material.

This formulation implies that X-ray intensities have an exponential decrease rate according to the material thickness  $\Delta x$  and the *linear absorption coefficient*  $\mu$ , as shown in Fig. 2.12. Physically, there are 2 type of absorption processes that can take place: the *photoelectric effect* and the *Compton effect*. A few words about these physical effects are in order.

*Compton effect* occurs when an incident photon hits the electron of an atom, dispersing it in a chaotic, randomized manner, resulting in *scattered photons* that do not provide any useful diagnostic information. Moreover, they are dangerous for the surrounding media as they contain a high amount of their original energy, leading to irradiations. This phenomenon, the Compton effect, is likely to happen when high energy photons are used in the diagnostic process.

*Photoelectric effect* on the other hand, relates to the emission of *electrons* from the surface of an object, as a response to the incident light. The higher the intensity of the incoming light, the more energy the electrons will have, when being emitted from the objects' surface. The chance of this type of interaction to occur, instead of the Compton effect, is high when the energy of the incoming photons is close to the energy binding the electron to the nucleus.

As a remark, elements with a higher atomic number have an increased chance of experiencing the photoelectric effect, at higher photon energies, whereas the adverse occurs in the Compton effect. That is, a high count of low atomic number elements are bound to respond to the incoming photons. Such subtleties play an important role in computed tomography.

In an ideal world, where one would be allowed to employ high radiation doses, have non-limited number of sensors, no movement and no scattering, then the CT images would be able to mirror the reality, exactly. However, any slight change in the *ideal* case, leads to unwanted artefacts, that burden the diagnosis process,

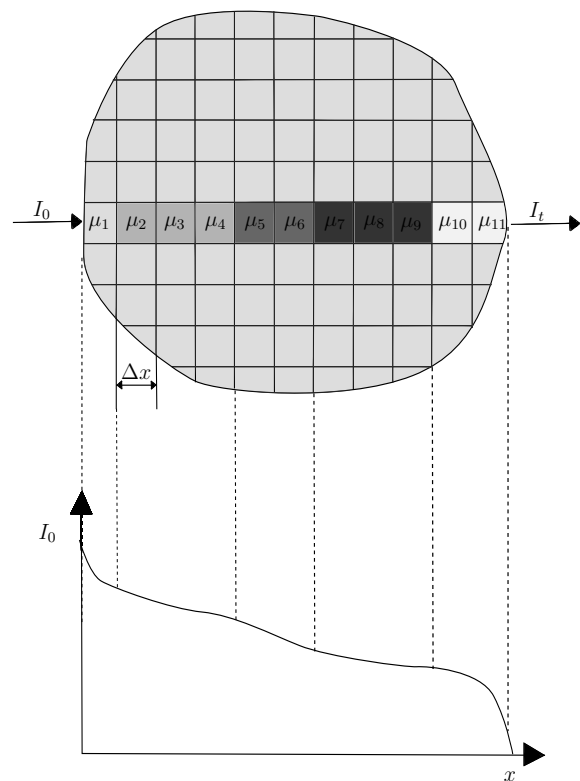


Figure 2.12: Exponential decrease of the X-ray intensity when passing through an object consisting of different media.

<sup>1</sup>[http://posterng.netkey.at/esr/viewing/index.php?module=viewing\\_poster&task=viewsection&pi=107494&ti=329481&searchkey=](http://posterng.netkey.at/esr/viewing/index.php?module=viewing_poster&task=viewsection&pi=107494&ti=329481&searchkey=)

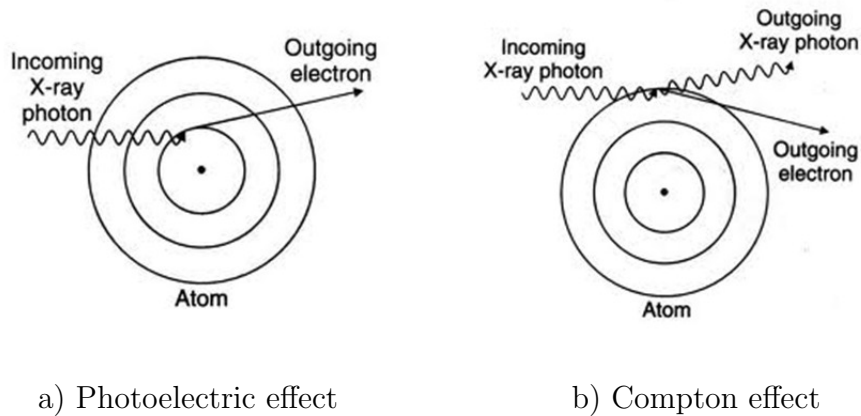


Figure 2.13: Two absorption processes<sup>1</sup> that are responsible of introducing noise in the data, during the acquisition process.

may it be from a medical point of view, or from a quality inspection routine. The most common artefacts encountered in industrial computed tomography are beam hardening (lower energy rays have an increased rate of being attenuated than higher energy rays), metal artefact, ring artefact (parts of the detector elements in a CT scanner are wrongly calibrated or defected) and image noise.

We introduced the physical aspect behind the acquisition process and how this is affected in practice. Next, we present the known possible configurations to acquire CT images, with regard to position of the sources and detectors, as well as the possible degrees of freedom involved, i.e. rotation or translation.

### 2.2.1.2 Imaging Modalities

Since the first appearance of CT scanners, scanning geometries have improved significantly in their process of acquiring X-ray data for image reconstruction. All these variations are classified according to the *generation* they belong to. Up to now, there are four known generations:

1. first generation used the same number of sources and detectors, that were placed opposite to each other and had a mechanically translate-rotate motion (see Fig. 2.14a);
2. the second generation of CT scanners used a small number of fan beams with multiple detectors, allowing multiple projections to be measured at the same time and still comprising of the mechanical movement of the source and detectors (see Fig. 2.14b);
3. third generation introduced the rotate-rotate motion of the sources and detectors. The geometry was the same as in Fig. 2.14b, the second generation,

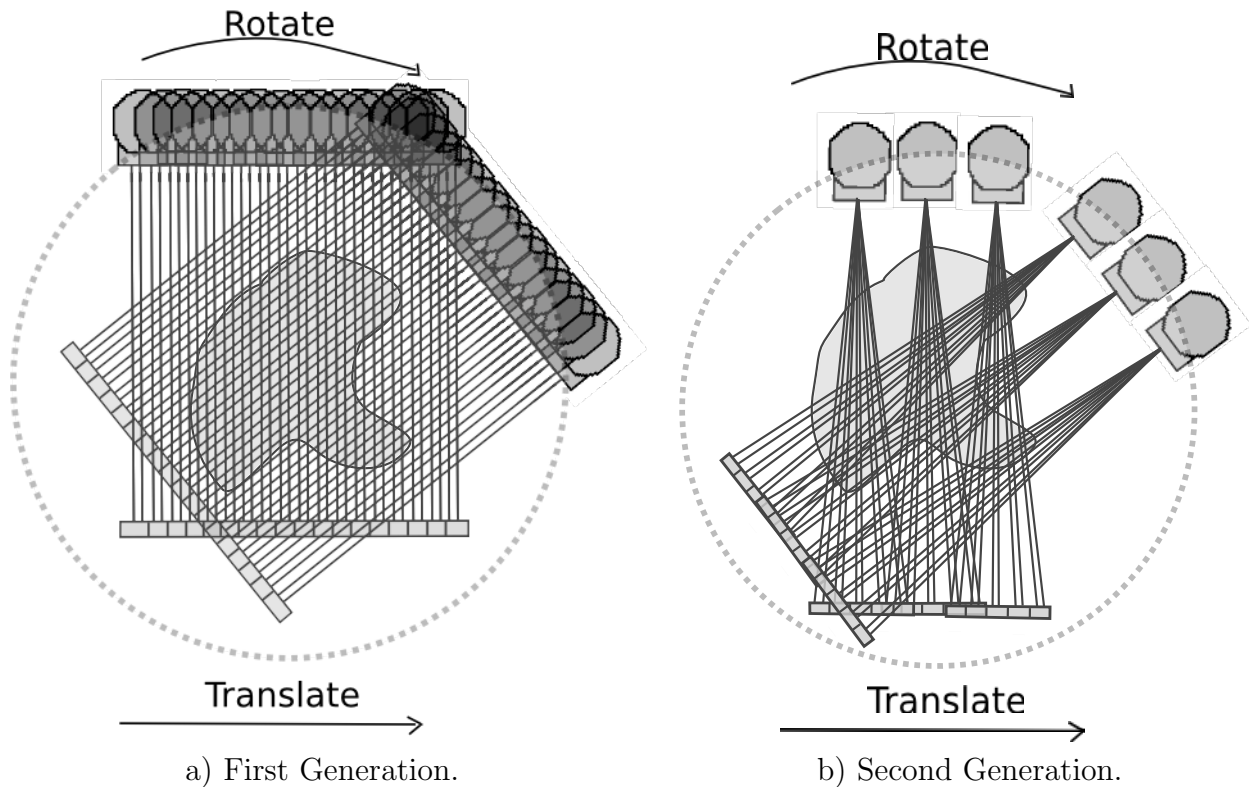


Figure 2.14: Acquisition geometry for first and second type generation of CT scanners.

but the advantage was that the sources and detectors rotated as one item, around the object (see Fig. 2.15a);

4. and the fourth generation of scanners comprised of a fixed ring of detectors surrounding the object. The beam source was the only moving part, at an angle, which activated certain detectors at a given scanning time (see Fig. 2.15b).

This thesis focuses on the simplest case of parallel beam geometries, as in the first generation of scanners, unless stated otherwise.

## 2.2.2 Discretization and Basic Recovery Schemes

In the course of this section, we present a number of reconstruction techniques, one that is highly used in practice (FBP) and others (ART methods) which provide the basis of more sophisticated techniques, presented and discussed in the remaining sections of this thesis. The content is merely intended to give the reader a flavour of what is used in different scenarios. Of course other techniques

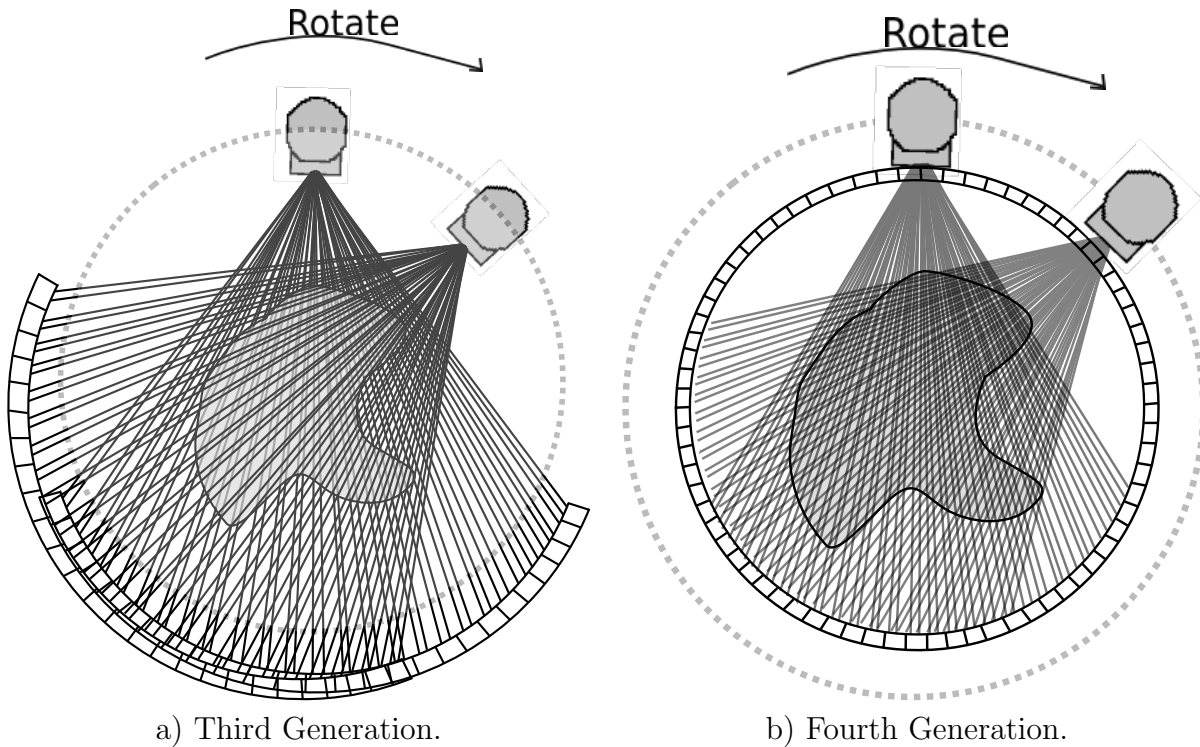


Figure 2.15: Acquisition geometry for third and fourth type generation of CT scanners.

are also investigated in the literature, but we restrict ourselves to what is relevant with respect to this thesis, i.e. discrete reconstruction methods.

### 2.2.2.1 Filtered Back-Projection

As part of the group of *analytical* reconstruction methods, *filtered backprojection (FBP)* is the most common algorithm currently implemented in practical applications. It returns satisfactory results, however, it has the drawback of requiring a *high amount of data* and it is highly unreliable when it comes to modelling artefacts in the reconstruction process.

We give the underlying mathematics behind FBP using a parallel beam setup. Mathematically, the acquisition process in X-ray tomography is closely related to the Radon transform (sinogram) of an object. Let us first define the object to be  $f : \mathbb{R}^2 \rightarrow \mathbb{R}$ . Making use of the  $\delta$  function, its Radon transform is

$$\mathcal{R}_{(\rho, \theta)}(f(x, y)) = \int_{-\infty}^{\infty} \int_{-\infty}^{\infty} f(x, y) \delta(x \cos \theta + y \sin \theta - \rho) dx dy.$$

This expression can be interpreted as being the line integral along a tomography beam, at a given orientation  $\theta$  and minimal distance  $\rho$  from the origin.

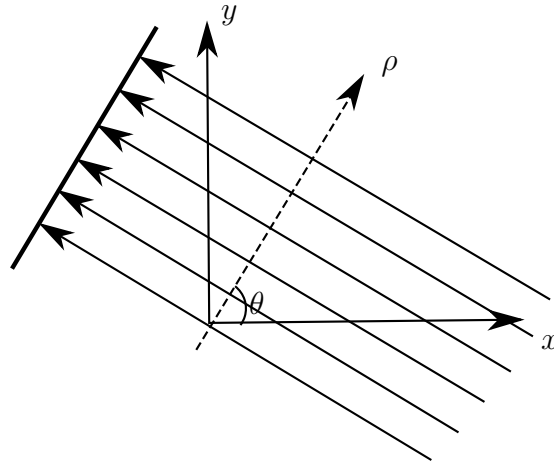


Figure 2.16: The Radon transform of each line in the parallel beam setup at a given angle  $\theta$  and distance  $\rho$  yields the projection of  $f$  at orientation  $\theta$ .

This transformation, in connection with the Fourier transform, lies at the foundation of the *projection-slice theorem*.

The Fourier transform of a two dimensional signal is expressed as

$$\mathcal{F}(\rho_x, \rho_y) = \int_{-\infty}^{\infty} \int_{-\infty}^{\infty} f(x, y) \exp^{-2\pi i(x\rho_x + y\rho_y)} dx dy.$$

**Theorem 2.2.1** (Projection-slice theorem). *Given a function  $f(x, y) : \mathbb{R}^2 \rightarrow \mathbb{R}$ , by performing the Fourier transform of the 2D signal, its value along a measurement line at a given angle  $\theta$  is equal to the 1D Fourier transform of the sinogram acquired at angle  $\theta$ .*

$$P(\rho, \theta) = \mathcal{F}(\rho \cos \theta, \rho \sin \theta)$$

A known fact about the inverse Radon transform is that it has bad performance with respect to noisy data; reason for which, in practice a more robust version is implemented, that involves the use of a high-pass filter.

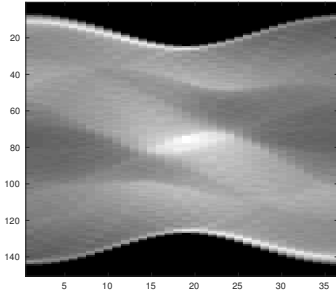
The base for the inverse Radon transform is given by the following identity:

$$f(x, y) = \hat{\mathcal{R}}(q * \mathcal{R}_{\rho, \theta}(f(x, y))),$$

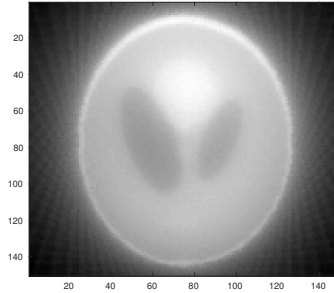
where  $q$  stands for a 1D filter,  $*$  denotes convolution and  $\hat{\mathcal{R}}$  is the backprojection operator

$$\hat{\mathcal{R}}(f(x, y)) = \int_0^\pi \left( \int_{-\infty}^{\infty} q(\omega) \mathcal{F}(f(x, y)) \exp^{2\pi i \omega (x \cos \theta + y \sin \theta)} d\omega \right) (x \cos \theta + y \sin \theta) d\theta.$$

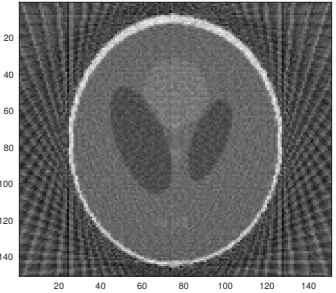
Because the backprojection routine results in a blurred image, the most common approach to alleviate this behaviour is to use a high-pass filter. The standard



Sinogram



Backprojection



Projection slice theorem



Original image

choice is Ram-Lak, however it has the tendency to amplify noise contained in the higher frequencies and thus, not improving the image quality by much. Other typical choices of filters would be Shepp-Logan, Hann, Generalized Hamming, cone filter, etc. In Horbert et. al.[108], the authors proposed a method in which the filtering operator is connected to the interpolation model, in such a way that it will result in only a single filtering operation. Results relate the fact that filter optimization improves reconstruction and is especially useful when computational speed is an important issue.

### 2.2.2.2 Algebraic Reconstruction Technique

Part of the *iterative* reconstruction algorithms, Algebraic Reconstruction Technique (ART) assumes that cross sections of the analysed object comprise of grids of unknowns. As the name suggests, algebraic equations need to be solved, so that the end result approximates well enough the measured projection data, i.e.

$$Ax = b, \tag{2.31}$$

where  $A \in \mathbb{R}^{m \times n}$  is the sensing matrix that models the acquisition process and  $x \in \mathbb{R}^n$  is the discrete set of unknowns that need to be reconstructed, given the set of measurements  $b \in \mathbb{R}^m$ .

When dealing with noise or other acquisition artefacts (beam hardening, ring artefacts, metal artefacts, motion), iterative methods have an advantage over

analytical ones. The user is able to include *a priori* information about the object, as constraints to the linear system, in order to improve the reconstruction.

### Computing the Measurements $b$

As stated earlier, the object considered is imaged as a square grid, divided into an  $n \times n$ , or  $n \times n \times n$  array of pixels or voxels, for 2D and 3D case, respectively. Each pixel/voxel in this grid, holds information about the material density of the object. The problem at hand is to estimate the value of these densities  $x$ , from a given set of measurements  $b$ . In synthetic experiments, these measurements  $b$  are obtained from what is called in the literature, *forward projection*. We give 3 possibilities to model these measurements, all of which can be considered as ray-driven approaches. That is, the measurements  $b$  are the result of the line-integral over the analysed volume:

- where the line integral is computed as a weighted sum of pixel values that have been crossed by the corresponding ray line. To each weight, the length of the intersection of the ray  $L_i$  with pixel  $x_j$  is attributed (see Fig.2.17a).
- where the end result is obtained as a weighted sum of bilinear interpolations, to compensate for deviations from the principal direction. When the main direction of the ray is on the  $x$ -axis, i.e. the largest absolute value of the following terms  $|x_1 - x_2|$ ,  $|y_1 - y_2|$ ,  $|z_1 - z_2|$ , is  $|x_1 - x_2|$ , then the weighting factor is given by

$$\frac{\sqrt{(x_1 - x_2)^2 + (y_1 - y_2)^2 + (z_1 - z_2)^2}}{|x_1 - x_2|}.$$

- as the result of a trilinear interpolation and the integral represents the sum at equally distance points along the projection ray.

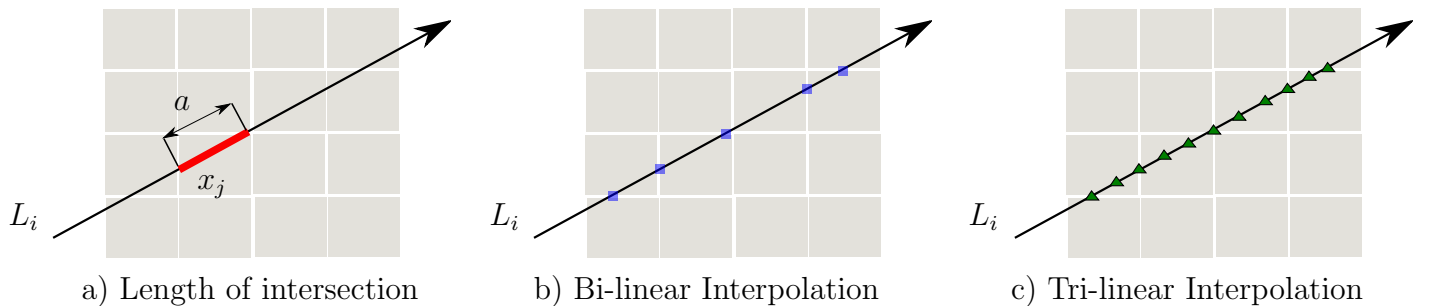


Figure 2.17: Interpolation schemes used in modelling the acquired measurements.

Method	Pros	Cons
Filtered Backprojection	<ul style="list-style-type: none"> <li>✔ fast to compute</li> <li>✔ direct formula for the inversion process</li> </ul>	<ul style="list-style-type: none"> <li>✘ modelling noise and other artefacts are not easy to do</li> <li>✘ much time to invest in proper filtering techniques</li> </ul>
Iterative methods	<ul style="list-style-type: none"> <li>✔ easy physical modelling of the object</li> <li>✔ easy adaptation to different imaging geometries</li> <li>✔ decreased radiation dose</li> </ul>	<ul style="list-style-type: none"> <li>✘ prolonged computation time</li> <li>✘ real-time reconstructions for large problem instances are much more difficult to realize</li> <li>✘ entire measurement area needs to be reconstructed</li> </ul>

Table 2.1: Comparison of analytical vs. iterative reconstruction methods.

For details, please read [113]. The most encountered case is the one where the line integral is calculated as a weighted sum, with weights given as the length of intersection between a ray and a pixel.

At the end of this section, we point out in Table 2.1, the advantages and disadvantages of the analytical methods vs. the iterative ones.

## 2.2.3 Discrete Tomography

### 2.2.3.1 Algebraic Reconstruction Technique

A widely known reconstruction method is the Kaczmarz method, firstly discovered by the Polish mathematician Stefan Kaczmarz, and brought back in attention in the area of image processing by Gabor Herman in the 1970s, from where it received the name *Algebraic Reconstruction Technique*.

From a geometrical point of view, each equation of the linear system (2.31) represents a hyperplane in the dimensional space of  $x$ . The unique solution is found to be at the intersection of all these hyperplanes. More precisely, starting with an initial guess,  $x_{(k,0)}$ , this is projected on the first hyperplane, resulting in a new point  $x_{(k,1)}$ . This point is further projected on the next equation in the system and so on.

Mathematically, this can be expressed as:

$$\begin{aligned}
 x_0^k &\rightarrow x_0^k - \frac{x_0^{k\top} a_1 - b_1}{a_1^\top a_1} a_1 = x_1^k, \\
 x_1^k &\rightarrow x_1^k - \frac{x_1^{k\top} a_2 - b_2}{a_2^\top a_2} a_2 = x_2^k, \\
 x_{I-1}^k &\rightarrow x_{I-1}^k - \frac{x_{I-1}^{k\top} a_I - b_I}{a_I^\top a_I} a_I = x_0^{(k+1)},
 \end{aligned} \tag{2.32}$$

with  $a_i$  the  $i$ -th row of  $A$  and  $x_{(k,1)}, x_{(k,2)}, \dots$  the first, second, etc., hyperplane at iteration  $k$ .

After passing through all the equations (hyperplanes), the last projected point is projected back onto the first equation and the process repeats until a unique solution is found, at the intersection of all hyperplanes. This behaviour in turn, exemplifies the fact that all ART type methods are *iterative* methods. They are known to converge rapidly when analysed in the root-mean squared error criterion, but the end result of the reconstruction suffers highly from salt and pepper noise, as will be seen in Fig. 2.19. In the presence of noise, the system  $Ax = b$  is likely to be inconsistent, and a more appropriate constraint then is  $\|Ax - b\| \leq \varepsilon$ .

Few adaptations of the Kaczmarz method exist:

1. **symmetric Kaczmarz**, where the equations are available in  $1, \dots, m$  order, then from  $m - 1$  to  $1$ , restarting from  $2$  to  $m$  and so on.
2. **randomized Kaczmarz**, where the hyperplane  $i$  on which to project is randomly chosen from  $[m]$  hyperplanes, with a probability proportional to  $\|a_i\|_2^2$ .
3. **Simultaneous ART (SART)**, where in order to update the solution  $x$ , a subset of ray sums belonging to a specific projection angle is taken into consideration. This offers the method a computational advantage over the traditional sequential ART method.

$$x_j^{k+1} = x_j^k - \frac{1}{\sum_{i=1}^m |a_{ij}|} \sum_{i=1}^m \frac{a_{ij}}{\sum_{j=1}^n |a_{ij}|} (a_i x^k - b_i), \quad j = 1, \dots, n. \tag{2.33}$$

An empirical study of the performance of these methods with respect to a relaxation parameter is given by Kazemi et. al. [74]. By choosing larger values of the relaxation parameter, ART methods have the tendency to converge faster, but to reach a noisy reconstruction in the end, while a smaller value of the parameter leads to smoother images, but the convergence rate is lowered significantly. Using a heuristic to find the *optimal* parameter value for each of the Kaczmarz variants, the authors concluded that a "good" assessment of the relaxation parameter is not related to the image size, nor to the type of used image.

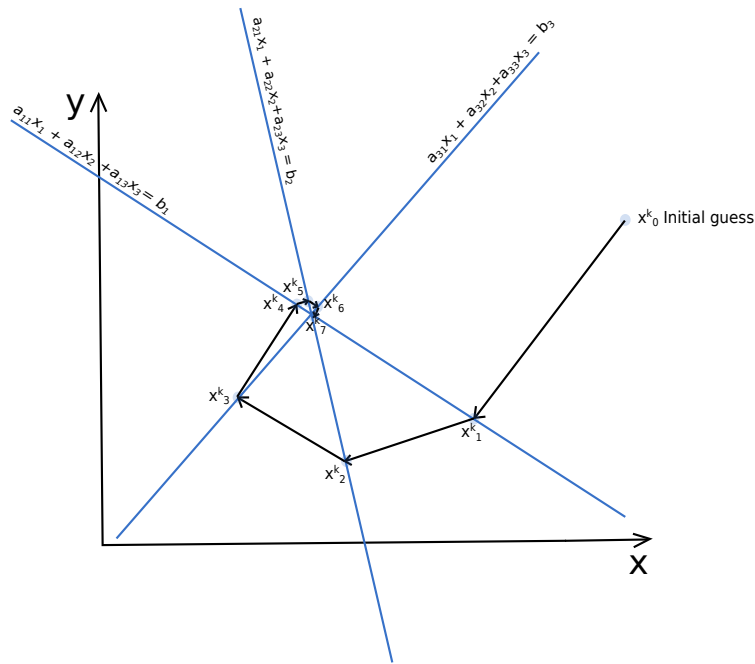


Figure 2.18: Algebraic reconstruction technique principle in 2D, for a  $3 \times 3$  matrix  $A$ .

### 2.2.3.2 Simultaneous Iterative Reconstruction Technique

In the SIRT methods, the approach is to simultaneously update the equations, no matter the order of the hyperplanes, in order to correct for errors. Specifically, it corrects all rows of the linear system using the current approximation and then it averages the result over all corrections. Unlike ART, the resulting images are smoother (see Fig. 2.20), but the time required for these methods to reach convergence increases.

There are several algorithms which fall in this category, from which we mention:

1. the **Cimmino** method [24], in which the projection routine of the current vector  $x^k$  is done onto *all* hyperplanes, and the end result comes after an averaging procedure, with equal weights,  $m$ , for each equation.

$$x^{k+1} = x^k + \lambda_k A^\top D(b - Ax^k),$$

where  $b = b_i \in \mathbb{R}^m$  and  $D = \frac{1}{m} \text{diag} \left( \frac{1}{\|a_1\|_2^2}, \frac{1}{\|a_2\|_2^2}, \dots, \frac{1}{\|a_m\|_2^2} \right)$ .

2. the **Landweber** method [77], with the iterative step

$$x^{k+1} = x^k + \gamma A^\dagger (b - Ax^k), \quad (2.34)$$

where  $0 < \gamma < 2/\lambda_{max}$ ,  $\gamma$  being a gain factor for influencing the convergence rate and  $\lambda_{max}$  representing the largest eigenvalue of the nonnegative matrix  $A^\dagger A$ . When initialized with  $x = 0$ , the iterations converge to the minimum norm least-squares solution.

3. **DROP** (Diagonal Relaxed Orthogonal Projections) [25], a modified version of Cimmino's method. Instead of using equal weights for each linear equation, the main idea is to divide the iterative step by the number of nonzero elements in the column  $j$ , denoted hereafter by  $s_j$ , of matrix  $A \in \mathbb{R}^{m \times n}$  and use orthogonal projections onto the corresponding hyperplanes. The update equation would read:

$$x_j^{k+1} = x_j^k - \frac{\lambda_k}{s_j} \sum_{i=1}^m \frac{a_i, x^k - b_i}{\|a_i\|_2^2} a_{ij}, \quad \text{for } j = 1, 2, \dots, n.$$

The values of  $s_j$  will be much smaller than  $m$ , improving the algorithms' convergence speed.

4. **CAV** (Component Averaging), an extension of DROP, where each orthogonal projection is replaced by a generalized oblique projection. For more details, we refer the reader to the paper of Censor et. al. [26].

### 2.2.3.3 (Soft) Discrete Algebraic Reconstruction Technique

Introduced as a fast heuristic algorithm, DART [6] serves in reconstructing binary images, by assuming object homogeneity, as prior knowledge. The algorithm alternates between an iterative algebraic method (SIRT) for continuous tomography to obtain an initial reconstruction and a segmentation step applied to a set of boundary pixels, in order to constrain the image to the desired range of gray values.

However, considering more complicated objects with several transitions (holes), proved to be rather challenging. Moreover, the authors do not relate any objective function to the idea behind this method and they show experiments displaying the weakness of the method with regard to different noise levels .

To overcome this limitation, Bleichrodt et. al. [9] improved the method by imposing soft constraints on pixel values, in order to permit the noise to spread all over the image domain, not only on boundary areas.

### 2.2.3.4 Maximum a Posteriori X-ray Computed Tomography Using Graph Cuts

Based on maximum a posteriori estimation, Maeda et. al. [83] handles the tomographic reconstruction problem from a statistical point of view. By supposing

that the user already knows how many materials there are in the object, they are able to use this information as a prior, leading to smooth solutions and allowing the existence of objects that have a high attenuation coefficient, such as metal. The objective function to be minimized is:

$$p(x, v | \mathcal{D}) \propto p(\mathcal{D} | x) p(x | v) p(v) \\ \Rightarrow E(x, v) = -\ln p(\mathcal{D} | x) - \ln p(x | v) - \ln p(v),$$

where  $x$  is the tomographic image,  $v = \{v_1, v_2, \dots, v_J\}$  is the labelled version of the tomographic image,  $J$  is the number of pixels and  $\mathcal{D}$  denotes the set of projections.

The proposed algorithm intends to optimize  $E(x, v)$  in an alternating fashion, considering the *scaled conjugate gradient* method for the continuous minimization, i.e. minimization wrt. to  $x$ , and graph cuts (see Sect. 2.1.3.2) for the discrete minimization wrt. to  $v$ .

Results using this approach have shown to be effective under low number of projections and the presence of metal artefacts.

## 2.2.4 Applications in Industry (Non-Destructive Testing)

Many industrial applications nowadays rely on CT methods to perform quality inspection on manufactured parts. Automotive, aviation and motorcycle industries together with their suppliers show a keen interest in the developments that can be achieved using this technique. The ability to see the inner structure of an object in its natural functioning position without requiring destructive testing is highly beneficial for companies, both from a financial and a time point of view.

Other non-destructive methods are also currently widely used, such as tactile or optical methods. However, tactile methods have the disadvantage that they can deform the object during measurements, while CT is a non-intrusive approach and in contrast to optical methods, CT inspection does not suffer from surface reflection. Moreover, these two approaches, tactile and optical testing, are only used for surface testing. CT has the advantage that it can also look inside the object, without performing any structural damage to it.

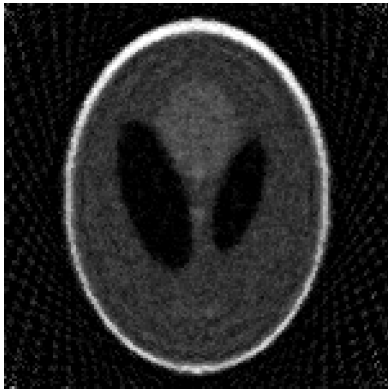
Failure analysis, assemblies inspection, investigations concerning material properties (porosity) or dimensional and geometrical measurements are a few applications that benefit from CT methods. The usual work flow of quality inspection is to perform the CT scan (in 3D) of the object and then reference it to an already existing CAD (computer aided design) model to detect irregularities.

<sup>2</sup>[http://www.dgzfp.de/Portals/24/PDFs/BBonline/bb\\_67-CD/bb67\\_v08.pdf](http://www.dgzfp.de/Portals/24/PDFs/BBonline/bb_67-CD/bb67_v08.pdf)

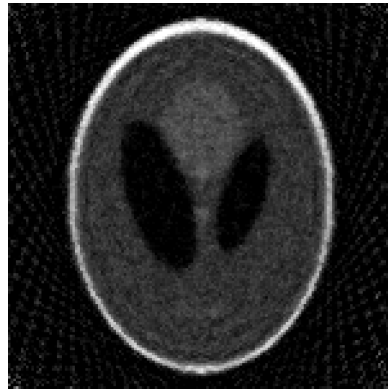
<sup>3</sup><https://grabcad.com/library/diesel-motorcycle-engine/files/Renderings/cylinderhead92mmChamb18Mar07.SLDPRT>

<sup>4</sup><https://grabcad.com/library/diesel-motorcycle-engine/files/Renderings/cylinderhead92mmChamb18Mar07.SLDPRT>

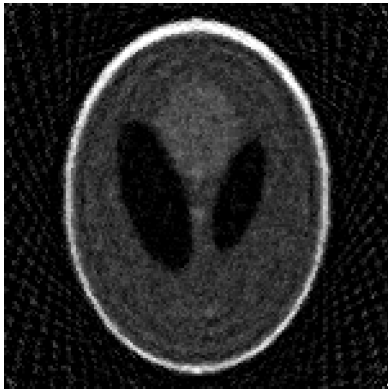
Moreover, in industry, unlike medicine, objects tend to be relatively simple and to have a predefined geometry, which can be mathematically modelled to improve the overall reconstruction process. One of the main objectives of industrial image processing is to increase the autonomy of the machines up to independent functioning. This is not possible, for example, in the medical field, where the computer only has the role to assist the doctor in the treatment and diagnostic phase of his patients.



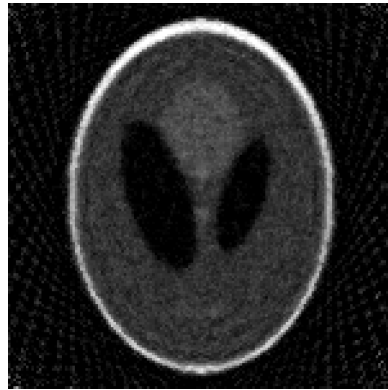
(a) Kaczmarz, SNR = 6.6610.



(b) Symmetric Kaczmarz, SNR = 6.6751.



(c) Randomized Kaczmarz, SNR = 6.2396.

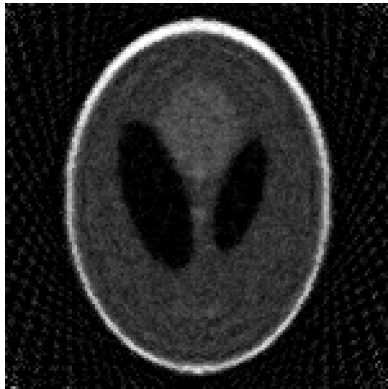


(d) SART, SNR = 6.7066.



(e) Original image.

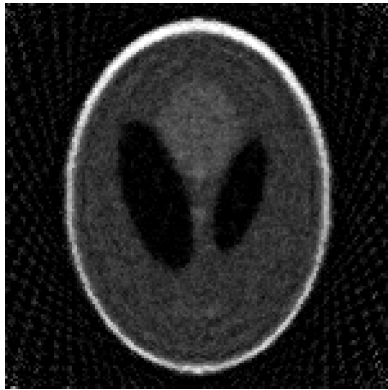
Figure 2.19: Behaviour of Algebraic Reconstruction Techniques (ART) for a tomographic problem of size  $150 \times 150$ , from 36 angles, equally distributed around a  $180^\circ$  angular range, with added random Gaussian noise to the right hand side vector  $b$ . The algorithms ended when the Normalized Cumulative Periodogram (NCP) criterion was fulfilled, using parallel beam tomography setup.



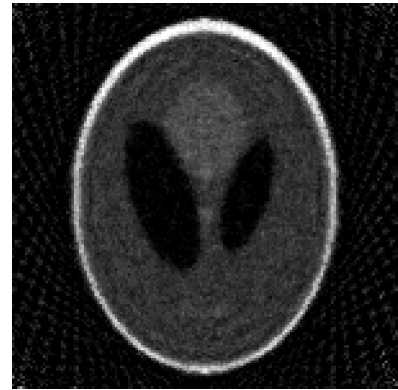
(a) Cimmino, SNR = 6.6813.



(b) Landweber, SNR = 6.9919.



(c) CAV, SNR = 6.6803.



(d) DROP, SNR = 6.6485.



(e) Original image.

Figure 2.20: Behaviour of Simultaneous Iterative Reconstruction Techniques (SIRT) for a tomographic problem of size  $150 \times 150$ , from 36 angles, equally distributed around a  $180^\circ$  angular range, with added random Gaussian noise to the right hand side vector  $b$ . The algorithms ended when the Normalized Cumulative Periodogram (NCP) criterion was fulfilled, using parallel beam tomography setup.

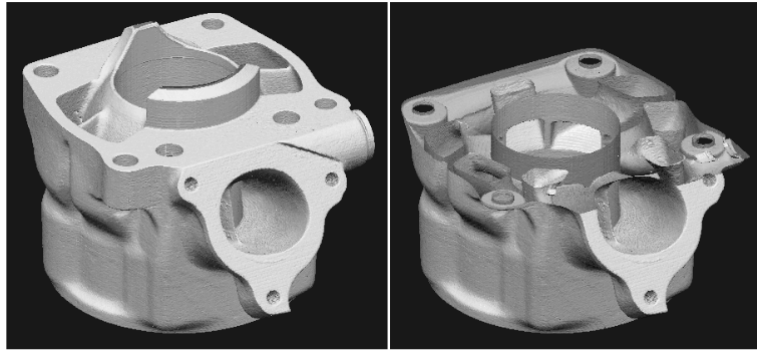


Figure 2.21: Motorcycle engine cylinder<sup>2</sup>: 3D visualisation of whole and cut tomogram

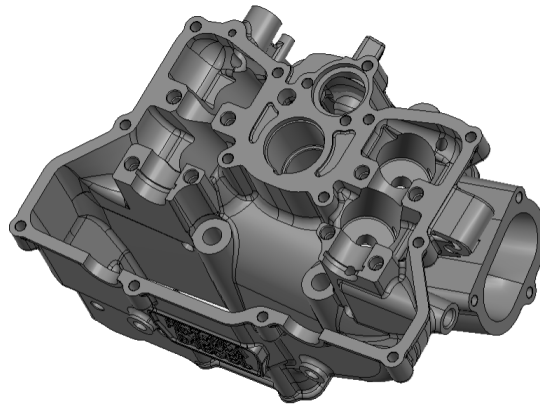


Figure 2.22: Motorcycle engine cylinder<sup>3</sup>: 3D CAD visualisation

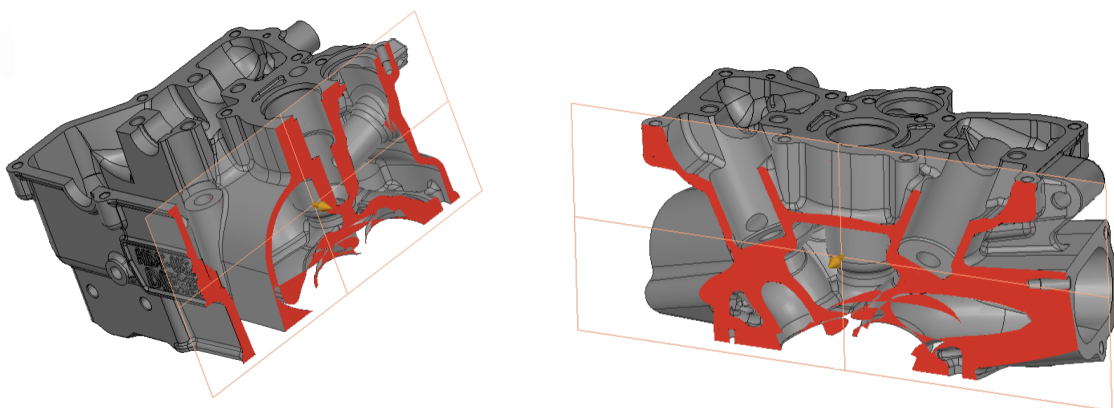


Figure 2.23: Motorcycle engine cylinder<sup>4</sup>: **Left**: CAD visualization - X cross section, **Right**: CAD visualization - Z cross section.

---

---

## CHAPTER 3

---

# CORRECT RECOVERY AND PHASE TRANSITIONS

In this chapter, we study unique recovery of cosparse signals from limited-angle tomographic measurements of two- and three-dimensional domains. More precisely, of compound solid bodies as depicted in Fig. 3.1.

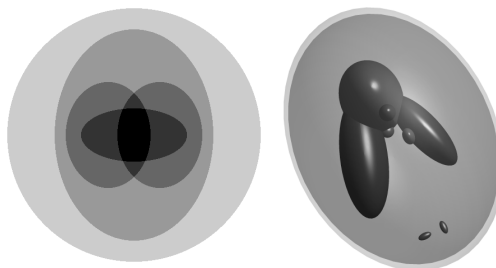


Figure 3.1: The left figure sketches the class of compound solid bodies considered in this chapter for reconstruction from few tomographic projections. These objects are similar to the 3D Shepp-Logan phantom (right) and are composed of different materials in a homogeneous way, but with unknown geometry. *The gradient of the piecewise constant intensity function is sparse.*

We adopt the recently introduced *cosparse analysis model* from [87], that provides an alternative viewpoint to the classical *synthesis model* and is more suitable to the problem class considered in this chapter. The current work applies and extends the results from [87] to the 3D recovery problem from few tomographic projections of three-dimensional images consisting of few homogeneous regions.

We give a theoretical relation between the image *cosparsity* and sufficient sampling, validate it empirically and conclude that TV-reconstructions of a class of synthetic phantoms exhibit a well-defined recovery curve similar to the study in [95, 96].

The content is structured as following: Section 3.1 characterizes the imaging scenarios considered in this chapter and throughout this thesis, unless stated otherwise, from the viewpoint of compressive sensing. We work out in more detail in Section 3.2 that the required assumptions in [91] do not imply relevant recovery guarantees for the discrete tomography set-ups considered here. In Section 3.3, we adopt the cospars analysis model [87] and generalize corresponding results to the practically relevant three-dimensional case. Aspects of the linear programming formulation used to solve problem (3.7), are examined in Section 3.4. A comprehensive numerical study underpinning our results is reported in Section 3.5. We conclude in Section 3.6.

The signals which we will be handling,  $u(x), x \in \Omega \subset \mathbb{R}^d, d \in \{2, 3\}$  are discretized as follows.  $\Omega$  is assumed to be a rectangular cuboid covered by a *regular grid graph*  $G = (V, E)$  of size  $|V| = n$ . Accordingly, we identify  $V = \prod_{i \in [d]} [n_i]_0 \subset \mathbb{Z}^d$ ,  $n_i \in \mathbb{N}$ . Thus, vertices  $v \in V$  are indexed by  $(i, j)^\top \in \mathbb{Z}^2$  and  $(i, j, k)^\top \in \mathbb{Z}^3$  in the case  $d = 2$  and  $d = 3$ , respectively, with ranges  $i \in [n_1]_0, j \in [n_2]_0, k \in [n_3]_0$ , and

$$n = n_1 n_2 n_3. \quad (3.1)$$

As a result, discretization of  $u(x)$ ,  $x \in \Omega$ , yields the vector  $u \in \mathbb{R}^n$ , where we keep the symbol  $u$  for simplicity.

Two vertices  $v_1, v_2 \in V$  are adjacent, i.e. form an edge  $e = (v_1, v_2) \in E$ , if  $\|v_1 - v_2\|_1 = 1$ . We also denote this by  $v_1 \sim v_2$ .

**Remark 3.0.1.** Informally speaking,  $G$  corresponds to the *regular pixel or voxel grid* in 2D and 3D, respectively.

Consider the one-dimensional discrete derivative operator

$$\partial: \mathbb{R}^m \rightarrow \mathbb{R}^{m-1}, \quad \partial_{i,j} = \begin{cases} -1, & i = j, \\ +1, & j = i + 1, \\ 0, & \text{otherwise.} \end{cases} \quad (3.2)$$

Forming corresponding operators  $\partial_1, \partial_2, \partial_3$  for each coordinate, conforming to the ranges of  $i \in [n_1]_0, j \in [n_2]_0, k \in [n_3]_0$ , and  $n = n_1 n_2 n_3$ , such that  $(i, j, k) \in V$ , we obtain the discrete gradient operator

$$\nabla = \begin{pmatrix} \partial_1 \otimes I_2 \otimes I_3 \\ I_1 \otimes \partial_2 \otimes I_3 \\ I_1 \otimes I_2 \otimes \partial_3 \end{pmatrix} \in \mathbb{R}^{p \times n}, \quad (3.3)$$

where  $\otimes$  denotes the Kronecker product and  $I_i$ ,  $i = 1, 2, 3$ , are identity matrices with appropriate dimensions. The *anisotropic* discretized TV-measure is given by

$$\text{TV}(u) := \|\nabla u\|_1. \quad (3.4)$$

The key assumption made through out this chapter is that *gradients* of functions to be reconstructed are sufficiently *sparse*.

As a consequence, if the linear system  $Au = b$  represents the tomographic imaging set-up with given measurements  $b \in \mathbb{R}^m$ , then the standard  $\ell_1$ -minimization approach

$$\min \|u\|_1 \quad \text{s.t.} \quad Au = b, \quad (3.5)$$

does not apply, because  $u$  itself is *not* sparse. We consider instead, the *total variation* criterion

$$\min_u \text{TV}(u) \quad \text{s.t.} \quad Au = b, \quad (3.6)$$

and its *nonnegative* counterpart

$$\min_u \text{TV}(u) \quad \text{s.t.} \quad Au = b, \quad u \geq 0, \quad (3.7)$$

that in the continuous case returns the  $(d - 1)$ -dimensional Hausdorff measure of discontinuities of indicator functions [120], with numerous applications in mathematical imaging [101]. This provides the natural sparse representation of the class of functions considered here (cf. Fig. 3.1). Our objective in this chapter is to establish sampling rates that enable the recovery of  $u$  as solution to the optimization problem (3.6) or (3.7).

For industrial applications additionally motivating our work, we refer to e.g. [23, 58]. In this context, scenarios of *limited-angle tomography* are relevant to our work as they enable minimization of acquisition time and related errors, affecting the quality of projection measurements and in turn, object reconstruction.

### 3.1 Tomographic Sensing Matrices

Depending on the application, different scanning geometries are used in CT imaging, as mentioned in Sect. 2.2.1.2. In the present work, we adopt a simple discretized model based on an image  $u(x)$ ,  $x \in \Omega \subset \mathbb{R}^d$ ,  $d \in \{2, 3\}$ , that represents the inhomogeneity of  $\Omega$  and consists of an array of unknown densities  $u_j$ ,  $j \in [n]$ . The model comprises algebraic equations for these unknowns in terms of measured projection data. To set up these equations, the sensing device measures line integrals of the object attenuation coefficient along X-rays  $L_i$ ,  $i \in [m]$ , along some known orientations. The  $i$ -th corresponding measurement obeys

$$b_i := \int_{L_i} u(x) dx \approx \sum_{j=1}^n u_j \int_{L_i} \mathcal{B}_j(x) dx = \sum_{j=1}^n u_j A_{ij}. \quad (3.8)$$

The values  $A_{ij}$  that form the *measurement or projection matrix*  $A$ , depend on the choice of the basis function. We assume  $\mathcal{B}_j$  are cube- or square-shaped uniform basis functions, the classical *voxel* in 3D or *pixel* in 2D.

The main task studied in this chapter concerns estimation of the weights  $u_j$  from the recorded measurements  $b_i$  and solving the noiseless setting  $Au = b$ . The matrix  $A$  has dimensions ( $\#$  rays  $=: m$ )  $\times$  ( $\#$  voxel/pixel  $=: n$ ), where  $m \ll n$ . Since the projection matrix encodes the incident relation between rays and voxels/pixels, the projection matrix  $A$  will be sparse. Based on additional assumptions on  $u$ , we will devise conditions for exact recovery of  $u$  from the *underdetermined* linear system  $Au = b$ .

### 3.1.1 Imaging Set-Up

For simplicity, we will assume that  $\Omega$  is a cube in 3D or a square in 2D and that  $\Omega = [0, d]^3$  is discretized into  $d^3$  voxels, while  $\Omega = [0, d]^2$  is discretized into  $d^2$  pixels. We consider a parallel ray geometry and choose the projection angles such that the intersection of each line with all adjacent cells is constant, thus yielding binary projection matrices after scaling. This simplification is merely made in order to obtain a structure in the projection matrix which allows to compute relevant combinatorial measures. We stress however that other discretization choices are possible and lead to similar results.

#### 2D Case: 3, ..., 8 Projection Directions

We set  $\Omega = [0, d]^2$  and obtain the binary projection matrices according to (3.8) from few projecting directions (three to eight), compare Fig. 3.2. We summarize the used parameters in Table 3.1.

# proj. dir.	$m$	$n$	projection angles
3	$4d - 1$	$d^2$	$0^\circ, 90^\circ, 45^\circ$
4	$6d - 2$	$d^2$	$0^\circ, 90^\circ, \mp 45^\circ$
5	$7d + \lfloor \frac{d}{2} \rfloor - 2$	$d^2$	$0^\circ, 90^\circ, \mp 45^\circ, \arctan(2)$
6	$8d + 2\lfloor \frac{d}{2} \rfloor - 2$	$d^2$	$0^\circ, 90^\circ, \mp 45^\circ, \mp \arctan(2)$
7	$9d + 3\lfloor \frac{d}{2} \rfloor - 2$	$d^2$	$0^\circ, 90^\circ, \mp 45^\circ, \mp \arctan(2), \arctan(0.5)$
8	$10d + 4\lfloor \frac{d}{2} \rfloor - 2$	$d^2$	$0^\circ, 90^\circ, \mp 45^\circ, \mp \arctan(2), \mp \arctan(0.5)$

Table 3.1: Dimensions of projection matrices in 2D.

#### 3D Case: 3 or 4 Projection Directions

We consider the imaging set-up depicted by Fig. 3.3 and Fig. 3.4. The projection angles were chosen again such that the intersection of each ray with all adjacent

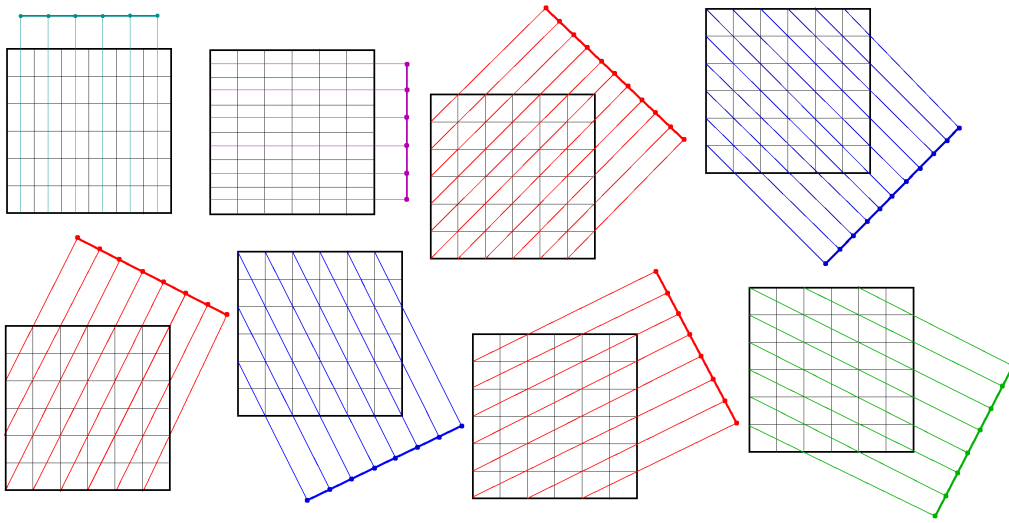


Figure 3.2: Eight different projecting directions along with projecting rays for  $90^\circ$ ,  $0^\circ$ ,  $\mp 45^\circ$ ,  $\mp \arctan(2)$ , and  $\mp \arctan(0.5)$  (from left to right, top to bottom). Note that the intersection segments for each projection ray with all adjacent pixel are equal. As a consequence, we obtain after appropriate scaling, binary projection matrices. Each sensor resolution varies with the projection angle, however. The illustration above depicts  $\Omega = [0, d]^2$  with  $d = 6$ .

voxels is constant. After appropriate scaling the resulting measurement matrices are binary as well.

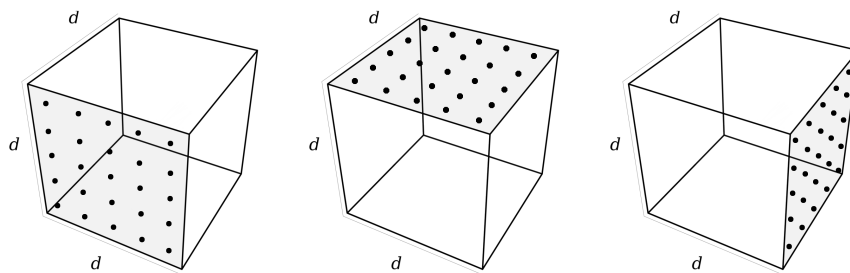


Figure 3.3: Imaging set-up for three orthogonal projections corresponding to each shaded plane of the cube. From left to right: Cell centers projected along each direction are shown as dots for the case  $d = 5$ . The cube  $\Omega = [0, d]^3$  is discretized into  $d^3$  cells and projected along  $3 \cdot d^2$  rays.

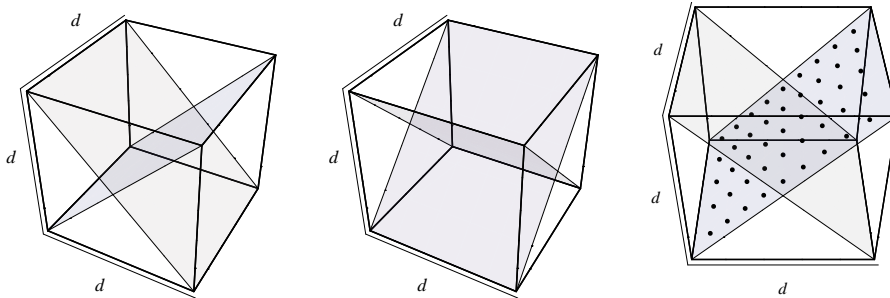


Figure 3.4: Imaging set-up for four projecting directions corresponding to the image planes shown as two pairs in the left and center panel respectively. Right panel: Voxel centers projected onto the first image plane are shown as dots for the case  $d = 5$ . The cube  $\Omega = [0, d]^3$  is discretized into  $d^3$  voxel and projected along  $4 \cdot d(2d - 1)$  rays.

It has been shown in [30] that binary matrices cannot satisfy  $RIP_{\delta,k}$  unless the numbers of rows is  $\Omega(k^2)$ .

**Theorem 3.1.1.** [30, Thm. 1] Let  $A \in \mathbb{R}^{m \times n}$  be any 0/1-matrix that satisfies  $RIP_{\delta,k}$ . Then

$$m \geq \min \left\{ \left( \frac{1 - \delta}{1 + \delta} \right)^2 k^2, \frac{1 - \delta}{1 + \delta} n \right\} .$$

Taking into account that there exists  $\text{spark}(A)$ -columns in  $A$  which are linearly dependent, we obtain, together with  $m \ll n$ , the following result.

**Corollary 3.1.2.** Let  $\delta \in (0, 1)$ . A necessary condition for  $A$  to satisfy the  $RIP_{\delta,k}$  for all  $k$ -sparse vectors is that

$$k \leq \min \left\{ \frac{1 + \delta}{1 - \delta} m^{\frac{1}{2}}, \text{spark}(A) - 1 \right\} .$$

### 3.1.2 Application to Considered Scenarios

For our particular matrices  $A$  defined in Sect. 3.1.1 we obtain, along the lines of [94, Prop. 3.2], that  $\text{spark}(A)$  is a constant for all dimensions  $d$  with  $m < n$ , while the number of measurements obeys  $O(d^{d-1})$ ,  $d \in \{2, 3\}$ . Compare also Fig. 3.5, left. However, we cannot be sure that  $A$  possesses the  $RIP_{\sqrt{2}-1, \sigma}$ , with  $\sigma = \text{spark}(A) - 1$ , unless we compute the singular values of all submatrices containing  $\sigma$  or less columns of  $A$ .

From the viewpoint of CS, the poor properties of  $A$  rest upon the small  $\text{spark}$  of  $A$ . In order to increase the maximal number of columns such that all column collections of size  $k$  (or less) are linearly independent, we can add to the entries of  $A$  small random numbers. Due to the fact that  $\text{rank}(A)$  almost equals  $m$

in all considered situations, the probability that  $k$ -arbitrary columns are linearly independent slowly decreases from 1, when  $k < \text{spark}(A)$ , to 0, when  $k > \text{rank}(A)$ . The perturbed matrix  $\tilde{A}$  is computed by uniformly perturbing the non-zero entries  $A_{ij} > 0$  to obtain  $\tilde{A}_{ij} \in [A_{ij} - \epsilon, A_{ij} + \epsilon]$ , and by normalizing subsequently all column vectors of  $\tilde{A}$ . In practice, such perturbations can be implemented by discretizing the image by different basis functions or choose their locations on an irregular grid.

As illustrated by Figure 3.1, considering functions  $u(x)$  with sparse gradients and the corresponding optimization criterion  $\text{TV}(u)$  for recovery (3.6), we may boost recovery performance in severely undersampled tomographic scenarios, despite the poor properties of measurement matrices  $A$ .

## 3.2 Sparsity and TV-Based Reconstruction

It has been well known empirically that solving the problem

$$\min \|\nabla u\|_1 \quad \text{s.t.} \quad \|Au - b\|_2 \leq \varepsilon \quad (3.9)$$

can provide high-quality and stable image recovery. Until the recent work [91], however, it had been an open problem to offer provable *theoretical* guarantees, beyond incomplete Fourier measurements [21, 20]. The gradient operator  $\nabla$  is not an orthonormal basis or a tight frame, thus neither the standard theory of CS nor the theoretical extensions in [18] concerning the *analysis model* apply to (3.9), even for images with truly sparse gradient  $\nabla u$ .

The recent work [91, 90] *proves* that stable recovery is possible via the convex program (3.9) and considers a general matrix  $A$  which is incoherent with the multidimensional Haar wavelet transform and satisfies a RIP condition. The Haar wavelet transform provides a sparsifying basis for 2D and 3D images and is closely related to the discrete gradient operator. In the remainder of this section, we denote the discrete multidimensional Haar wavelet transform by  $H$  and refer the reader to the definition of [90, p. 6]. The following theorem summarizes the main results of [91, Thm. 5, Thm. 6], and [90] and specializes them to the case of *anisotropic* TV (3.4) as considered in the present chapter, see also the remarks following [91, Thm. 6] and [90, Main Thm.].

**Theorem 3.2.1.** *Let  $d = 2^N$  be a power of two and  $n = d^{\text{d}}$ ,  $\text{d} \in \{2, 3\}$ . Further, let  $H$  be the discrete multidimensional Haar transform, and let  $A \in \mathbb{R}^{m \times n}$  such that  $AH^{-1}$  satisfies  $\text{RIP}_{\delta, 5k}$  with  $\delta < \frac{1}{3}$ . Then for any  $\bar{u} \in \mathbb{R}^n$  with  $b = A\bar{u} + \nu$  and  $\|\nu\|_2 \leq \varepsilon$ , the solution  $u$  of (3.9) satisfies the gradient error bound*

$$\|\nabla u - \nabla \bar{u}\|_1 \leq \|\nabla \bar{u} - (\nabla \bar{u})_k\|_1 + \sqrt{k}\varepsilon,$$

and the signal error bound

$$\|u - \bar{u}\|_2 \leq \log\left(\frac{n}{k}\right) \frac{\|\nabla \bar{u} - (\nabla \bar{u})_k\|_1}{\sqrt{k}} + \varepsilon.$$

Note that recovery is exact when  $\nabla \bar{u}$  is exactly  $k$ -sparse and  $\|v\|_2 = 0$ .

The RIP assumption on  $AH^{-1} = AH^\top$  implies that  $\mathcal{N}(A)$  cannot contain any signals admitting a  $k$ -sparse wavelet expansion, apart from the zero vector, since  $\|Av\|_2 = \|AH^{-1}Hv\|_2 \approx (1 \pm \delta)\|Hv\|_2 = (1 \pm \delta)\|v\|_2$ , with the last equality holding because  $H^\top H = I$ .

There exist sensing matrices  $A \in \mathbb{R}^{m \times n}$  which satisfy the above conditions, e.g.  $RIP_{1/3,k}$ , where  $k$  can be as large as  $O(m/\log(m/n))$ . This class includes matrices with i.i.d. standard Gaussian or  $\pm 1$  entries, random submatrices of the Fourier transform and other orthogonal matrices.

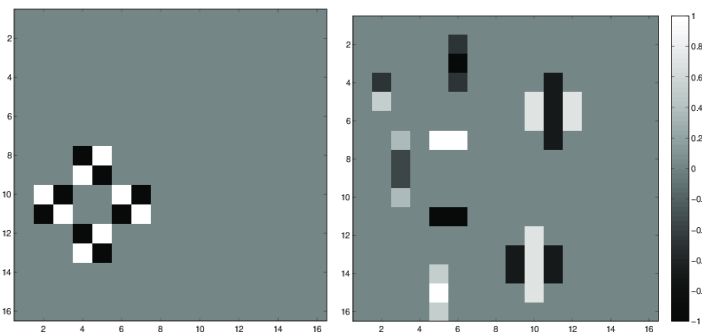


Figure 3.5: The *sparsest* nullspace vector  $u_{\mathcal{N}} \in \mathcal{N}(A) \setminus \{0\}$  is shown on the left as a  $16 \times 16$  image, for matrices  $A$  from Section 3.1.1 with 6,7 or 8 projecting directions, where  $d = 16$ , compare Table 3.1. Gray indicates components with value 0, white the value 1 and black the value  $-1$ . Projections along all rays depicted in Fig. 3.2 sum up to zero. This shows that  $\text{spark}(A) = 16$  and the matrix has a NSP of order 7. These numbers do not change with the problem's size for any  $d \geq 16$ . The image on the right depicts the bivariate Haar-transformed nullspace basis vector  $Hu_{\mathcal{N}}$ , which has 32 nonzero elements.

In our scenario, however, due to the low RIP order of the tomographic projection matrix  $A$ , for any image dimension  $d$ , the RIP order of  $AH^{-1}$  does not improve significantly. To illustrate this point, let us consider further the bivariate discrete Haar transform  $H$  and a sparse nullspace vector  $u_{\mathcal{N}}$  with  $\|u_{\mathcal{N}}\|_0 = 16$ , depicted in Fig. 3.5, left panel, of the 2D projection matrix  $A$  from 6, 7 or 8 projections. Then  $0 = \|Au_{\mathcal{N}}\|_2 = \|AH^{-1}Hu_{\mathcal{N}}\|_2$  holds with  $\|Hu_{\mathcal{N}}\|_0 = 32$ , see Fig. 3.5, right. Thus, the matrix  $AH^{-1}$  cannot satisfy RIP of an order larger than  $32 - 1$ , and this holds for any  $d \geq 16$ . Consequently, suppose it does accordingly satisfy  $RIP_{1/3,31}$ , then Thm. 3.2.1 would imply exact recovery of any image with a 6-sparse image gradient. Unfortunately, such an extremely low sparsity is of limited use for practical applications.

### 3.3 Cosparsity and TV-Based Reconstruction

In this section we derive bounds for the number  $m$  of measurements, depending on the cosparsity of the vector  $u$ , that should be reconstructed, with respect to the analysis operator  $B$ . This requires to estimate the dimension of the subspace of  $\ell$ -cosparse vectors. We relate this problem to the isoperimetric problem on grid graphs studied by [10]. In this more general way, we reproduce the estimate proved differently in [87] for the 2D case and additionally provide an estimate for the 3D case. For comparison and completion, we mention the uniqueness results from [82, 87].

#### 3.3.1 Basic Uniqueness Results

This section collects some results from [87] that were derived based on [82].

**Proposition 3.3.1** (Uniqueness with known cosupport). *Let  $A \in \mathbb{R}^{m \times n}$  and  $B \in \mathbb{R}^{p \times n}$  be given measurement and analysis operators and assume the rows of the matrix  $\begin{pmatrix} A \\ B \end{pmatrix}$  are linearly independent. Then, if the cosupport  $\Lambda \subset [p]$  of the  $\ell$ -cosparse vector  $u \in \mathbb{R}^n$  is known, the condition*

$$\max_{|\Lambda| \geq \ell} \dim \mathcal{W}_\Lambda \leq m \quad (3.10)$$

*is necessary and sufficient for recovery of every such vector from the measurements  $b = Au$ .*

We remind the reader that the quantity  $\mathcal{W}_\Lambda$  stands for the subspace of  $\ell$ -cosparse signals:

$$\bigcup_{\Lambda \subset [p]: |\Lambda| = \ell} \mathcal{W}_\Lambda,$$

where  $\mathcal{W}_\Lambda = \text{span}(\omega_j, j \in \Lambda)^\perp$ , with  $\omega_j$  being the rows of the matrix  $\Omega$ .

Proposition 3.3.1 says that if the dimension of the subspace  $\mathcal{W}_\Lambda$  increases, then more measurements are needed for recovery of  $\ell$ -cosparse vectors  $u \in \mathcal{W}_\Lambda$ . The dimension  $\dim \mathcal{W}_\Lambda$  increases for decreasing  $\ell$ .

**Proposition 3.3.2** (Uniqueness with unknown cosupport). *Let  $A \in \mathbb{R}^{m \times n}$  and  $B \in \mathbb{R}^{p \times n}$  be given measurement and analysis operators, and assume the rows of the matrix  $\begin{pmatrix} A \\ B \end{pmatrix}$  are linearly independent. Then a necessary condition for uniqueness of a  $\ell$ -cosparse solution  $u$  to the measurement equations  $Au = b$  is*

$$\tilde{\kappa}_B(\ell) \leq m, \quad \tilde{\kappa}_B(\ell) := \max \{ \dim(\mathcal{W}_{\Lambda_1} + \mathcal{W}_{\Lambda_2}) : |\Lambda_i| \geq \ell, i = 1, 2 \}, \quad (3.11)$$

*whereas a sufficient such condition is*

$$\max_{|\Lambda| \geq \ell} \dim \mathcal{W}_\Lambda \leq \frac{m}{2}, \quad (3.12)$$

Roughly speaking, lack of knowledge of  $\Lambda$  implies the need of twice the number of measurements for unique recovery.

**Remark 3.3.1.** Both propositions assume the rows of  $A$  and  $B$  are independent. This is neither the case for typical sensor matrices  $A$  used in discrete tomography nor in the specific case  $B = \nabla$  considered next.

Denoting  $\kappa_B(\ell) := \max_{|\Lambda| \geq \ell} \dim \mathcal{W}_\Lambda$ , we will show in our experiments, that the estimates of  $\kappa_B(\ell) = \kappa_\nabla(\ell)$  derived in Sect. 3.3.2 correctly display the relationship between the basic parameters involved, up to some scale factor discussed in Sect. 3.5.

### 3.3.2 Application to the Analysis Operator $\nabla$

In order to apply the results of Sect. 3.3.1, the function  $\kappa_B(\ell)$  has to be evaluated, or estimated, in the case  $B = \nabla$ .

For a given cosupport  $\Lambda \subset E$ , define the set of vertices covered by  $\Lambda$ ,

$$V(\Lambda) = \{v \in V : v \in e \text{ for some } e \in \Lambda\}, \quad (3.13)$$

and denote the number of connected components of  $V(\Lambda)$  by  $|V(\Lambda)|_\sim$ . Due to definition (3.3) of the analysis operator  $\nabla$  and (2.26), each component  $(\nabla_\Lambda u)_i$  corresponds to an edge  $e = (v_1, v_2)$  with  $u(v_1) = u(v_2)$ . Therefore, following the reasoning in [87],  $u \in \mathcal{W}_\Lambda = \mathcal{N}(\nabla_\Lambda)$  if and only if  $u$  is constant on each connected component of  $V(\Lambda)$ . Hence  $\dim \mathcal{W}_\Lambda$  equals the size of the remaining vertices  $|V \setminus V(\Lambda)|$  plus the degree of freedom for each connected component,

$$\dim \mathcal{W}_\Lambda = |V| - |V(\Lambda)| + |V(\Lambda)|_\sim. \quad (3.14)$$

Now, in view of  $\kappa_B(\ell) := \max_{|\Lambda| \geq \ell} \dim \mathcal{W}_\Lambda$ , consider some  $\Lambda$  with  $|\Lambda| = \ell$  and the problem

$$\max_{\Lambda: |\Lambda| = \ell} \dim \mathcal{W}_\Lambda = |V| - \min_{\Lambda: |\Lambda| = \ell} (|V(\Lambda)| - |V(\Lambda)|_\sim). \quad (3.15)$$

Clearly, the minimal value of the last term is  $|V(\Lambda)|_\sim = 1$ . It will turn out below that this value is attained for extremal sets  $\Lambda$  and that the maximum in  $\kappa_B(\ell)$  is achieved for  $|\Lambda| = \ell$ .

We therefore temporarily ignore the last term and focus on the second term. The problem is to *minimize* over all subsets  $\Lambda \subset E$  of cardinality  $|\Lambda| = \ell$  the number  $|V(\Lambda)|$  of vertices covered by  $\Lambda$ . We establish this relationship by considering instead the problem of *maximizing* the set  $\Lambda$  over all sets  $S := V(\Lambda) \subseteq V$  of fixed cardinality  $s = |S(\Lambda)|$ . This problem was studied in [10] for regular grid graphs  $G = (V, E)$  with vertex set  $V = [q]_0^d$  with equal dimension along each coordinate, in terms of the problem

$$\max_{S: |S| = s} |\text{Int}_e(S)|, \quad (3.16)$$

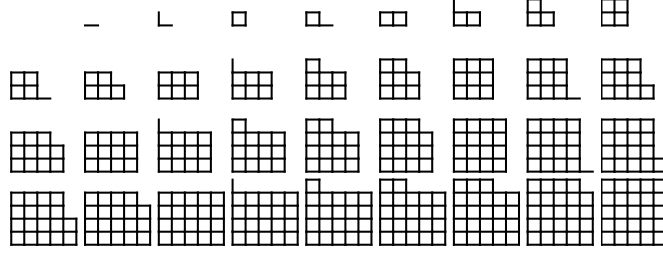


Figure 3.6: From left to right, top to bottom: Edge sets  $\Lambda$  corresponding to the subsets  $S = V(\Lambda) \subseteq V = [q]_0^d$ ,  $q = 5$ ,  $d = 2$ , of cube-ordered vertices of cardinalities  $s = |S| = 1, 2, \dots, |V|$ . According to Thm. 3.3.4, these sets belong to the maximizers of  $|\Lambda|$  among all subsets  $V(\Lambda) \subseteq V$  with fixed  $s = |V(\Lambda)|$ .

where  $\text{Int}_e(S)$  denotes the *edge interior* of a set  $S \subset V(G)$ ,

$$\text{Int}_e(S) := \{(v_1, v_2) \in E : v_1, v_2 \in S\}, \quad (3.17)$$

which equals  $\text{Int}_e(S) = \Lambda$  for our definition  $S = V(\Lambda)$ .

**Theorem 3.3.3** ([10, Thm. 13]). *Let  $S$  be a subset of  $[q]_0^d$ , with  $s = |S|$ ,  $q \geq 3$ ,  $d \geq 2$ . Then*

$$|\text{Int}_e(S)| \leq \max \left\{ ds(1 - s^{-1/d}), dq^d(1 - 1/q)(1 - (1 - s/q^d)^{1-1/d}) \right\}. \quad (3.18)$$

Some sets  $S = V(\Lambda) \subseteq V$  corresponding to maximal sets  $\Lambda = \text{Int}_e(S)$  are also determined in [10]. The following corresponding assertion is based on the *cube order* or vertices  $v \in V = [q]_0^d$  (identified with grid vectors  $v = (v_1, \dots, v_d)^\top$ ):  $v \prec v' \Leftrightarrow w(v) < w(v')$ , where  $w(v) = \sum_{i \in [d]} 2^{i+dv_i}$ . See Figure 3.6 for an illustration.

**Theorem 3.3.4** ([10, Thm. 15]). *Let  $S' \subset V = [q]^d$ , and let  $S$  be the set of the first  $s = |S'|$  vertices in the cube order on  $V$ . Then  $|\text{Int}_e(S')| \leq |\text{Int}_e(S)|$ .*

Thm. 3.3.4 says (cf. Fig. 3.6) that singly connected minimal sets  $V(\Lambda)$  in (3.15) are achieved, that is  $|V(\Lambda)|_{\sim} = 1$ . Furthermore, these sets  $\{\Lambda\}_{|\Lambda| \geq \ell}$  are nested. Hence the maximum in  $\kappa_B(\ell)$  is achieved for  $|\Lambda| = \ell$ .

A closer inspection of the two terms defining the upper bound (3.18) shows that the first term of the r.h.s. is larger if  $s \geq d^d = 4$  in the 2D case  $d = 2$ , respectively, if  $s \geq d^d = 27$  in the 3D case  $d = 3$ . The corresponding values of the bound are  $|\text{Int}_e(S)| \leq 4$  and  $|\text{Int}_e(S)| \leq 54$ , respectively. As a consequence, we

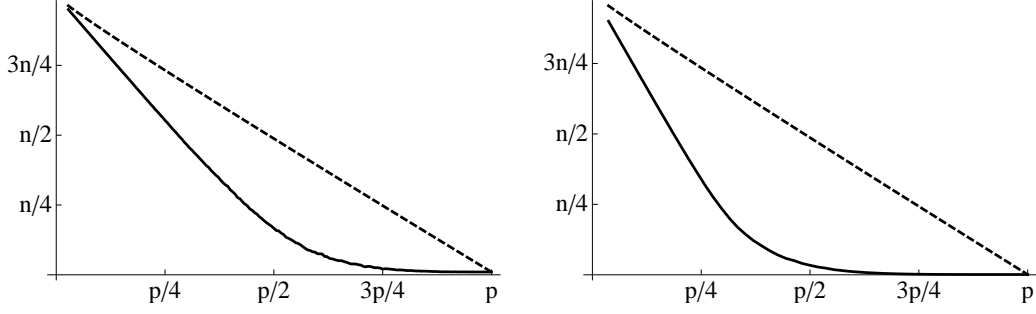


Figure 3.7: The bounds (3.20a) and (3.20b) shown in the left and right panel respectively, as dashed lines, for  $d = 10$ , as a function of  $\ell$ . The solid lines show empirical expected values of  $\kappa_{\nabla}(\ell)$  computed by averaging over 100 analysis matrices  $B_{\Lambda}$  for each value  $\ell = |\Lambda|$ . The gap to the upper bound simply shows that the extremal sets discussed in connection with Theorem 3.3.4 are not observed in random experiments. For example, it is quite unlikely that random cosupports  $\Lambda$  are singly connected.

consider the practically relevant first term. Setting  $\ell = |\text{Int}_e(S)| = |V(\Lambda)|$  and solving the equality for  $s$  (due to Thm. 3.3.4) yields

$$s = \frac{1}{2}(1 + \ell + \sqrt{1 + 2\ell}) \quad (d = 2) \quad (3.19a)$$

$$s = \frac{1}{3} \left( 2^{1/3} \frac{1 + 2\ell}{t(\ell)} + \left( 1 + \ell + \frac{1}{2^{1/3}} t(\ell) \right) \right) \quad (d = 3) \quad (3.19b)$$

$$t(\ell) = \left( 2 + 6\ell + 3\ell^2 + \sqrt{(4 + 9\ell)\ell^3} \right)^{1/3} \quad (3.19c)$$

$$\geq \frac{1}{3} \left( 1 + \ell + (3\ell^2)^{1/3} + 2(\ell/3)^{1/3} \right) + O(\ell^{-1/3}). \quad (3.19d)$$

Inserting  $s$ , or simpler terms lower bounding  $s$ , for  $|V(\Lambda)|$  in (3.15) and putting all conclusions together, yields for  $\kappa_B(\ell)$  and  $B = \nabla$ :

**Lemma 3.3.5.** *Let  $G = (V, E)$  be a regular grid graph with  $V = [q]_0^d$ ,  $n = |V| = q^3$ . Then*

$$\forall \ell > 4, \quad \kappa_{\nabla}(\ell) \leq n - \frac{1}{2}(\ell + \sqrt{1 + 2\ell}) + \frac{1}{2}, \quad (d = 2), \quad (3.20a)$$

$$\forall \ell > 54, \quad \kappa_{\nabla}(\ell) \leq n - \frac{1}{3} \left( \ell + \sqrt[3]{3\ell^2} + 2\sqrt[3]{\frac{\ell}{3}} \right) + \frac{2}{3}, \quad (d = 3). \quad (3.20b)$$

Figure 3.7 illustrates these bounds.

**Remark 3.3.2.** Up to the constant 1 under the square root, the bound (3.20a) for the 2D case equals the bound derived in a different way in [87]. We provided

the bounds (3.20) based on general results in [10] that apply to grid graphs in any dimension  $d \geq 2$ .

We conclude this section by applying Propositions 3.3.1 and 3.3.2.

**Corollary 3.3.6.** *Under the assumptions of Propositions 3.3.1 and 3.3.2, a  $\ell$ -cosparse solution  $u$  to the measurement equations  $Au = b$  will be unique if the number of measurements satisfies*

$$m \geq n - \frac{1}{2}(\ell + \sqrt{2\ell + 1} - 1) \quad (d = 2), \quad (3.21a)$$

$$m \geq n - \frac{1}{3}(\ell + \sqrt[3]{3\ell^2} + 2\sqrt[3]{\frac{\ell}{3}} - 2) \quad (d = 3) \quad (3.21b)$$

in case the cosupport  $\Lambda$  is known, and

$$m \geq 2n - (\ell + \sqrt{2\ell + 1} - 1) \quad (d = 2), \quad (3.22a)$$

$$m \geq 2n - \frac{2}{3}(\ell + \sqrt[3]{3\ell^2} + 2\sqrt[3]{\frac{\ell}{3}} - 2) \quad (d = 3) \quad (3.22b)$$

in case the cosupport  $\Lambda$  is unknown.

The above derived bounds on the required image cosparsity guarantees uniqueness in case of known or unknown cosupport, and imply that recovery can be carried out via

$$\min_u \|Bu\|_0 \quad \text{s.t.} \quad Au = b, B_\Lambda u = 0, \quad (3.23)$$

when the cosupport is known, or via

$$\min_u \|Bu\|_0 \quad \text{s.t.} \quad Au = b, \quad (3.24)$$

when the cosupport is unknown. In Sect. 3.5, we compare these relationships to numerical results involving convex relaxations of (3.23) and (3.24), studied in Sect. 3.4.

## 3.4 Recovery by Linear Programming

In this section, uniqueness of the optimum  $\bar{u}$  solving problem (3.7) is studied. The resulting condition is necessary and sufficient for unique recovery  $\bar{u} = u^*$  of any  $\ell$ -cosparse vector  $u^*$  that satisfies  $Au^* = b$  and has cosupport  $\Lambda$ ,  $|\Lambda| = \ell$ , with respect to the analysis operator  $B = \nabla$ .

We turn problem (3.7) into a standard linear programming formulation. Defining

$$M := \begin{pmatrix} B & -I & I \\ A & 0 & 0 \end{pmatrix}, \quad q := \begin{pmatrix} 0 \\ b \end{pmatrix} \quad (3.25)$$

and the polyhedral set

$$\mathcal{P} := \{w \in \mathbb{R}^{n+2p} : Mw = q, w \geq 0\}, \quad w := \begin{pmatrix} u \\ v \end{pmatrix} = \begin{pmatrix} u \\ v^1 \\ v^2 \end{pmatrix}, \quad (3.26)$$

problem (3.7) equals the linear program (LP)

$$\min_{w \in \mathcal{P}} \langle c, w \rangle = \min_{(u, v^1, v^2) \in \mathcal{P}} \langle \mathbb{1}, v^1 + v^2 \rangle, \quad c = \begin{pmatrix} 0 \\ \mathbb{1} \\ \mathbb{1} \end{pmatrix}. \quad (3.27)$$

Let  $\bar{w} = (\bar{u}, \bar{v}) = (\bar{u}, \bar{v}^1, \bar{v}^2)$  solve (3.27). We assume throughout

$$\bar{u}_i > 0, \quad i \in [n] \quad (3.28)$$

which is not restrictive with respect to applications ( $u$  may e.g. represent strictly positive material densities). Based on  $\bar{w}$ , we define the corresponding index sets

$$J := \{i \in [\dim(w)] : \bar{v}_i = 0\}, \quad \bar{J} := \{i \in [\dim(v)] : \bar{v}_i = 0\}, \quad w_J = v_{\bar{J}}, \quad \forall w = \begin{pmatrix} u \\ v \end{pmatrix}. \quad (3.29)$$

**Theorem 3.4.1** ([84, Thm. 2(iii)]). *Let  $\bar{w}$  be a solution of the linear program (3.27). The following statements are equivalent:*

- (i)  $\bar{w}$  is unique.
- (ii) There exists no  $w$  satisfying

$$Mw = 0, \quad w_J \geq 0, \quad \langle c, w \rangle \leq 0, \quad w \neq 0. \quad (3.30)$$

We turn Theorem (3.4.1) into a *nullspace condition* w.r.t. the sensor matrix  $A$ , for the unique solvability of problems (3.27) and (3.7). This condition is stated as Corollary 3.4.3 below, after a preparatory Lemma.

**Lemma 3.4.2.** *Let  $\bar{w}$  be a solution of the LP (3.27). Then the cardinality of the index set  $\bar{J}$  defined by (3.29) is*

$$|\bar{J}| = 2\ell + k = p + \ell, \quad |\bar{J}^c| = 2p - |\bar{J}| = k, \quad k := p - \ell. \quad (3.31)$$

*Proof.* The minimal objective function value (3.27) is  $\sum_{i \in [p]} \bar{v}_i^1 + \bar{v}_i^2$  with all summands being non-negative. Since  $B\bar{u} = \bar{v}^1 - \bar{v}^2$ ,  $(B\bar{u})_\Lambda = 0$  and optimality of  $\bar{v}$  imply  $\bar{v}_\Lambda^1 = \bar{v}_\Lambda^2 = 0$ , which contributes  $2|\Lambda| = 2\ell$  indices to  $\bar{J}$ . Furthermore, if  $(B\bar{u})_i = \bar{v}_i^1 - \bar{v}_i^2 < 0$ , then optimality of  $\bar{v}$  implies  $\bar{v}_i^1 = 0$ ,  $\bar{v}_i^2 > 0$  and vice versa if  $(B\bar{u})_i > 0$ . Hence  $\Lambda^c$  supports  $|\Lambda^c| = p - \ell = k$  vanishing components of  $\bar{v}$ .  $\square$

**Corollary 3.4.3.** *Let  $\bar{w} = (\bar{u}, \bar{v}^1, \bar{v}^2)$  be a solution of the linear program (3.27) with corresponding index sets  $J, \bar{J}$  given by (3.29), and with component  $\bar{u}$  that solves problem (3.7) and has cosupport  $\Lambda$  with respect to  $B$ . Then  $\bar{w}$  resp.  $\bar{u}$  are unique if and only if*

$$\forall w = \begin{pmatrix} u \\ v \end{pmatrix}, v = \begin{pmatrix} v^1 \\ v^2 \end{pmatrix} \quad \text{s.t.} \quad u \in \mathcal{N}(A) \setminus \{0\} \quad \text{and} \quad Bu = v^1 - v^2 \quad (3.32)$$

the condition

$$\|(Bu)_\Lambda\|_1 > \langle (Bu)_{\Lambda^c}, \text{sign}(B\bar{u})_{\Lambda^c} \rangle \quad (3.33)$$

holds. Furthermore, any unknown  $\ell$ -cosparsive vector  $u^*$  with  $Au^* = b$  can be uniquely recovered as solution  $\bar{u} = u^*$  to (3.7) if and only if, for all vectors  $u$  conforming to (3.32), the condition

$$\|(Bu)_\Lambda\|_1 > \sup_{\Lambda \subset [p]: |\Lambda|=\ell} \sup_{\bar{u} \in \mathcal{W}_\Lambda} \langle (Bu)_{\Lambda^c}, \text{sign}(B\bar{u})_{\Lambda^c} \rangle \quad (3.34)$$

holds.

**Remark 3.4.1.** Condition (3.33) corresponds up to a magnitude  $|\cdot|$  operation applied to the right-hand side to the statement of [87, Thm. 7]. The authors do not present an explicit proof, but mention in [87, App. A] that the result follows by combining a strictly local minimum condition with convexity of the optimization problem for recovery.

Our subsequent explicit proof elaborates basic LP-theory due to [84] and Thm. 3.4.1.

*Proof of Corollary 3.4.3.* Theorem (3.4.1) asserts that  $\bar{w}$  is unique if and only if for every  $w \in \mathcal{N}(M) \setminus \{0\}$  with  $w_J \geq 0$  the condition  $\langle c, w \rangle > 0$  holds. In view of the definition (3.25) of  $M$ , vectors  $w \in \mathcal{N}(M) \setminus \{0\}$  are determined by (3.32). Condition (3.32) excludes vectors  $0 \neq w = (0, v^1, v^2) \in \mathcal{N}(M)$  because then  $v^1 = v^2$  and  $w_J \geq 0$  implies exclusion of those  $w$  by  $\langle c, w \rangle \leq 0$  in (3.30).

It remains to turn the condition (3.30) into a condition for vectors  $u$  given by vectors  $w = (u, v^1, v^2)$  satisfying (3.32). To this end, we focus on such vectors  $w$  with  $w_J \geq 0$  that minimize  $\langle c, w \rangle$ . We have  $w_J = v_{\bar{J}}$  by (3.29), and the proof of Lemma 3.4.2 shows that  $v_{\bar{J}} \geq 0$  decomposes into

- $2\ell$  conditions  $v_\Lambda^1, v_\Lambda^2 \geq 0$  leading to the choice

$$\begin{cases} v_i^1 = (Bu)_i \geq 0, & v_i^2 = 0, & \text{if } (Bu)_i \geq 0, \\ v_i^1 = 0, & v_i^2 = -(Bu)_i \geq 0, & \text{if } (Bu)_i \leq 0, \end{cases} \quad i \in \Lambda \quad (3.35)$$

minimizing  $\langle c, w \rangle$ ;

- $k$  conditions supported by  $\Lambda^c$  of the form: either  $v_i^1 \geq 0$  or  $v_i^2 \geq 0$  depending on  $(B\bar{u})_i > 0$  or  $(B\bar{u})_i < 0$ ,  $i \in \Lambda^c$ . In order to minimize  $\langle c, w \rangle$ , this leads to the choice

$$\begin{cases} v_i^1 = 0, & v_i^2 = -(Bu)_i \leq 0, & \text{if } (Bu)_i \geq 0, (B\bar{u})_i > 0, \\ v_i^1 = 0, & v_i^2 = (Bu)_i \geq 0, & \text{if } (Bu)_i \leq 0, (B\bar{u})_i > 0, \\ v_i^1 = (Bu)_i \geq 0, & v_i^2 = 0, & \text{if } (Bu)_i \geq 0, (B\bar{u})_i < 0, \\ v_i^1 = (Bu)_i \leq 0, & v_i^2 = 0, & \text{if } (Bu)_i \leq 0, (B\bar{u})_i < 0, \end{cases} \quad i \in \Lambda^c. \quad (3.36)$$

By (3.27),  $\langle c, w \rangle = \langle \mathbb{1}, v^1 + v^2 \rangle = \langle \mathbb{1}, (v^1 + v^2)_\Lambda \rangle + \langle \mathbb{1}, (v^1 + v^2)_{\Lambda^c} \rangle$ , and (3.35) shows that  $\langle \mathbb{1}, (v^1 + v^2)_\Lambda \rangle = \|(Bu)_\Lambda\|_1$  whereas (3.36) shows that  $\langle \mathbb{1}, (v^1 + v^2)_{\Lambda^c} \rangle = \langle (Bu)_{\Lambda^c}, -\text{sign}(B\bar{u})_{\Lambda^c} \rangle$ . Thus  $\langle c, w \rangle \leq 0 \Leftrightarrow \|(Bu)_\Lambda\|_1 - \langle (Bu)_{\Lambda^c}, \text{sign}(B\bar{u})_{\Lambda^c} \rangle \leq 0$ , and non-existence of such  $w$  means  $\langle c, w \rangle > 0$  for every such  $w$ , which equals (3.32) and (3.33).

Finally, generalizing condition (3.33) to all vectors  $u^* \in \mathcal{W}_\Lambda$  and all possible cosupports  $\Lambda$  leads to (3.34).  $\square$

Conditions (3.33) and (3.34) clearly indicate the direct influence of cosparsity on the recovery performance: If  $\ell = |\Lambda|$  increases, then these conditions will more likely hold.

On the other hand, these results are mainly theoretical since numerically checking (3.34) is infeasible. This motivates the comprehensive experimental assessment of recovery properties reported in Sect. 3.5.

## 3.5 Numerical Experiments

In this section, we relate the previously derived bounds on the required image cosparsity that guarantees uniqueness in case of known or unknown cosupport  $\Lambda$  to numerical experiments.

### 3.5.1 Set-Up

This section describes how we generate 2D or 3D images for a given cosparsity  $\ell$  and how we acquire measurements.

#### Test Images

Recall from Sect. 2.1.2.2, that the sparsity of the image gradient is denoted by  $k$  and the cosparsity by  $\ell$ ,

$$k = \|Bu\|_0 = |\text{supp}(Bu)|, \quad B \in \mathbb{R}^{p \times n}, \quad (3.37a)$$

$$\ell = p - \|Bu\|_0 = p - k, \quad (3.37b)$$

$\Lambda := \{r \in [p] : (Bu)_r = 0\}$  denotes the cosupport of the input image  $u$  with respect to the analysis operator  $B$ , and  $\Lambda^c = [p] \setminus \Lambda$  denotes the complement of the set  $\Lambda$ .

Using the parametrization

$$\rho := \frac{k}{n} \quad (3.38)$$

with

$$k := p - \ell \quad \text{and} \quad n = \begin{cases} d^2 & \text{in 2D} \\ d^3 & \text{in 3D} \end{cases}, \quad p = \begin{cases} 2d(d-1) & \text{in 2D} \\ 3d^2(d-1) & \text{in 3D} \end{cases}, \quad (3.39)$$

we generated random 2D and 3D images composed of randomly located ellipsoids with random radii along the coordinate axes. Fig. 3.8 and 3.9 depict a small sample of these images for illustration and provide the parameter ranges.

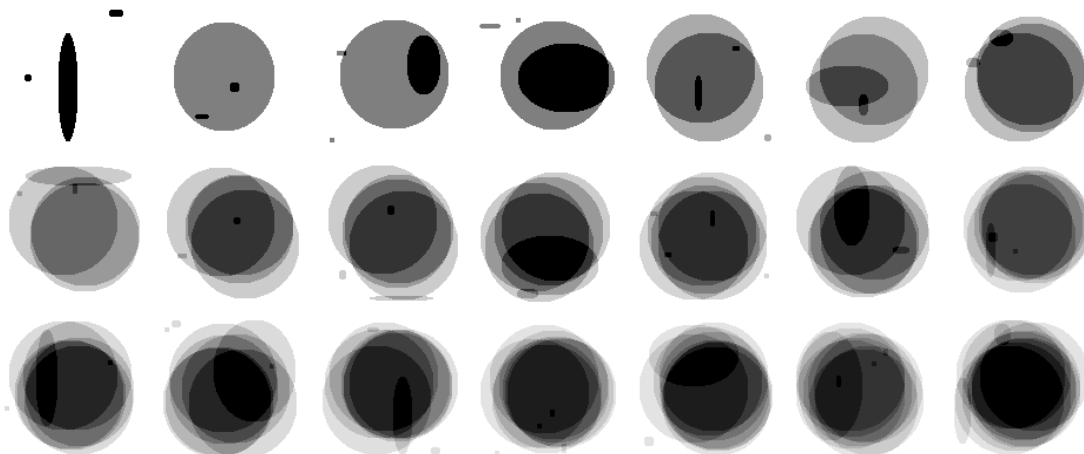


Figure 3.8: Random images with varying cosparsity  $\ell = p - k$ , parametrized by  $\rho$  (3.38). For each dimension  $d = 80 \cdots 180$ , random images were generated for  $\rho = 0.005 \cdots 0.22$ . The figure shows a sample image for a subset of increasing values of  $\rho$  and  $d = 120$ .

### Tomographic Projections

Images in 2D are undersampled by the projection matrices from Sect. 3.1.1, with parameters listed in Table 3.1. In 3D we consider the two projection matrices from Sect. 3.1.1, see Fig. 3.3 and Fig. 3.4. We also consider a perturbation of each  $A$ . Each perturbed matrix  $\tilde{A}$  has the same sparsity structure as  $A$ , but random entries drawn from the standard uniform distribution on the open interval  $(0.9, 1.1)$ .

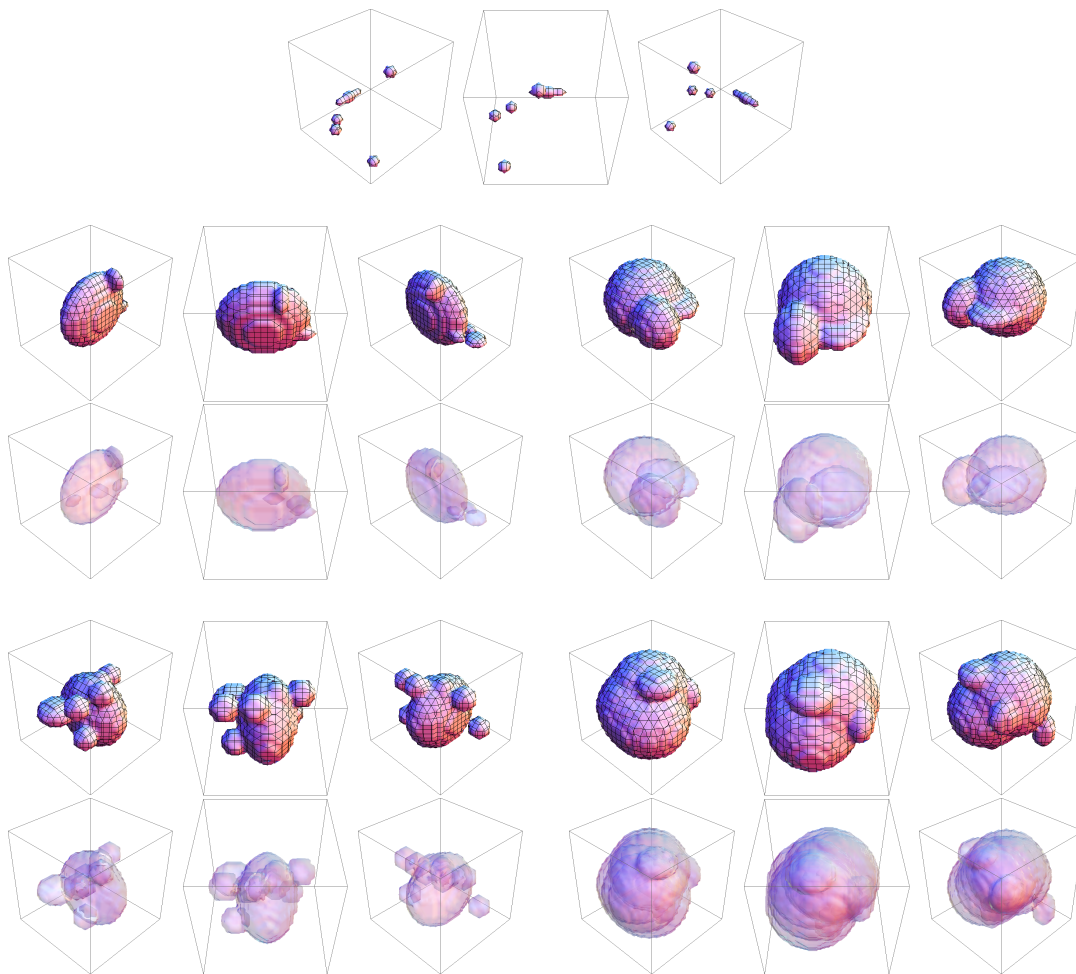


Figure 3.9: Random images with varying sparsity  $\ell = p - k$ , parametrized by  $\rho$  (3.38). For dimension  $d = 31$ , random images were generated for  $\rho = 0.0032 \cdots 1.01$ . The figure shows a sample image for five different values of  $\rho$ , each plotted from three different viewpoints.

### 3.5.2 Optimization

To recover a  $\ell$ -sparse test image  $\bar{u}$ , we solve the LP relaxation (3.27) of (3.24), where we take into account the nonnegativity of  $\bar{u}$ . The relaxation is obtained from (3.7) by considering two additional variables  $v^1$  and  $v^2$  which represent the positive and negative part of  $Bu$ . In cases where we assume that  $\Lambda$  is known, we add the constraint  $B_\Lambda u = 0$  and solve the LP with the same objective as (3.27), but with the polyhedral feasible set defined by

$$M := \begin{pmatrix} B_{\Lambda^c} & -I_{\Lambda^c} & I_{\Lambda^c} \\ B_\Lambda & 0 & 0 \\ A & 0 & 0 \end{pmatrix} \quad \text{and} \quad q := \begin{pmatrix} 0 \\ 0 \\ b \end{pmatrix}. \quad (3.40)$$

The resulting LPs were solved with the help of a standard LP solver <sup>1</sup>. The reconstruction is considered *successful* if the solution  $u$  of the above described LPs is within a small distance from the original  $\ell$ -cosparsely  $\bar{u}$  generating the data, and  $\|u - \bar{u}\|_2 \leq \varepsilon n$  holds, with  $\varepsilon = 10^{-6}$  in 2D and  $\varepsilon = 10^{-8}$  in 3D.

### 3.5.3 Phase Transitions

Phase transitions display the empirical probability of exact recovery over the space of parameters that characterize the problem (cf. [41]). Our parametrization relates to the design of the projection matrices  $A \in \mathbb{R}^{m \times n}$ . Because both  $m$  and  $n$  depend on  $d$ , we choose  $d$  as an *oversampling parameter*, analogously to the *undersampling parameter*  $\rho = \frac{m}{n}$  used in [41].

We analyze the influence of the image cosparsity, or equivalently of the image gradient sparsity, on the recovery via (3.27) or (3.40). We assess empirical bounds in relation with the theoretically required sparsity that guarantees exact recovery, described as an empirical phase transition of  $\rho$  depending on  $d$ . This *phase transition*  $\rho(d)$  indicates the necessary relative sparsity  $\rho$  to recover a  $\ell$ -cosparsely image with overwhelming probability by convex programming.

For each  $d \in \{80, 90, \dots, 170, 180\}$  and for each relative sparsity  $\rho$ , we generated 70 images for the 2D case and 50 images for the 3D case, as illustrated in Sect. 3.5.1, together with corresponding measurements. This in turn gave us  $d, n, m$  and  $k$ , defining a point  $(d, \rho) \in [0, 1]^2$ . This range was discretized into cells so as to accumulate in a  $(d, \rho)$  cell a 1 if the corresponding experiment was successful (exact recovery) and 0 otherwise. In 2D, we performed 10 or 30 such runs for each  $(d, \rho)$  pair, for unknown or known cosupport respectively. The success rate of image reconstruction is displayed by gray values: black  $\leftrightarrow$  0% recovery rate, white  $\leftrightarrow$  100% recovery rate. In 3D, we analyzed the behavior for two image sizes,  $d = 31$  and  $d = 41$ . The same reasoning as in the 2D case was applied, except that now instead of performing one test with 10 experiments, we ran 6 tests with 30 experiments each, in both cases of unknown and known cosupport. We show the mean value averaged over all 6 tests.

#### Recovery of 2D Images

The results are shown in Fig. 3.10 and Fig. 3.11. The empirical transitions agree with the analytically derived thresholds up to a scaling factor  $\alpha$ . The values of  $\alpha$  are listed in Table 3.2. The accordingly rescaled curves are shown as dotted lines in the plots.

All plots display a phase transition and thus exhibit regions where exact image reconstruction has probability equal or close to one.

---

<sup>1</sup>MOSEK <http://mosek.com/>

$\alpha$ -values in 2D						
$d$	Cosupport	Measurements	$3P$	$4P$	$5P$	$6P$
80 ... 180	Known	unperturbed	0.9120	-	-	-
		perturbed	-	-	-	-
	Unknown	unperturbed	1.0026	1.0029	1.0034	0.9970
		perturbed	1.0056	1.0051	1.0019	1.0039

Table 3.2: The scaling factors of the theoretical curves (3.21a) and (3.22a) for known and unknown cosupport respectively.

### Recovery of 3D Images

The results are shown in Fig. 3.12 and Fig. 3.13 for  $d = 31$  and  $d = 41$ , and summarized in Fig. 3.14. The empirical phase transitions differ again from the analytically derived thresholds 3.21b and 3.22b only by a scaling factor  $\alpha$ . These values are listed as Table 3.3. The rescaled curves are shown as dotted lines in the plots. Fig. 3.14 also relates the critical sparsity of the gradient to the critical sparsity estimated in [95, 96], which in turn implies exact recovery via (3.5).

$\alpha$ -values in 3D				
# proj. dir.	Cosupport	Measurements	$d = 31$	$d = 41$
3	Known	unperturbed	0.9005	0.9109
		perturbed	0.8542	0.8760
	Unknown	unperturbed	1.0818	1.0634
		perturbed	1.0262	1.0226
4	Known	unperturbed	0.9988	0.9937
		perturbed	0.8519	0.8868
	Unknown	unperturbed	1.3185	1.223
		perturbed	1.1247	1.0909

Table 3.3: The scaling factors of the theoretical curves (3.21b) and (3.22b) for known and unknown cosupport respectively.

### 3.5.4 Discussion

Several observations are in order.

- Perturbation of projection matrices brings no significant advantage in the practically relevant case of unknown co-support. The empirical transitions will remain the same for perturbed and unperturbed matrices. This is very different to the  $\ell_1$ -minimization problem (3.5), where perturbation boosts the recovery performance significantly as shown in [95].

- In the case of known co-support, when  $B_\Lambda u = 0$  is added as additional constraint, unperturbed matrices perform better. We notice that the empirical phase transition is *below* the red curve, and deduce that linear dependencies might be beneficial when the co-support is known.
- When increasing the number of projecting directions (4,5,6 or more) the differences between estimated (dashed) and theoretical (continuous line) phase transition become smaller (clearly visible for unknown co-support results). This might be due to the fact that linear dependencies between the columns (and rows) of  $A$  become “rare”, and the assumptions of Propositions 3.3.1 and 3.3.2 are more likely to be satisfied.
- In 3D the difference between empirical phase transitions for 3 and 4 projecting directions is very small, i.e. relative phase transitions are almost equal. This is different to the 2D case above. We currently do not have an explanation for this phenomenon.
- The log-log plot in Figure 3.14 shows that phase transitions in 3D exhibit a power law behavior, similar to the theoretical phase transitions for  $\ell_1$ -recovery from [95], [96]. Moreover, the plot also shows the scaling exponent of the green and red curves is higher, which results in significantly higher sparsity levels of the image gradient than image sparsity which allow exact recovery for big volumes and large  $d$ .

## 3.6 Conclusion

We studied the cosparsity model in order to theoretically investigate conditions for unique signal recovery from severely undersampled linear systems, that involve measurement matrices whose properties fall far short of the assumptions commonly made in the compressed sensing literature. Extensive numerical experiments revealed a high accuracy of the theoretical predictions, up to a scale factor caused by slight violations in practice of our mathematical assumptions. Unique recovery can be accomplished by linear programming that in principle copes with large problem sizes. The signal class covered by the cosparsity model seems broad enough to cover relevant industrial applications of non-standard tomography, like contactless quality inspection.

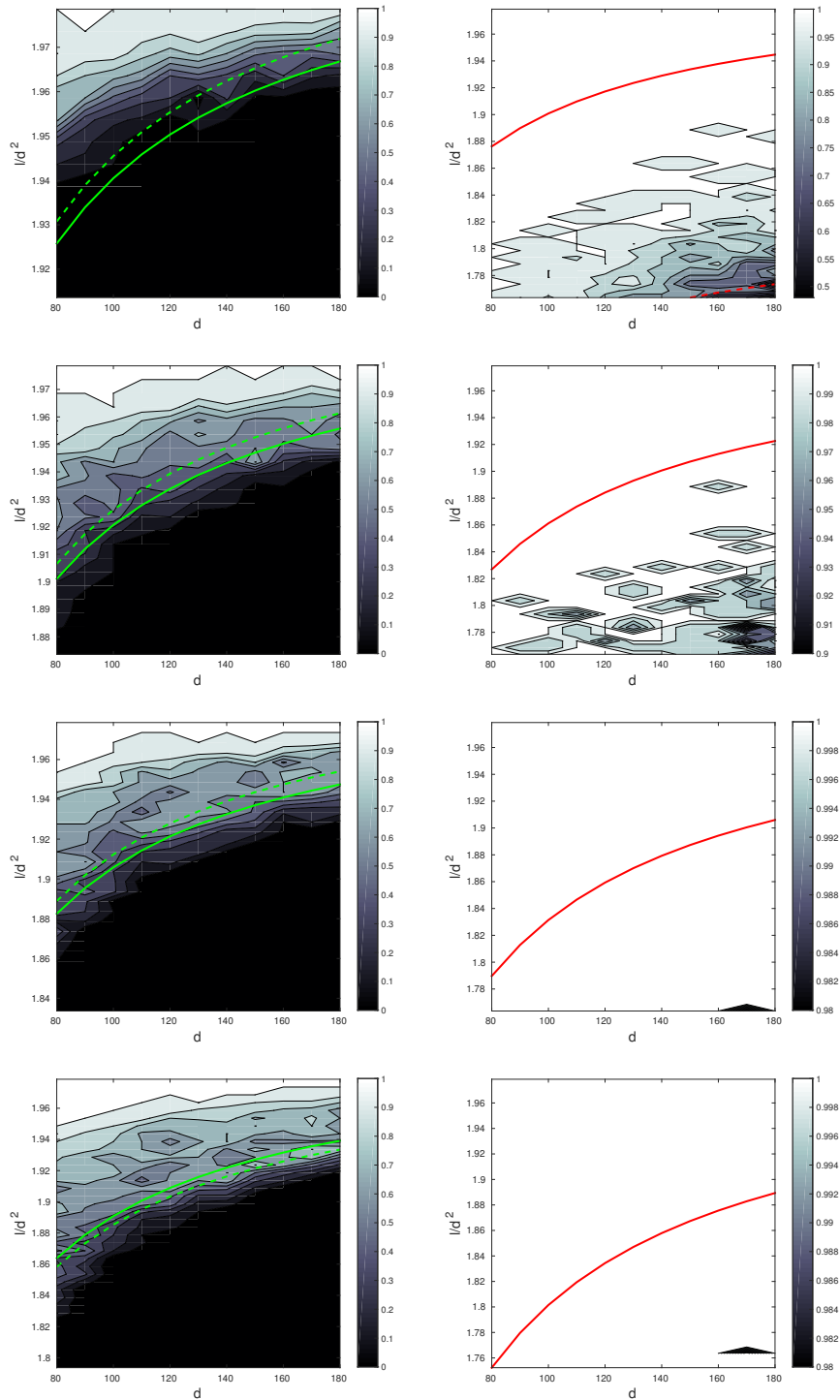


Figure 3.10: Phase transitions for the unperturbed matrix  $A$ , 2D case, 3, 4, 5 and 6 projecting directions (top to bottom), with unknown (left column) and known (right column) cosupport. The continuous green and red lines depict the theoretical curves (3.22a) and (3.21a) respectively. The dashed lines correspond to the empirical threshold, which are all scaled versions of (3.22a) (left column) or (3.21a) (right column) with scaling factors  $\alpha$  summarized in Table. 3.2.

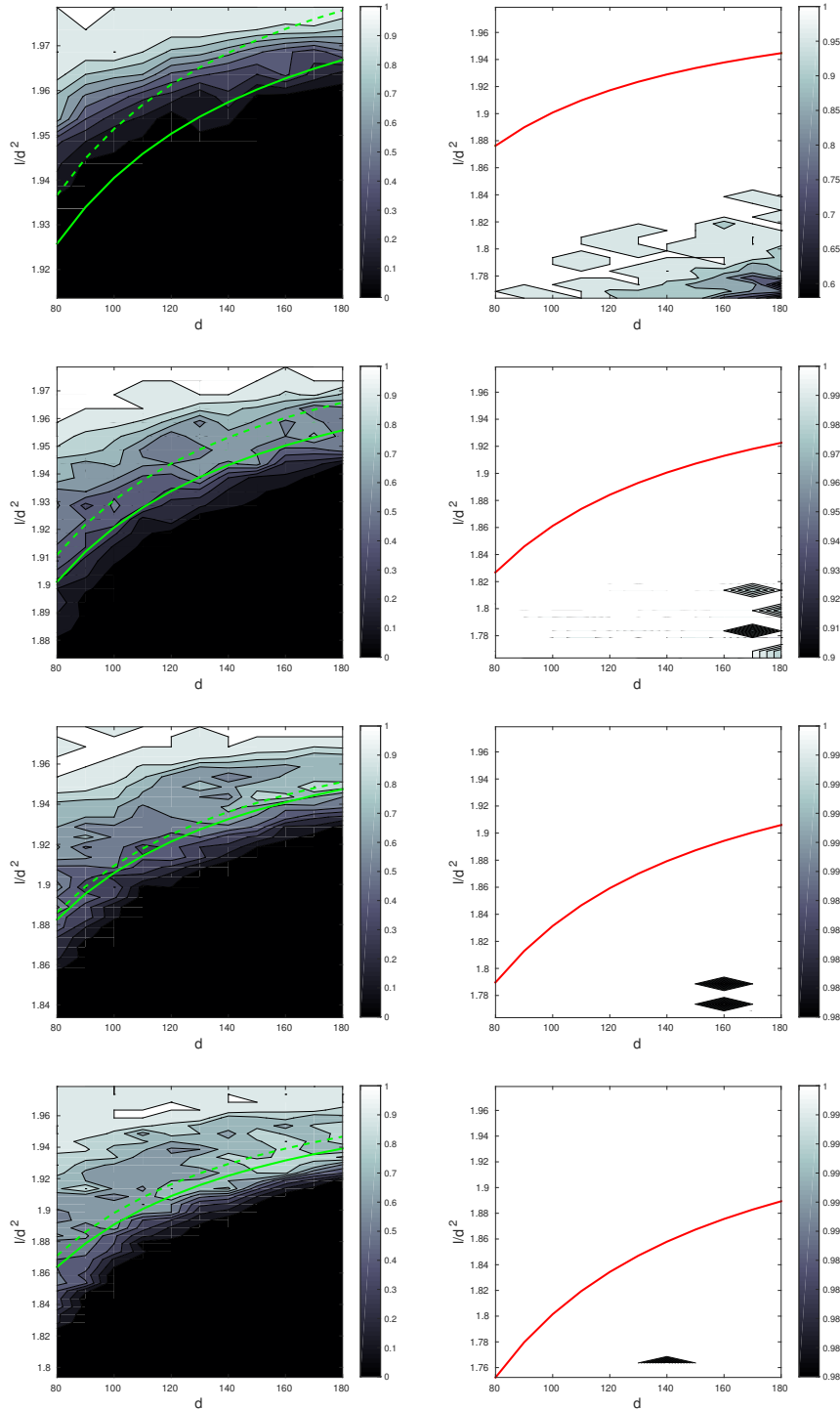


Figure 3.11: Phase transitions for the perturbed matrix  $\tilde{A}$ , 2D case, 3, 4, 5 and 6 projections (top to bottom), with unknown (left column) and known (right column) cosupport. The continuous green and red lines depict the theoretical curves (3.22a) and (3.21a) respectively. The dashed lines correspond to the empirical threshold, which are all scaled versions of (3.22a) (left column) or (3.21a) (right column) with scaling factors  $\alpha$  listed in Table. 3.21

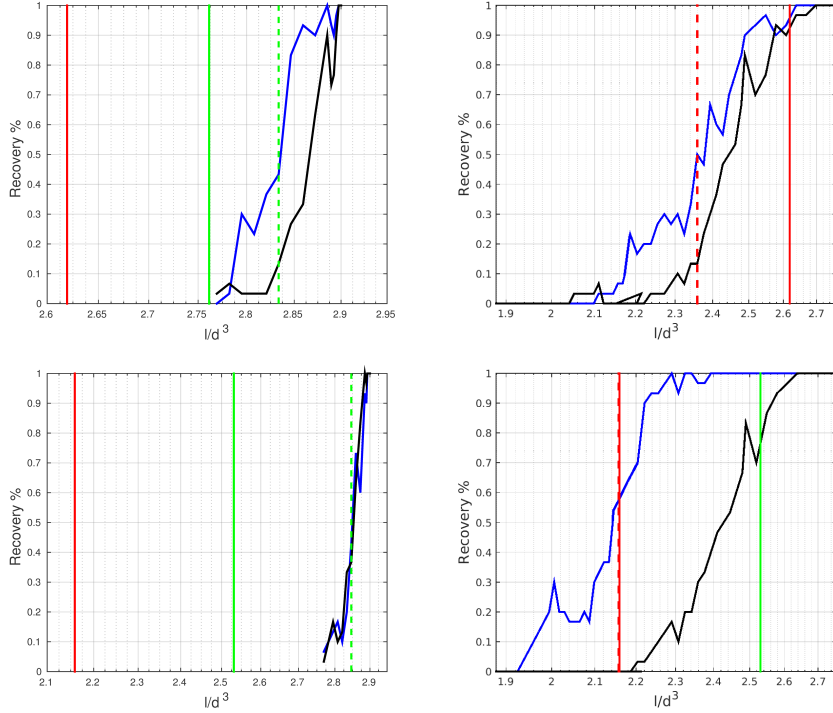


Figure 3.12: Empirical probability ( $6 \times 30$  trials) of exact recovery by total variation minimization (3.7) via the unperturbed (blue line) and perturbed (black line) matrices from Section 3.1.1, Fig. 3.3 and Fig. 3.4, for 3 (top row) and 4 (bottom row) projecting directions, respectively, and  $d = 31$ . The left column shows the decay of the recovery probability when the cosupport is *unknown* using both perturbed and unperturbed projecting matrices, while the right one, shows results for *known* cosupport. The continuous vertical lines stand for the theoretical thresholds for known (3.21b) (red) and unknown (3.22b) (green) cosupport, while the dotted red and green vertical lines stand for the empirically estimated threshold for known and unknown cosupport but for unperturbed matrices only. The deviation of the empirical thresholds from the theoretical curves for known cosupport (3.21b) and unknown cosupport (3.22b) was estimated through least-squares fit and is summarized in Table 3.3, along with results for the perturbed matrices.

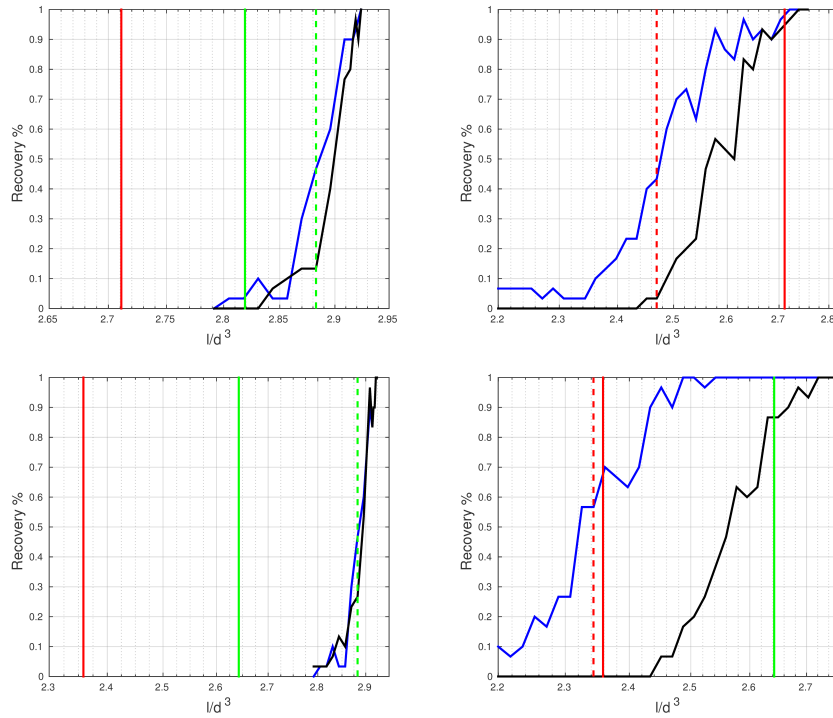


Figure 3.13: Empirical probability ( $6 \times 30$  trials) of exact recovery by total variation minimization (3.7) via the unperturbed (blue line) and perturbed (black line) matrices from Section 3.1.1, Fig. 3.3 and Fig. 3.4, for 3 (top row) and 4 (bottom row) projecting directions respectively. Hereby  $d = 41$ . The significance of each curve is identically to the one in Fig. 3.12. Scaling factors are summarized in Table 3.3.

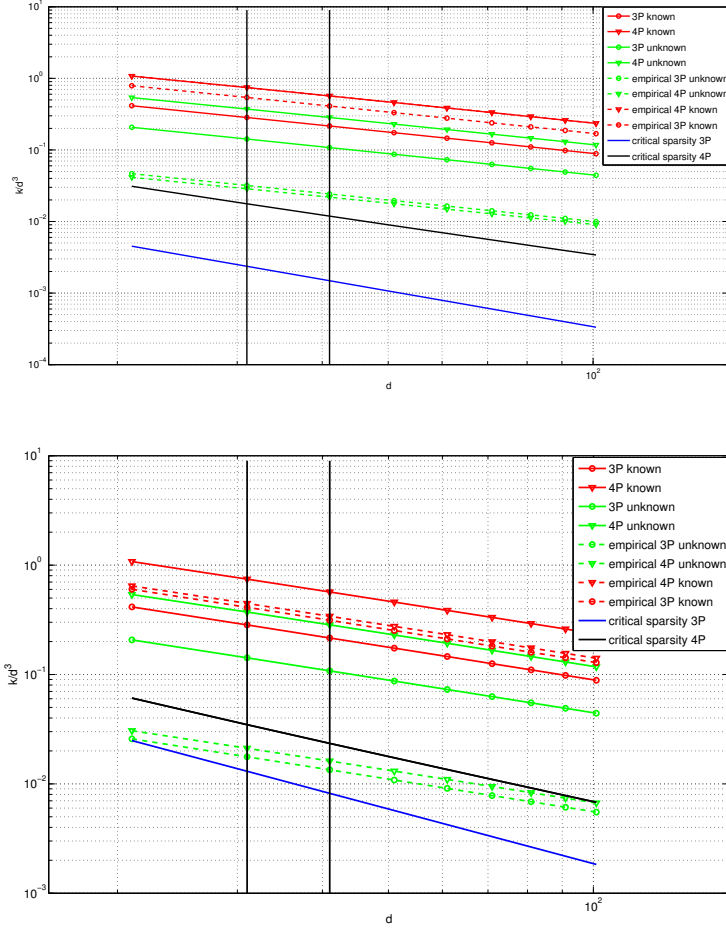


Figure 3.14: Log-log plot of phase transitions in 3D for the unperturbed matrix  $A$  (top), and perturbed matrix  $\tilde{A}$  (bottom) for 3 ( $\circ$ -marked curves) and 4 projecting directions ( $\nabla$ -marked curves). The continuous green and red lines depict the theoretical curves (3.22b) and (3.21b) respectively. The dashed lines correspond to the empirical thresholds, which are all scaled versions of (3.22b) or (3.21b) with scaling factors summarized in Table. 3.3. The blue (stands for 3 projecting directions) and black (stands for 4 projecting directions) curves show the relative critical sparsity such that  $k$  random points are recovered *exactly* by (3.5). These are the theoretical phase transition  $\ell_1$ -recovery from [95], [96]. The vertical lines correspond to  $d = 31$  and  $d = 41$ , compare with Fig. 3.12 and Fig. 3.13.

---

---

## CHAPTER 4

---

# RECOVERY ALGORITHMS: PERTURBED DUAL APPROACH

In the previous chapter, we were able to predict the number of measurements required for the unique reconstruction of a class of cosparsely dense 2D and 3D signals in severely undersampled scenarios by convex programming. These results extend established  $\ell_1$ -related theory based on cosparsity of the signal itself to novel scenarios not covered so far, including tomographic projections of 3D solid bodies composed of few different materials. As a consequence, the large-scale optimization task based on total-variation minimization subject to tomographic projection constraints is considerably more complex than basic  $\ell_1$ -programming for sparse regularization.

This chapter looks closer into large-scale optimization routines, by analysing different perturbation schemes of the objective function (4.2). The problems are solved using efficient methodologies from unconstrained optimization with regard to dual programs.

We give a brief overview of the following lines: in Sect. 4.1 we introduce our problem with the help of linear programming theory. Sect. 4.2 develops on the problem tackled in Sect. 4.1, by perturbing (4.5) with an entropy term and later on, with a quadratic perturbation term. Using notions of duality, we are able to find a global optimum solution to our problems. Following a similar perturbation principle, adding a quadratic term to the objective function (4.2), we solve the corresponding optimization problem in a continuous - discrete alternating manner, in Sect. 4.4. For the continuous case, we consider duality principles to obtain an end solution, while for the discrete minimization step we rely on graph-cuts to obtain a segmented image. An empirical comparison between algorithms that are most favourably used to solve problems of the type (4.2), already introduced in Sect. 2.1.1.4, and the routines mentioned in this chapter and Chapter 3 is

given in Sect. 4.3. Lastly, we give an overview of the take home messages of this chapter in Sect. 4.5.

## 4.1 TV-Recovery by Linear Programming

We consider the discretized TV-term

$$\text{TV}(u) := \|Bu\|_1, \quad B := \begin{pmatrix} \partial_1 \otimes I \otimes I \\ I \otimes \partial_2 \otimes I \\ I \otimes I \otimes \partial_3 \end{pmatrix} \in \mathbb{R}^{p \times n}, \quad (4.1)$$

an additional nonnegative constraint on image  $u$  and express  $Bu = z$ . Thus, (3.6) becomes

$$\min_{u,z} \|z\|_1 \quad \text{s.t.} \quad Bu = z, \quad Au = b, \quad u \geq 0. \quad (4.2)$$

### 4.1.1 Primal Linear Program and its Dual

By splitting the variable  $z$  in its positive  $v^1 := \max\{0, z\}$  and negative part  $v^2 := -\min\{0, z\}$  we convert problem (4.2) into a linear program in normal form. With

$$M := \begin{pmatrix} B & -I & I \\ A & 0 & 0 \end{pmatrix}, \quad q := \begin{pmatrix} 0 \\ b \end{pmatrix}, \quad (4.3)$$

and the polyhedral set

$$\mathcal{P} := \{y \in \mathbb{R}^{n+2p} : Mx = q, x \geq 0\}, \quad x := \begin{pmatrix} u \\ v^1 \\ v^2 \end{pmatrix}, \quad (4.4)$$

problem (4.2) becomes the linear program ( $P$ )

$$(P) \quad \min_{x \in \mathcal{P}} \langle c, x \rangle = \min_{(u,v^1,v^2) \in \mathcal{P}} \langle \mathbb{1}, v^1 + v^2 \rangle, \quad c = \begin{pmatrix} 0 \\ \mathbb{1} \\ \mathbb{1} \end{pmatrix}. \quad (4.5)$$

We further assume that  $\mathcal{P} \neq \emptyset$ , i.e. a feasible solution always exists. Due to  $c \geq 0$ , the linear objective in ( $P$ ) is bounded on  $\mathcal{P}$ . Thus ( $P$ ) always has a solution under the feasibility assumption. In view of basic linear programming theory, compare [99, 11.43], the dual program also has a solution. The dual program ( $D$ ) reads

$$(D) \quad \min_y -\langle q, y \rangle, \quad M^\top y \leq c.$$

With

$$y = \begin{pmatrix} y_0 \\ y_b \end{pmatrix}, \quad M^\top = \begin{pmatrix} B^\top & A^\top \\ -I & 0 \\ I & 0 \end{pmatrix}, \quad M^\top y = \begin{pmatrix} B^\top y_0 + A^\top y_b \\ -y_0 \\ y_0 \end{pmatrix}, \quad (4.6)$$

this reads

$$\min_{y_0, y_b} -\langle b, y_b \rangle \quad \text{s.t.} \quad B^\top y_0 + A^\top y_b \leq 0, \quad -1 \leq y_0 \leq 1. \quad (4.7)$$

Moreover, both primal and dual solutions  $(\bar{x}, \bar{y})$  will satisfy the following optimality conditions

$$0 \leq c - M^\top \bar{y} \perp \bar{x} \geq 0, \quad (4.8)$$

$$M\bar{x} = q. \quad (4.9)$$

### 4.1.2 Uniqueness of Primal LP

A classical argument for replacing  $\|\cdot\|_0$  by  $\|\cdot\|_1$  and solving for (4.2) is uniqueness of the minimal  $\ell_1$  (thus LP) solution. Let  $\bar{x} = (\bar{u}, \bar{v}) = (\bar{u}, \bar{v}^1, \bar{v}^2)$  be  $\ell$ -cosparsely and solve (4.5). We assume throughout

$$\bar{u}_i > 0, \quad i \in [n]. \quad (4.10)$$

Based on  $\bar{x}$ , we define the corresponding support set

$$J := \{i \in [\dim(x)]: \bar{x}_i \neq 0\} = \text{supp}(\bar{x}), \quad \bar{J} := J^c = [\dim(x)] \setminus J. \quad (4.11)$$

Denoting  $k := p - \ell$  the cardinality of the index sets  $J$  and  $\bar{J}$  is

$$|\bar{J}| = 2\ell + k = p + \ell, \quad |J| = n + 2p - |\bar{J}| = n + k, \quad (4.12)$$

compare [34, Lem. 5.3]. This shows that  $\bar{x} \in \mathbb{R}^{n+2p}$  is a  $(n+k)$ -sparse vector.

**Theorem 4.1.1** ([84, Thm. 2(iii)]). *Let  $\bar{x}$  be a solution of the linear program (4.5). The following statements are equivalent:*

(i)  $\bar{x}$  is unique.

(ii) There exists no  $x$  satisfying

$$Mx = 0, \quad x_{\bar{J}} \geq 0, \quad \langle c, x \rangle \leq 0, \quad x \neq 0. \quad (4.13)$$

Theorem (4.1.1) can be turned into a *nullspace condition* w.r.t. the sensor matrix  $A$ , for the unique solvability of problems (4.5) and (4.2).

**Proposition 4.1.2** ([34, Cor. 5.3]). *Let  $\bar{x} = (\bar{u}, \bar{v}^1, \bar{v}^2)$  be a solution of the linear program (4.5) with component  $\bar{u}$  that has cosupport  $\Lambda$  with respect to  $B$ . Then  $\bar{x}$ , resp.  $\bar{u}$ , are unique if and only if*

$$\forall x = \begin{pmatrix} u \\ v \end{pmatrix}, v = \begin{pmatrix} v^1 \\ v^2 \end{pmatrix} \quad \text{s.t.} \quad u \in \mathcal{N}(A) \setminus \{0\} \quad \text{and} \quad Bu = v^1 - v^2 \quad (4.14)$$

the condition

$$\|(Bu)_\Lambda\|_1 > \langle (Bu)_{\Lambda^c}, \text{sign}(B\bar{u})_{\Lambda^c} \rangle \quad (4.15)$$

holds. Furthermore, any unknown  $\ell$ -cosparsely vector  $u^*$ , with  $Au^* = b$ , can be uniquely recovered as solution  $\bar{u} = u^*$  to (4.2) if and only if, for all vectors  $u$  conforming to (4.14), the condition

$$\|(Bu)_\Lambda\|_1 > \sup_{\Lambda \subset [p]: |\Lambda|=\ell} \sup_{\bar{u} \in \mathcal{N}(B_\Lambda)} \langle (Bu)_{\Lambda^c}, \text{sign}(B\bar{u})_{\Lambda^c} \rangle \quad (4.16)$$

holds.

**Remark 4.1.1.** Conditions (4.15) and (4.16) clearly indicate the direct influence of cosparsity on the recovery performance: if  $\ell = |\Lambda|$  increases, then these conditions will more likely hold. On the other hand, these results are mainly theoretical since numerically checking (4.16) is infeasible. However, we will assume that uniqueness of (4.2) is given, provided that the cosparsity  $\ell$  of the unique solution  $\bar{u}$  satisfies the conditions in (3.22a) and (3.22b). This assumption is motivated by the comprehensive experimental assessment of recovery properties reported in Chapter 3, Sect. 3.5.

**Remark 4.1.2.** We note that, besides the condition for uniqueness from Thm. (4.1.1), a LP solution is unique if there is a unique feasible point. For high cosparsity levels  $\ell$ , this seems to be often the case.

Let  $\bar{x}$  be a (possibly unique) primal solution of  $(P)$  and  $\bar{y}$  a dual solution. In view of (4.11) and (4.8) we have

$$(c - M^\top \bar{y})_i = 0, \quad \forall i \in J. \quad (4.17)$$

We note that non-degeneracy of the primal-dual pair  $(\bar{x}, \bar{y})$  implies uniqueness of the dual variable  $\bar{y}$ .

## 4.2 Recovery by Perturbed Linear Programming

### 4.2.1 Entropic Perturbation and Exponential Penalty.

In various approaches to solving large-scale linear programs, one regularizes the problem by adding to the linear cost function a separable nonlinear function

multiplied by a small positive parameter. Popular choices of this nonlinear function include the quadratic function, the logarithm function, and the negative  $\langle x, \log(x) \rangle$ -entropy function. Our main motivation in following this trend is that by adding a strictly convex and separable perturbation function, the dual problem will become unconstrained and differentiable. Consider

$$(P_\varepsilon) \quad \min \langle c, x \rangle + \varepsilon \langle x, \log x - \mathbb{1} \rangle \quad \text{s.t.} \quad Mx = q, x \geq 0 . \quad (4.18)$$

The perturbation approach by the entropy function was studied by Fang et al. [49, 50] and, from a dual exponential penalty view, by Cominetti et al. [32].

**The Unconstrained Dual.** We write  $(P_\varepsilon)$  (4.18) in the form (2.6a)

$$\min \varphi(x), \quad \varphi(x) := \langle c, x \rangle + \underbrace{\varepsilon \langle x, \log x - \mathbb{1} \rangle + \delta_{\mathbb{R}_+^n}(x)}_{:=f(x)} + \delta_0(q - Mx) . \quad (4.19)$$

With  $g := \delta_0$ , we get  $g^* \equiv 0$ , since  $\delta_C^* \equiv \sigma_C$  and thus

$$g^*(y) = \delta_0^*(y) = \sigma_0(y) = \sup_{z=0} \langle y, z \rangle = 0, \quad \forall y \in \mathbb{R}^n$$

holds. On the other hand, we have  $f^*(y) = \varepsilon \langle \mathbb{1}, e^{\frac{y}{\varepsilon}} \rangle$ . Now (2.6b) gives immediately the dual problem

$$\sup \psi(y), \quad \psi(y) := \langle q, y \rangle - \varepsilon \langle \mathbb{1}, e^{\frac{M^\top y - c}{\varepsilon}} \rangle . \quad (4.20)$$

We note that  $\psi$  is unconstrained and twice differentiable with

$$\nabla \psi(y) = q - M e^{\frac{M^\top y - c}{\varepsilon}} \quad \text{and} \quad (4.21a)$$

$$\nabla^2 \psi(y) = -\frac{1}{\varepsilon} M \text{diag} e^{\frac{M^\top y - c}{\varepsilon}} M^\top . \quad (4.21b)$$

Moreover,  $-\nabla^2 \psi \succ 0$  for all  $y$ , with  $e^{\frac{M^\top y - c}{\varepsilon}} \in \mathcal{R}(M) = \mathcal{N}(M)^\perp$ , in view of (4.21b). Note that if  $\psi$  has a solution then it is unique and the strictly feasible set must be nonempty, see (4.21a), thus  $\text{rint } \mathcal{P} = \{x: Mx = q, x > 0\} \neq \emptyset \Leftrightarrow q \in M(\mathbb{R}_{++}^n)$ . Further we can rewrite (4.20) in more detailed form in view of (4.6)

$$(D_\varepsilon) \quad \min_{y_0, y_b} -\langle b, y_b \rangle + \varepsilon \langle \mathbb{1}_n, e^{\frac{B^\top y_0 + A^\top y_b}{\varepsilon}} \rangle + \varepsilon \langle \mathbb{1}_p, e^{\frac{-y_0 - \mathbb{1}_p}{\varepsilon}} \rangle + \varepsilon \langle \mathbb{1}_p, e^{\frac{y_0 - \mathbb{1}_p}{\varepsilon}} \rangle . \quad (4.22)$$

**Connecting Primal and Dual Variables.** With  $\text{dom } g = 0$ ,  $\text{dom } g^* = \mathbb{R}^n$ ,  $\text{dom } f^* = \mathbb{R}^n$  and  $\text{dom } f = \mathbb{R}_+^n$ , the assumptions (2.7) become  $q \in \text{int } M(\mathbb{R}_+^n) = M(\text{int } \mathbb{R}_+^n) = M(\mathbb{R}_{++}^n)$ , compare [99, Prop. 2.44], and  $c \in \text{int } \mathbb{R}^n = \mathbb{R}^n$ . Thus, under the assumption of a strictly feasible set, we have no duality gap. Moreover both problems (4.19) and (4.20) have a solution.

**Theorem 4.2.1.** Denote by  $x_\varepsilon$  and  $y_\varepsilon$  a solution of  $(P_\varepsilon)$  and  $(D_\varepsilon)$  respectively. Then the following statements are equivalent:

(a)  $q \in M(\mathbb{R}_{++}^n)$ , thus the strictly feasible set is nonempty.

(b) The duality gap is zero  $\psi(y_\varepsilon) = \varphi(x_\varepsilon)$ .

(c) Solutions  $x_\varepsilon$  and  $y_\varepsilon$  of  $(P_\varepsilon)$  and  $(D_\varepsilon)$  exist and are connected through

$$x_\varepsilon = e^{\frac{M^\top y_\varepsilon - c}{\varepsilon}}. \quad (4.23)$$

*Proof.* (a)  $\Rightarrow$  (b): holds due duality. On the other hand, (b) implies solvability of  $\psi$  and thus (a), as noted after Eq. (4.21b). (a)  $\Rightarrow$  (c): The assumptions of Thm. (2.1.1) hold. Now  $\partial f^*(y) = \{\nabla f^*(y)\} = \{e^{\frac{y}{\varepsilon}}\}$  and the r.h.s. of (2.9a) gives (c). Now, (c) implies  $Mx_\varepsilon = q$  and thus (a).  $\square$

The following result shows that for  $\varepsilon \rightarrow 0$  and under the nonempty strictly feasible set assumption,  $x_\varepsilon$  given by (4.23) approaches the least-entropy solution of  $(P)$ , if  $y_\varepsilon$  is a solution of  $(D_\varepsilon)$ . The proof follows along the lines of [112, Prop. 1].

**Theorem 4.2.2.** Denote the solution set of (4.5) by  $\mathcal{S}$ . Assume  $\mathcal{S} \neq \emptyset$  and  $\text{rint } \mathcal{P} \neq \emptyset$ . Then, for any sequence of positive scalars  $(\varepsilon_k)$  tending to zero and any sequence of vectors  $(x_{\varepsilon_k})$ , converging to some  $x^*$ , we have  $x^* \in \text{argmin}_{x \in \mathcal{S}} \langle x, \log x - \mathbb{1} \rangle$ . If  $\mathcal{S}$  is a singleton, denoted by  $\bar{x}$ , then  $x_{\varepsilon_k} \rightarrow \bar{x}$ .

**Partial Perturbation.** In the case of a unique and sparse feasible point  $\bar{x}$  the assumption  $q \in M(\mathbb{R}_{++}^n)$  does not hold. With  $J = \text{supp}(\bar{x})$  the primal reads

$$\min \langle c, x \rangle + \varepsilon \langle x_J, \log x_J - \mathbb{1}_J \rangle \quad \text{s.t.} \quad Mx = q, x_{J^c} = 0, x \geq 0,$$

and the dual becomes

$$\max_y \langle q, y \rangle - \varepsilon \langle \mathbb{1}, e^{\frac{(M^\top)_J y - c_J}{\varepsilon}} \rangle.$$

However, the solution support  $J$  is unknown. Using (4.17), one can show that an approximative solution  $y_\varepsilon$  of  $(D_\varepsilon)$ , i.e.  $\|\nabla \psi(y_\varepsilon)\| \leq \tau_\varepsilon$ , with  $\tau_\varepsilon > 0$  small, can be used to construct  $x_\varepsilon$  according to (4.23), such that  $x_\varepsilon \rightarrow \bar{x}$ .

**Exponential Penalty Method.** We discussed above how problem  $(P_\varepsilon)$  tends to  $(P)$  as  $\varepsilon \rightarrow 0$ . Likewise,  $(D_\varepsilon)$  tends to  $(D)$ . This was shown by Cominetti et al. [32, Prop. 3.1]. The authors noticed that the problem  $(D_\varepsilon)$  is an exponential penalty formulation of  $(D)$ , compare (4.6) and (4.22).

They also investigated the asymptotic behavior of the trajectory  $y_\varepsilon$  and its relation with the solution set of  $(D)$ . They proved the trajectory  $y_\varepsilon$  is approximately a straight line directed towards the center of the optimal face of  $(D)$ , namely  $y_\varepsilon = y^* + \varepsilon d^* + \eta(\varepsilon)$ , where  $y^*$  is a particular solution of  $(D)$ . Moreover, the error  $\eta(\varepsilon)$  goes to zero exponentially fast, i.e. at the speed of  $e^{-\frac{\mu}{\varepsilon}}$  for some  $\mu > 0$ . See the proof of [32, Prop. 3.2].

### 4.2.2 Quadratic Perturbation

In this section we consider a quadratic perturbation of

$$\min_{z,u} \|z\|_1 \quad \text{s.t.} \quad Au = b, Bu = z, \quad (4.24)$$

with  $B = \nabla$ .

We denote by  $M := \begin{pmatrix} A & 0 \\ B & -I \end{pmatrix}$ ,  $q := \begin{pmatrix} b \\ 0 \end{pmatrix}$  and  $x := \begin{pmatrix} u \\ z \end{pmatrix}$ . With a *finite* perturbation parameter  $\lambda > 0$  the quadratic perturbation (4.24) written in the form of (2.6a) is

$$\min \varphi(x), \quad \varphi(x) := \underbrace{\lambda\|z\|_1 + \frac{1}{2}\|z\|_2^2 + \frac{1}{2}\|u\|_2^2}_{:=f(u,z)} + \underbrace{\delta_0}_{:=g}(q - Mx). \quad (4.25)$$

With

$$f(u, z) = f_1(u) + f_2(z), \quad f_1(u) = \frac{1}{2}\|u\|_2^2, \quad f_2(z) = \lambda\|z\|_1 + \frac{1}{2}\|z\|_2^2,$$

using  $f^* = f_1^* + f_2^*$  and

$$f_1^*(y) = \frac{1}{2}\|y\|^2, \quad f_2^*(y) = \frac{1}{2}\|S_\lambda(y)\|^2,$$

the dual (2.6b) becomes

$$\min \psi(y), \quad \psi(y) := -\langle q, y \rangle + \frac{1}{2}\|A^\top y_b + B^\top y_0\|_2^2 + \frac{1}{2}\|S_\lambda(-y_0)\|_2^2, \quad (4.26)$$

where we denote  $y = \begin{pmatrix} y_b \\ y_0 \end{pmatrix}$ . Using the subgradient inversion formula  $\nabla f_2^* = (\partial f_2)^{-1}$  we get  $\nabla f_2^*(y) = S_\lambda(y)$ , with  $S_\lambda(y)$  denoting the soft-thresholding operator, in view of

$$\partial_i f_2(z) = \begin{cases} \lambda \operatorname{sign}(z_i) + z_i, & z_i \neq 0, \\ [-\lambda, \lambda], & z_i = 0. \end{cases} \quad (4.27)$$

Thus, the dual (4.26) is differentiable with

$$\nabla \psi(y) = -q + M \begin{pmatrix} A^\top y_b + B^\top y_0 \\ S_\lambda(-y_0) \end{pmatrix}.$$

Assuming a feasible solution exists to (4.24), both primal (4.25) and dual (4.26) problems have a solution, the duality gap is zero and the primal and dual solution pair  $(x^\lambda, y^\lambda)$  are connected through

$$x^\lambda = \begin{pmatrix} A^\top y_b^\lambda + B^\top y_0^\lambda \\ S_\lambda(-y_0^\lambda) \end{pmatrix}.$$

The advantage of this formulation is that due to the differentiability and strong convexity of  $f$  the perturbation is finite. This means that there is a large, but finite,  $\bar{\lambda} > 0$  such that solving (4.25) one obtains for all  $\lambda \geq \bar{\lambda}$  a solution of (4.24) by solving (4.25), e.g. via (4.26), compare [51, 55]. However, this perturbation parameter  $\bar{\lambda}$  depends on the unknown solution  $x^\lambda$ .

### 4.2.3 Numerical Experiments

We illustrate the performance of our perturbation approach compared to the LP solver MOSEK, in noisy and non-noisy environments, for 2D and 3D cases. We implemented the entropic and quadratic approach and solved the perturbed dual formulations by a conventional unconstrained optimization approach, the *Limited Memory BFGS* algorithm, see [11], which scales to large problem sizes. In all experiments, the perturbation parameters were kept fixed to  $\varepsilon = 1/50$  (see Fig. 4.3 for a justification) and  $\lambda = 0.85$ . We allowed a maximum number of 1500 iterations and stopped when the norm of the gradient of the perturbed dual function satisfies  $\|\nabla\psi(y^k)\| \leq 10^{-4}$ .

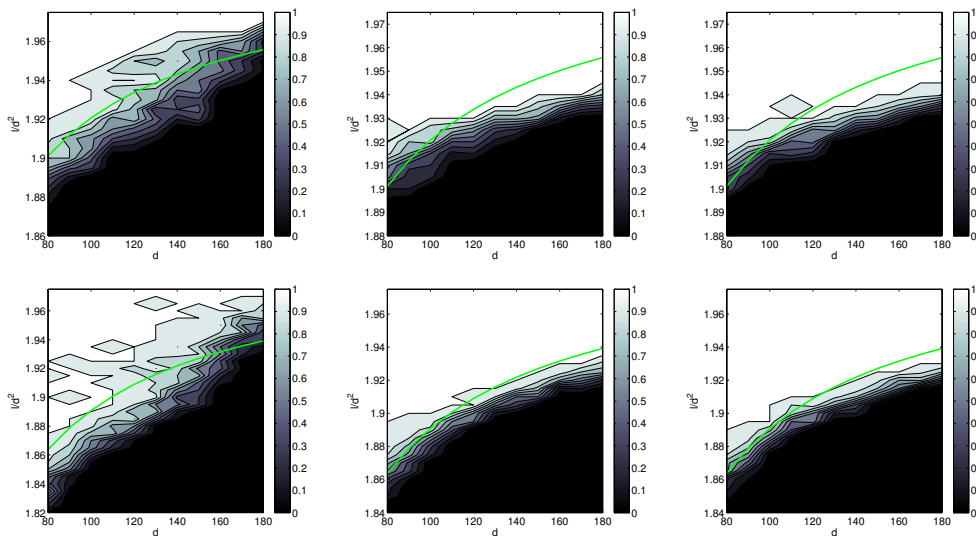


Figure 4.1: Phase transitions for the 2D case, 4 cameras (top row) and 6 cameras (bottom row), computed for the noiseless case with MOSEK (left column), our approach (middle column) and our approach for the noisy case (right column). The green solid line corresponds to the theoretical curve (3.22a).

The first performance test was done on 2D  $d \times d$  images of randomly located ellipsoids with random radii along the coordinate axes. See Fig. 4.2 (right) for two sample images. The relative cosparsity is denoted by  $\rho := \frac{\ell}{n}$ . Parameters  $p$

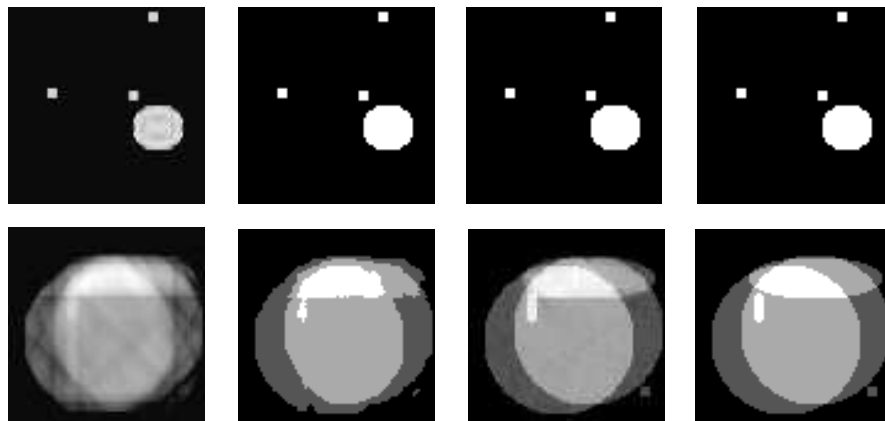


Figure 4.2: Comparison between the quadratic perturbation approach (left two columns) and entropic perturbation approach (right two columns) for two relative cosparsity levels. Two  $80 \times 80$  images, are projected along 6 directions. For both  $\rho = \ell/d^2 = 1.7786$  (top row) and  $\rho = \ell/d^2 = 1.8586$  (bottom row) reconstruction should in theory be *exact*. Result (left column) and rounded result (second left column) of the quadratic perturbation approach for  $\alpha = 1$ . Results for the entropic perturbation approach (right two columns) with  $\varepsilon = 1/50$ . Here the rounded result *exactly equals* the original image (right column).

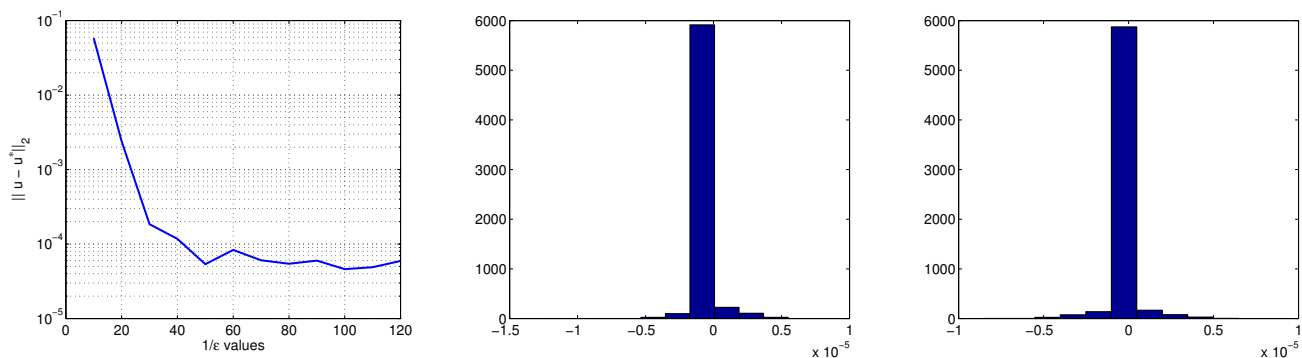


Figure 4.3: Experimental finite perturbation property of the entropic approach. Here  $\varepsilon = 1/50$  is a reasonable value since the reconstruction error varies insignificantly (left). The histograms of  $(u - u^*)$  for  $\varepsilon = 1/50$  (middle) and  $\varepsilon = 1/120$  (right) are highly similar.

and  $n$  vary for two- and three-dimensional images as

$$n = \begin{cases} d^2 & \text{in 2D} \\ d^3 & \text{in 3D} \end{cases}, \quad p = \begin{cases} 2d(d-1) & \text{in 2D} \\ 3d^2(d-1) & \text{in 3D} \end{cases}. \quad (4.28)$$

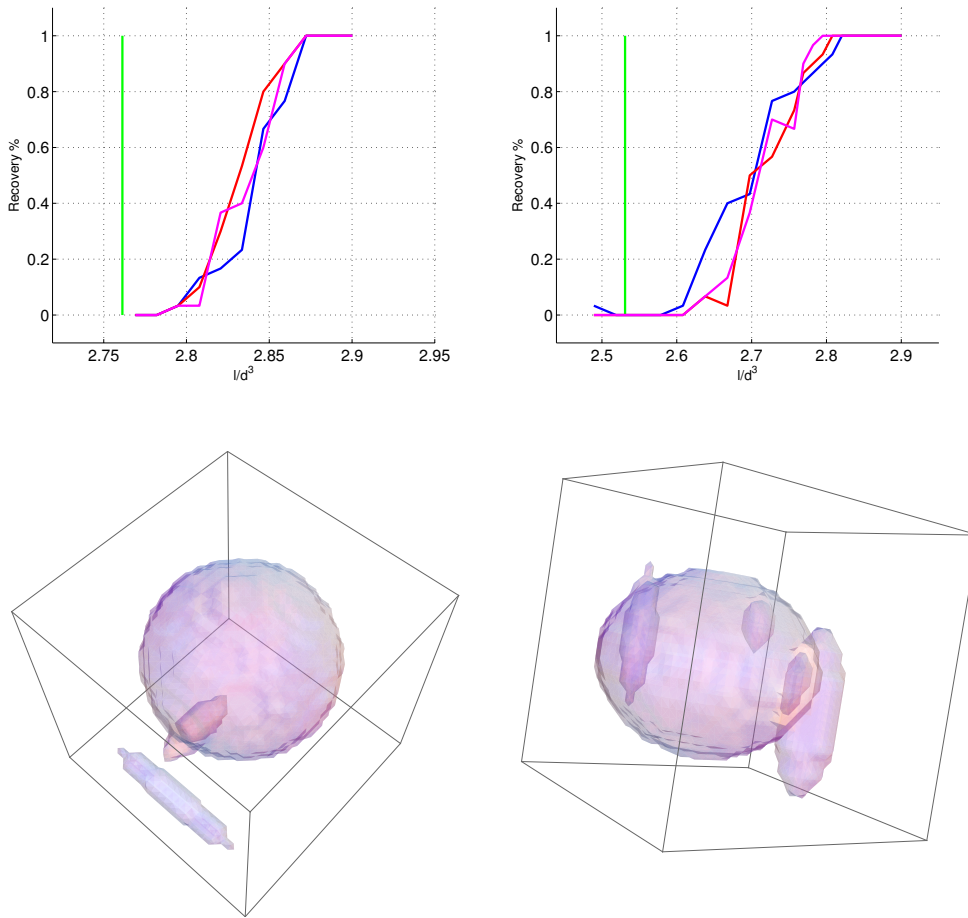


Figure 4.4: Phase transitions for the 3D case, 3 cameras (top left) and 4 cameras (top right) and random example of perfectly reconstructed images  $d = 31$  (bottom). The average performance of MOSEK (blue line) for the noiseless case, and the entropic approach in the noiseless (red line) and noisy (magenta line) case for  $\varepsilon = 1/50$  as a variation of relative sparsity. The green solid line corresponds to the theoretical curve (3.22b). Measurements were corrupted by Poisson noise of  $\text{SNR} = 50\text{db}$ .

Our parametrization relates to the design of the projection matrices  $A \in \mathbb{R}^{m \times n}$ , see Sect. 3.1 for details.

The phase transitions in Fig. 4.1 display the empirical probability of exact recovery over the space of parameters that characterize the problem. Here we performed 90 tests for each  $(\rho, d)$  parameter combination.

We analysed the influence of the image sparsity, also for 3D images, see Fig. 4.4. In 3D, for each problem instance defined by a  $(\rho, d)$ -point, we generated

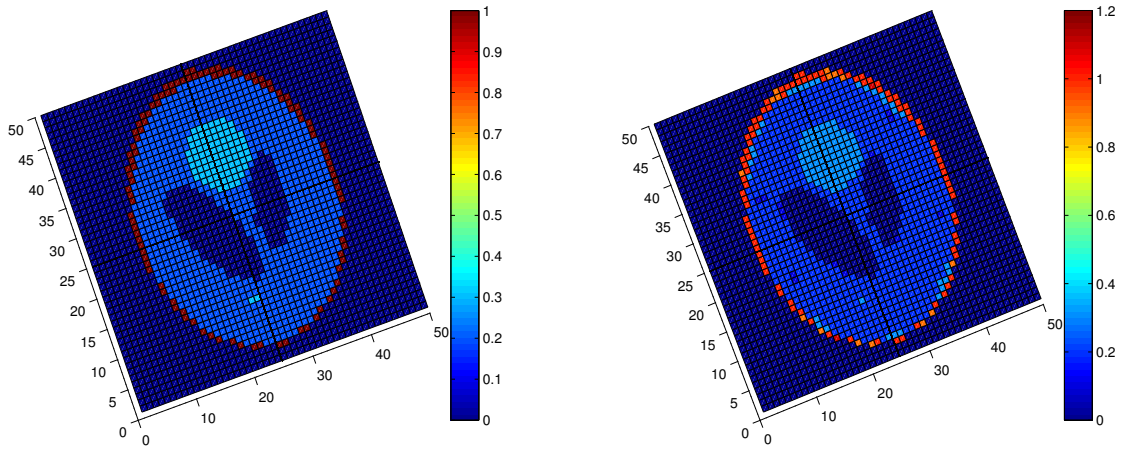


Figure 4.5: Slices through the 3D volume of an original Shepp-Logan image (left) and the reconstructed image from 7 *noisy* projecting directions via the entropic perturbation approach, satisfying  $\|u - u^*\|_\infty < 0.5$  (right). This shows that the approach is also stable for low noise levels as opposed to MOSEK. Measurements were corrupted by Poisson noise of SNR = 50db.

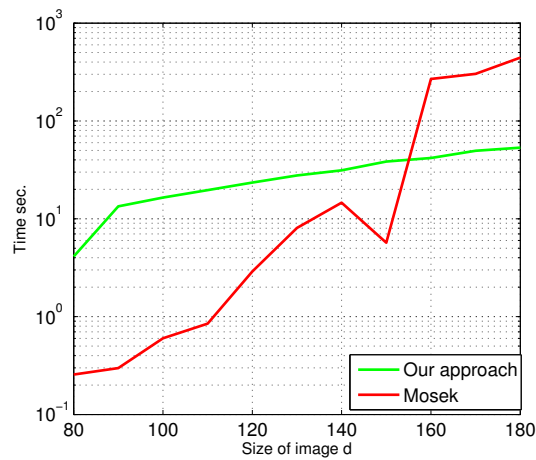


Figure 4.6: Comparison between computation times of the proposed approach and MOSEK.

60 random images. In both 2D and 3D, we declared a random test as successful if  $\|u - u^*\|_\infty < 0.5$ , which leads to perfect reconstruction after rounding. Both Fig. 4.1 and Fig. 4.4 display a phase transition and exhibit regions where exact image reconstruction has probability equal or close to one and closely match the

solid green line in the plots, which stands for the theoretical curve (3.22a). In the noisy case, projection data was corrupted by Poisson noise of  $SNR = 50\text{db}$ . The perturbation parameter has been set as in the noiseless case, i.e.  $\varepsilon = 1/50$  and  $\lambda = 0.85$ . MOSEK however was unable to solve the given problem, stating that either the primal or the dual might be infeasible. Thus our perturbation approach is also stable to low noise levels as opposed to MOSEK. Moreover the proposed algorithm scales much better with the problem size and is significantly more efficient for large problem sizes that are relevant to applications. In particular, problems sizes can be handled where MOSEK stalls, see Fig. 4.6. Finally, we underline that the entropic perturbation approach performs significantly better than quadratic perturbation as shown in Fig. 4.2.

### 4.3 Algorithm Comparisons

The role of this section is to compare the behaviour of FISTA, Douglas-Rachford (DR) and Chambolle-Pock (CP) algorithms with the methods we developed in Chapter 3 and 4. As test image, we will use the Shepp-Logan phantom of dimensions  $50 \times 50$ , known to be the standard image used for testing algorithms intended for ill-posed tomographic reconstructions problems. The three algorithms CP, DR and FISTA are run each for 1500 iterations, after which the result is shown. Through Fig. 4.7 we show that this choice of number of iterations is sufficient enough, considering the outcome of the residual at each iteration. For the other algorithms, we used the same parameters as stated in the corresponding sections where they were presented. For the entropic and quadratic perturbation the output is shown after rounding. For rounding, we increased the image scale multiplying the algorithm output by 10. Next, we rounded and then divided this result by 10, to come back to the initial scale, i.e.  $[0, 1]$ .

In Table 4.1 we summarize the functions considered for FISTA, DR, CP, while in Table 4.2 we present the output of each routine, applying the 8 camera projection matrix mentioned in Sect. 3.1.

Alg.	$f(x)$	$g(x)$	Extra remarks
FISTA	$\ \nabla x\ _1$	$\ Ax - b\ _2^2$	$\lambda = 1e - 05$
DR	$\delta_C(x)$	$\ \nabla x\ _1$	$C = \{x : Ax = b\}, \lambda = 5e - 03$
CP	$\frac{1}{2}\ Ax - b\ _2^2 + \lambda\ \nabla x\ _1$	0	$K = \begin{pmatrix} A \\ \nabla \end{pmatrix}, \lambda = 1e - 01.$

Table 4.1: Summary of the functions used in algorithms presented in Sect. 2.1.1.4.

A few comments are in order, concerning the remarks column. For the Douglas-Rachford algorithm, parameter  $\lambda$  is used in the computation of the Total Variation

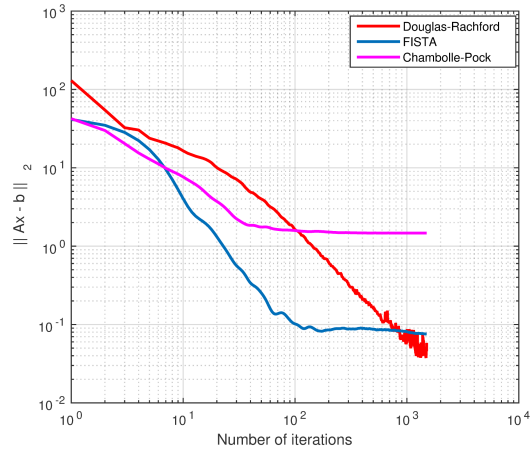
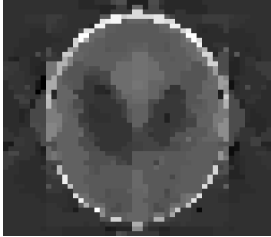
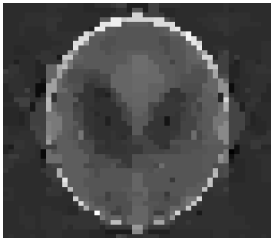
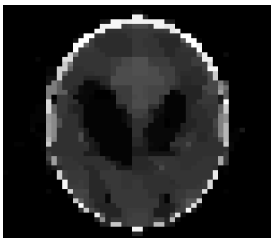


Figure 4.7: Graphical illustration of the residual along the computation lines of the Douglas-Rachford, FISTA and Chambolle-Pock algorithms.

proximal operator and the formation of the matrix  $K$  in the implementation of the Chambolle-Pock primal-dual algorithm is well documented in [104], Alg. 4. We also report that our implementation of the CP primal-dual routine is based on the paper of [104].

### 4.3. ALGORITHM COMPARISONS

Algorithm	Reconstruction	$\ \text{Orig} - \text{Rec}\ _2$	Time (sec.)
FISTA		4.8951	29.6091
Douglas Rachford		4.6924	85.0362
Chambolle Pock		3.3487	25.4830
Mosek		1.2874	1.03
Entropy		1.3820	13.38

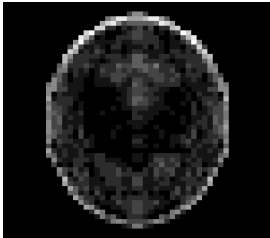
Quadratic		5.6040	3.7131
-----------	---	--------	--------

Table 4.2: Output of implemented algorithms. First column depicts the end result of the reconstruction algorithm. Second column contains the values for the  $L_2$  norm difference between the original and the reconstructed image, while in the third column we give the computation times required for each method.

## 4.4 Continuous / Discrete Interplay

We take upon the idea of Maeda et. al. [83] as the underlying basis of the approach we will present next. A brief review of its contents has already been given in Sect. 2.2.3.4. Our interest hereafter lies in solving problem (4.2) for large-scale problems, i.e. 3D images, by a continuous and discrete alternating minimization technique, similarly to [83].

### 4.4.1 Continuous minimization

We remind the reader the energy function that is minimized in [83], in an alternating manner:

$$E(u, v) = -\ln p(\mathcal{D}|u) - \ln p(u|v) - \ln p(v).$$

For the continuous case, [83] considers

$$\begin{aligned} \hat{u} &= \operatorname{argmin}_u E(u, \hat{v}) \\ &= \operatorname{argmin}_u -\ln p(\mathcal{D}|u) - \ln p(u|\hat{v}), \end{aligned} \quad (4.29)$$

and solves the minimization problem with respect to  $u$ , by using the *scaled conjugate gradient* method. A very popular approach in solving Maximum-Likelihood problems is *expectation - maximization* (EM). Its preference over other methods lay in its theoretical and practical properties. Numerous implementations of EM can be found in the literature, either as a stand along routine, or in connection with Total Variation minimization, or variations, among which we mention: [78], [92], [118], Ordered Subset Expectation Maximization (OSEM) [46].

However, based on our recent results in Sect. 4.2.3, Fig. 4.1, where perturbation showed an improvement in the number of accurately reconstructed images, and

because we want to solve problems of the form (4.2) in a deterministic way, we aim at solving a *perturbed quadratic penalty* instance of (4.2):

$$\min_u \|\nabla u\|_1 + \frac{\alpha}{2}\|u - v\|_2^2 \quad \text{s.t.} \quad Au = b, u \geq 0, \quad (4.30)$$

which is equivalent to

$$\min_{z,u} \|z\|_1 + \frac{\alpha}{2}\|u\|_2^2 - \langle \alpha v, u \rangle \quad \text{s.t.} \quad Au = b, \nabla u = z, u \geq 0. \quad (4.31)$$

$\alpha > 0$  is a regularizing parameter that enforces the solution to the discrete optimization problem "v" to closely fit the solution of the continuous optimization problem "u" and  $\nabla$  is the discrete gradient operator.

Denoting  $M := \begin{pmatrix} A & 0 \\ \nabla & -I \end{pmatrix}$ ,  $q := \begin{pmatrix} b \\ 0 \end{pmatrix}$  and  $x := \begin{pmatrix} u \\ z \end{pmatrix}$ , we consider the quadratic perturbation of (4.31) wrt. to  $z$  by *finite*, but large, perturbation parameter  $\lambda > 0$ . We write (4.31) in the Fenchel duality form (see Sect. 2.1.1.3) and obtain

$$\min \varphi(x), \quad \varphi(x) := \underbrace{\langle c, x \rangle + \lambda\|z\|_1 + \frac{1}{2}\|z\|_2^2 + \frac{\alpha\lambda}{2}\|u\|_2^2 + \delta_{\mathbb{R}_+^n}(u)}_{:=f(u,z)} + \underbrace{\delta_0(q - Mx)}_{:=g}. \quad (4.32)$$

With  $c = (-\alpha\lambda v^\top, 0)^\top \in \mathbb{R}^{n+p}$  and

$$f(u, z) = f_1(u) + f_2(z), \quad f_1(u) = \frac{\alpha\lambda}{2}\|u\|_2^2 + \delta_{\mathbb{R}_+^n}(u), \quad f_2(z) = \lambda\|z\|_1 + \frac{1}{2}\|z\|_2^2$$

using  $f^* = f_1^* + f_2^*$  and

$$f_1^*(y) = \frac{1}{2\alpha\lambda}\|\max(0, y)\|_2^2, \quad f_2^*(y) = \frac{1}{2}\|S_\lambda(y)\|_2^2,$$

the dual becomes

$$\min \psi(y), \quad \psi(y) := -\langle q, y \rangle + \frac{1}{2\alpha\lambda}\|\max(0, A^\top y_b + \nabla^\top y_0 + \alpha\lambda v)\|_2^2 + \frac{1}{2}\|S_\lambda(-y_0)\|_2^2, \quad (4.33)$$

where we denote  $y = \begin{pmatrix} y_b \\ y_0 \end{pmatrix}$ .

In view of the fact that the conjugate of the function  $f_2$ , i.e.  $f_2^*$  is continuously differentiable, we can make use of the property of subgradient inversion (Prop. (1)),  $\nabla f_2^* = (\partial f_2)^{-1}$ . This leads to  $\nabla f_2^*(y) = S_\lambda(y)$  in view of

$$\partial_i f_2(z) = \begin{cases} \lambda \text{sign}(z_i) + z_i, & z_i \neq 0, \\ [-\lambda, \lambda], & z_i = 0. \end{cases}$$

On the other hand,  $\nabla f_1^*(y) = \frac{1}{\alpha\lambda} \max(0, y)$ . Thus, the dual is differentiable with

$$\nabla\psi(y) = -q + M \left( \begin{array}{c} \frac{1}{\alpha\lambda} \max(0, A^\top y_b + \nabla^\top y_0 + \alpha\lambda v) \\ S_\lambda(-y_0) \end{array} \right).$$

Assuming a feasible solution exists to (4.31), both primal (4.32) and dual (4.33) problems have a solution, the duality gap is zero and the primal and dual solution pair  $(x^\lambda, y^\lambda)$  are connected through

$$x^\lambda = \left( \begin{array}{c} \frac{1}{\alpha\lambda} \max(0, A^\top y_b + \nabla^\top y_0 + \alpha\lambda v) \\ S_\lambda(-y_0) \end{array} \right).$$

#### 4.4.2 Discrete minimization

We follow the steps taken in Maeda et. al. [83] and use  $\alpha$ -expansion (see Sect. 2.1.3.2) to solve the corresponding optimization problem.

As we are interested in the discrete optimization part, we report this as being:

$$\begin{aligned} \hat{v} &= \operatorname{argmin}_v E(\hat{u}, v) \\ &= \underbrace{-\ln p(u|v)}_{\text{fidelity}} - \underbrace{\ln p(v)}_{\text{regularization}}, \end{aligned} \quad (4.34)$$

where  $u$  is the tomographic image,  $v = \{v_1, v_2, \dots, v_J\}$  is the labelled version of the tomographic image and  $J$  is the number of pixels. Each pixel  $j$  ( $j = 1, 2, \dots, J$ ) is represented by hidden variables  $v_j = [v_{j1}, v_{j2}, \dots, v_{jk}, \dots, v_{jK}]$  with  $K$  being the number of material classes. The convention is to have a material coding such that when a pixel is marked to belong to a certain  $k$  class, the other classes are set to 0. Moreover,  $p(u|v)$  is the conditional prior, reflecting the probability of a CT image to occur, given a fixed labelling of the material classes and  $p(v)$  is the class prior, that plays the role of a regularization term.

In order to use  $\alpha$ -expansion to minimize (4.34), we should be able to express our minimizing function in the form of (2.29), with local functions indexed by a graph  $G = (V, E)$  :

$$E(v) = \sum_{i \in V} D_i(v_i, u_i) + \sum_{(i,j) \in E} V_{i,j}(v_i, v_j). \quad (4.35)$$

The nodes in the  $V$  set correspond to pixels in the CT image and the set  $E$  of edges stands for the neighborhood system used to represent directly interacting variables. Work in this section was jointly made with Matthias Zisler. The following derivations are also found in his master thesis [121].

We begin the transformation towards the  $\alpha$ -expansion formulation by writing explicitly the content of each term in equation (4.34):

$$\begin{aligned} E(v) &:= -\ln p(u|v) - \ln p(v) \\ &= -\ln \left( \prod_{j=1}^J p(u_j|v_j) \right) - \ln \left( \frac{1}{Z} e^{-H(v)} \right) \\ &= -\sum_{j=1}^J \ln p(u_j|v_j) + \ln(Z) + H(v). \end{aligned}$$

Using the definitions of  $p(u_j|v_j)$  and  $H(v)$  from [83], Sect. 2.2 and Sect. 2.3, we are left with

$$\begin{aligned} E(v) &= -\sum_{j=1}^J \ln \prod_{k=1}^K \mathcal{N}(u_j|\nu_k, r_k^2)^{v_{jk}} - \sum_{k=1}^K \left( J_k^{self} \sum_{j=1}^J v_{jk} + J_k^{inter} \sum_{j=1}^J \sum_{i \in \eta(j)} v_{ik} v_{jk} \right) + \ln(Z) \\ &= -\sum_{j=1}^J \sum_{k=1}^K \left( \ln \mathcal{N}(u_j|\nu_k, r_k^2) + J_k^{self} \right) v_{jk} - \sum_{j=1}^J \sum_{i \in \eta(j)} \sum_{k=1}^K J_k^{inter} v_{ik} v_{jk} + \ln(Z) \\ &= -\sum_{j \in V} \sum_{k=1}^K \left( \ln \mathcal{N}(u_j|\nu_k, r_k^2) + J_k^{self} \right) v_{jk} - \sum_{(i,j) \in E} \sum_{k=1}^K J_k^{inter} v_{ik} v_{jk} + \ln(Z), \end{aligned}$$

where the iteration over each pixel  $j$  and their adjacent neighboring pixels  $\eta(j)$  can be expressed as iterating over all  $E$  edges in the system. The term  $\mathcal{N}(\cdot|\nu_k, r_k^2)$ , stands for the normal Gaussian distribution, with mean  $\nu_k$  and variance  $r_k$ . Explicitly, it takes the form

$$\ln \mathcal{N}(u_j|\nu_k, r_k^2) = \ln \left( \frac{1}{\sqrt{2\pi r_k}} e^{-\frac{1}{2} \left( \frac{u_j - \nu_k}{r_k} \right)^2} \right) = \ln(\sqrt{2\pi r_k}) - \frac{1}{2} \left( \frac{u_j - \nu_k}{r_k} \right)^2.$$

Now, we can write the above result in the form of (4.35):

$$\begin{aligned} E(v) &= \sum_{j \in V} \sum_{k=1}^K \underbrace{\left( \ln(\sqrt{2\pi r_k}) + \frac{1}{2} \left( \frac{u_j - \nu_k}{r_k} \right)^2 - J_k^{self} \right)}_{:=D_j(v_j, u_j)} v_{jk} + \\ &+ \sum_{(i,j) \in E} \underbrace{\sum_{k=1}^K -J_k^{inter} v_{ik} v_{jk}}_{:=V_{i,j}(v_i, v_j)} + \underbrace{\ln(Z)}_{ct}, \end{aligned}$$

with  $\ln(Z)$  a term that can be neglected, as it is just a constant when minimizing over  $v$ . At this time, we can formally state the unary and pairwise terms, as

$$D_j(v_j, u_j) := \sum_{k=1}^K \left( \ln(\sqrt{2\pi}r_k) + \frac{1}{2} \left( \frac{u_j - v_k}{r_k} \right)^2 - J_k^{self} \right) v_{jk}$$

$$V_{i,j}(v_i, v_j) := \sum_{k=1}^K -J_k^{inter} v_{ik} v_{jk}.$$

Usually, in graph cut algorithms the unary term can be arbitrary, however the pairwise term must hold submodularity condition to enable the application of a maximum-flow solver as subroutine,

$$V_{i,j}(\alpha, \alpha) + V_{i,j}(\beta, \gamma) \leq V_{i,j}(\alpha, \gamma) + V_{i,j}(\beta, \alpha), \quad \forall \alpha, \beta, \gamma \in \mathcal{L} \quad (4.36)$$

$$\text{with labelling } \mathcal{L} := \{l \in \{0, 1\}^K \mid \sum_{k=1}^K l_k = 1\}.$$

The submodularity condition (4.36) always stands if  $J_k^{inter}$  is assumed to be greater or equal to 0:

$$\alpha = \beta \rightarrow -J_k^{inter} + 0 \leq 0 - J_k^{inter} \quad (4.37)$$

$$\alpha = \gamma \rightarrow -J_k^{inter} + 0 \leq -J_k^{inter} + 0 \quad (4.38)$$

$$\beta = \gamma \rightarrow -J_{k\alpha}^{inter} - J_{k\beta}^{inter} \leq 0 + 0 \quad (4.39)$$

$$\alpha = \beta = \gamma \rightarrow -J_k^{inter} - J_k^{inter} \leq -J_k^{inter} - J_k^{inter}. \quad (4.40)$$

### 4.4.3 Numerical Experiments

For implementation of our tests, we used 3D measurement matrices from the AirTools<sup>1</sup> toolbox, as it allowed us a more degree of freedom regarding the choice of projecting angles. We generated random angle scenarios, determined by their  $x$ ,  $y$ ,  $z$  positions in space.

For determining the optimal solution of the continuous problem, we used L-BFGS<sup>2</sup>, which we let run for 1500 iterations. An obvious question would be why 1500 or not more or less. We need to mention that we used the number of iterations in connection with another termination criteria,  $\|\nabla\psi(y^k)\| \leq 10^{-5}$ , however this never occurred in practice. And after extensive empirical trials, the mentioned number of iterations seemed appropriate for an optimal balance between computation time and quality of the reconstruction. Moreover, the reconstruction need not be perfect, as the following step of discrete minimization would reinforce object properties, "steering" thus the reconstruction towards the optimum value. During all test runs, we used  $\alpha = 18$ ,  $\lambda = 5$ .

#### 4.4. CONTINUOUS / DISCRETE INTERPLAY

Name	Gray val.	Image size	$r_k$	$J_{inter}$	$J_{self}$	# of detectors	# of proj.
Cube	2	$20^3$	$1.2e - 04$	47	1	8	6
Cube	4	$20^3$	$1.2e - 04$	47	1	8	4
Piston	2	$64^3$	$1.2e - 04$	10	1	25	9
Shepp-Logan	5	$25^3$	$1.2e - 04$	30	1	12	7

Table 4.3: Parameters used for the discrete optimization routine, that enable accurate reconstruction.

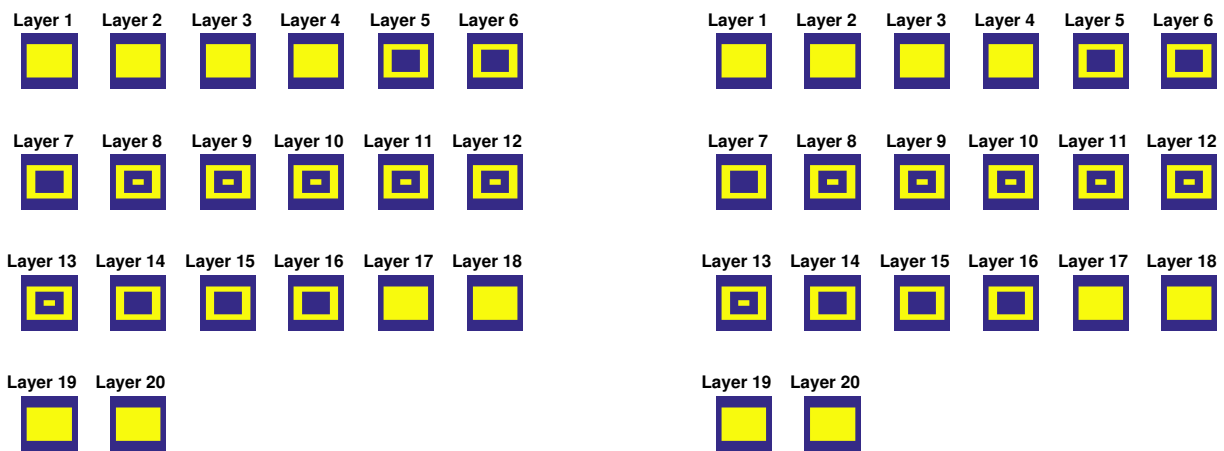


Figure 4.8: **Left:** Cross-sections of the original 3D cube with 2 gray levels.  $L_2$  norm of original image is  $l_2 = 54.1110$ . **Right:** Reconstruction with parameters mentioned in Table 4.3 to which we mention the  $L_2$  norm of the algorithm output, # of iterations and time required for reconstruction:  $L_2 = 54.1110$  (equal to the original), 9 iterations and 181 sec.

For the discrete problem, the number of detectors and the regularisation factor  $J_{inter}$  of each material is set constant, varying only on the image to be reconstructed, as shown in Table 4.3. The relative proportion  $J_{self}$  is constant over all images and is set to be 1, as we want each material to have equal chance of being reconstructed.

The alternating approach ends when the  $L_1$ -norm of the difference between the original image and the output of the discrete minimization problem is less than

<sup>1</sup><http://www2.compute.dtu.dk/~pcha/AIRtools/>

<sup>2</sup><http://www.di.ens.fr/~mschmidt/Software/minFunc.html>

$1e - 03$ .

During the experimental phase, we noticed that the end result of the reconstruction is in a one to one correspondence with the number of detectors used in the acquisition process, as well as with the orientation of the cameras. The higher the number of available detectors, the lower the required number of projection angles, given a certain limit, because it is obvious that one cannot reconstruct an image from only one view, for example. Likewise, a stagnation step in convergence is bound to occur at some camera orientation configurations. We currently have no explanation for this phenomenon. In this case, when the  $L_1$  error of the difference between the original image and the reconstructed image does not encounter any new change for the next couple of 5 iterations, we restart the process with a new camera orientation setting.

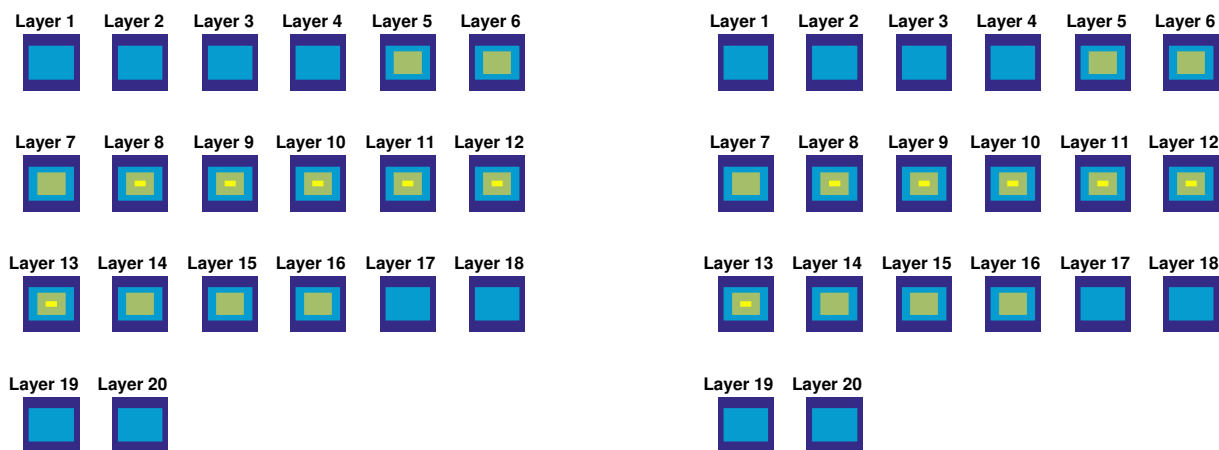


Figure 4.9: **Left:** Cross-sections of the 3D cube with 4 gray levels.  $L_2$  norm of this image is  $l_2 = 27.8089$ . **Right:** Reconstruction with parameters mentioned in Table 4.3 to which we mention the  $L_2$  norm of the algorithm output, # of iterations and time required for reconstruction:  $L_2 = 27.8089$  (equal to original), 3 iterations and 117 sec.

## 4.5 Conclusion

We presented three algorithmic approaches: entropic perturbation, quadratic perturbation, quadratic perturbation with continuous / discrete interplay to solve perturbed non-negatively constrained linear programs that arise in tomographic reconstruction problems of the form (4.2). While the perturbation enables to

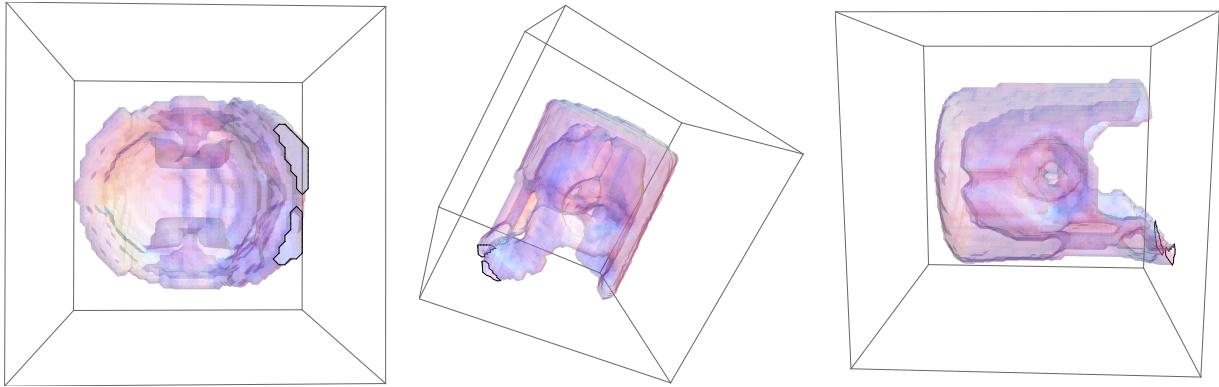


Figure 4.10: **Left:** Bottom view of the 3D piston with 2 gray levels.  $L_2$  norm of this image is  $l_2 = 149.1141$ . **Center and Right:** Tilted and side view of the piston reconstructed with parameters mentioned in Table 4.3 to which we mention the  $L_2$  norm of the algorithm output, # of iterations and time required for reconstruction:  $L_2 = 149.1141$  (equal to the original), 4 iterations and 2024.82 sec.

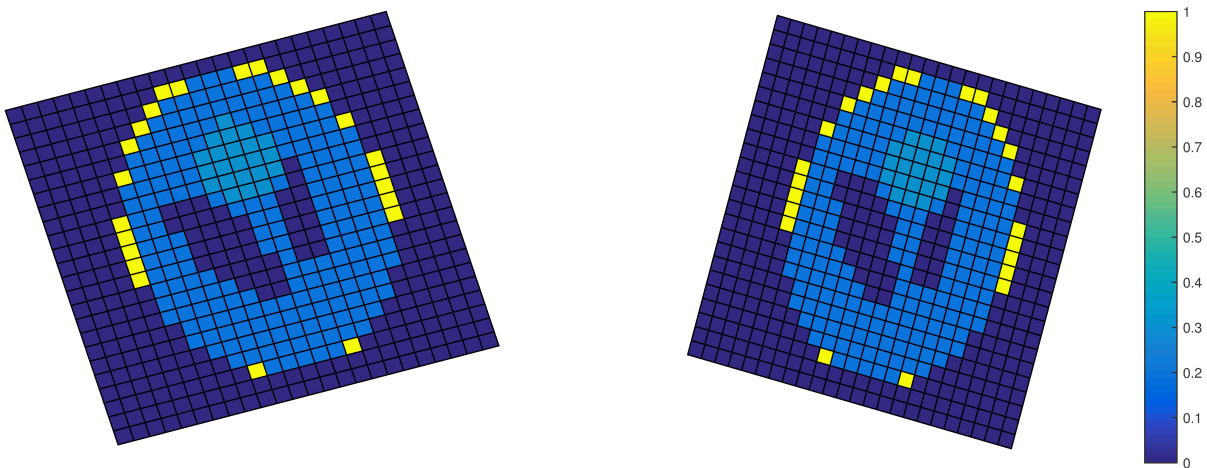


Figure 4.11: **Left:** Cross-section of the Shepp Logan phantom with 5 gray levels.  $L_2$  norm of this image is  $l_2 = 24.07$ . **Right:** Reconstruction with parameters mentioned in Table 4.3 to which we mention the  $L_2$  norm of the algorithm output, # of iterations and time required for reconstruction is  $l_2 = 24.0393$ , 2 iterations and 165.68 sec.

apply efficient sparse numerics, it does not compromise reconstruction accuracy. This is a significant step in view of the big data volumes of industrial scenarios.

## CHAPTER 4. RECOVERY ALGORITHMS: PERTURBED DUAL APPROACH

Moreover, we gave a brief comparison between widely known convex optimization routines and the approaches developed in this thesis. This chapter concludes with an alternating continuous / discrete minimization routine, which scales well with large problem sizes and higher number of gray levels, as seen in the empirical tests we have conducted.



---

---

# CHAPTER 5

---

## NEARLY ISOTROPIC PRIORS AND PROBLEM SPLITTING

In Chapters 3 and 4, we considered the problem of reconstructing images that have a sparse image gradient and indicate conditions on the number of measurements required for unique recovery. Empirically, in such cases, it also coincides with the solution to the corresponding convex optimisation problem. However, only horizontal and vertical differences were taken into account (TV-seminorm). Here we propose a different analysis operator, that better exploits the geometry of signal transitions and penalizes jumps along arbitrary (projecting) directions. While uniqueness conditions are subject to current research, we present below a dedicated numerical splitting scheme, along with few preliminary results.

### 5.1 Approach

We consider the constrained minimization problem

$$\min \gamma \sum_{s=1}^S \omega_s \|\nabla_{d_s} u_s\|_1 + \sum_{i=1}^p \|A_{d_i} v_{d_i} - b_{d_i}\|_2^2 \quad \text{s.t.} \quad \left\{ \begin{array}{l} u_r - u_t = 0; \\ v_i - u_s = 0; \\ i = 1, \dots, p; \\ (\forall) 1 \leq r < t \leq S; \\ (\forall) 1 \leq s \leq S. \end{array} \right. \quad (5.1)$$

with projection directions  $d_i, i \in [p]$ , associated weights  $\omega_s \geq 0$ , regularisation parameter  $\gamma > 0$  and  $S$  the number of derivative directions. The projection and derivative directions need not be identical nor equal in their number. For example, one might use 9 projection directions and only 4 derivative directions to analyse

the system. However, it might be the case that one angle from the projection direction is also an angle that is used for the derivative direction. Summing along directions  $d_i$  yields a corresponding block  $A_{d_i}$  in the projection matrix  $A$ .  $\nabla_{d_s}$ ,  $s \in [S]$  are linear operators approximating the directional derivative along  $d_s$ . We detail the case of positive weights  $\omega_s = 1$ , for arbitrary numbers of derivative and projection directions and we replace the projection directions  $d_i$  by indices  $i$  for ease of writing.

The constraints imposed on the objective function state that the split variables used in the derivative directions should resemble each other and correspondingly, to the considered projection directions. The result of the optimization problem leads to identical images  $u_i, v_j$ .

A similar problem to the one we are analysing is presented in [110], which considers the Potts model instead of the  $\ell_1$  minimization. The authors show convergence of their method, however proving global optimality of the solution is an open problem. With our approach, we have the guarantees that the objective function is convex, thus a global solution is bound to exist.

We begin analysing our problem by forming the augmented Lagrangian with multipliers  $\lambda_{i,s}, \rho_{r,t}$  and prox-parameters  $\mu, \nu$ :

$$L = \gamma \sum_{s=1}^S \left( \omega_s \|\nabla_{d_s} u_s\|_1 + \sum_{i=1}^p \langle \lambda_{i,s}, v_i - u_s \rangle + \frac{\mu}{2} \sum_{i=1}^p \|v_i - u_s\|_2^2 \right) + \sum_{i=1}^p \|A_i v_i - b_i\|_2^2 + \langle \rho_{r,t}, u_r - u_t \rangle + \frac{\nu}{2} \|u_r - u_t\|_2^2.$$

Writing it in a more convenient form, we have

$$L = \gamma \sum_{s=1}^S \left( \omega_s \|\nabla_{d_s} u_s\|_1 + \frac{\mu}{2} \sum_{i=1}^p \|v_i - u_s + \frac{\lambda_{i,s}}{\mu}\|_2^2 - \frac{\mu}{2} \sum_{i=1}^p \left\| \frac{\lambda_{i,s}}{\mu} \right\|_2^2 \right) + \sum_{i=1}^p \|A_i v_i - b_i\|_2^2 + \frac{\nu}{2} \sum_{1 \leq r < t \leq S} \left( \|u_r - u_t + \frac{\rho_{r,t}}{\nu}\|_2^2 - \left\| \frac{\rho_{r,t}}{\nu} \right\|_2^2 \right).$$

In the following lines, we introduce a lemma from [110] that will ease the minimization of the Lagrangian with respect to the split variables  $u_1, u_2, \dots$  and the projection  $v_1, v_2, \dots$ .

**Lemma 5.1.1** ([110], Lemma 2.1). *For  $a, b_1, \dots, b_N \in \mathbb{R}$  and  $x_1, \dots, x_N > 0$ , we have that*

$$\sum_i x_i (a - b_i)^2 = \left( \sum_i x_i \right) \left( a - \frac{\sum_i b_i x_i}{\sum_i x_i} \right)^2 + C$$

where  $C \in \mathbb{R}$  is a constant that does not depend on  $a$ .

*Proof.* We calculate

$$\begin{aligned}
 \sum_i x_i (a - b_i)^2 &= a^2 \left( \sum_i x_i \right) - 2a \left( \sum_i b_i x_i \right) + \sum_i b_i^2 x_i \\
 &= \left( \sum_i x_i \right) \left( a^2 - 2a \frac{\sum_i b_i x_i}{\sum_i x_i} + \frac{\sum_i b_i^2 x_i}{\sum_i x_i} \right) \\
 &= \left( \sum_i x_i \right) \left( a^2 - 2a \frac{\sum_i b_i x_i}{\sum_i x_i} + \left( \frac{\sum_i b_i x_i}{\sum_i x_i} \right)^2 - \left( \frac{\sum_i b_i x_i}{\sum_i x_i} \right)^2 - \frac{\sum_i b_i^2 x_i}{\sum_i x_i} \right) \\
 &= \left( \sum_i x_i \right) \left( \left( a - \frac{\sum_i b_i x_i}{\sum_i x_i} \right)^2 - \left( \frac{\sum_i b_i x_i}{\sum_i x_i} \right)^2 - \frac{\sum_i b_i^2 x_i}{\sum_i x_i} \right)
 \end{aligned}$$

□

The result depicts the ones stated in the lemma, as the last two terms are independent of  $a$ .

Using Lemma 5.1.1, the restricted form of the augmented Lagrangian reads:

$$\begin{aligned}
 L &= \gamma \sum_{s=1}^S \left( \omega_s \|\nabla_{d_s} u_s\|_1 + \frac{\mu}{2} \sum_{i=1}^p \left\| v_i - u_s + \frac{\lambda_{i,s}}{\mu} \right\|_2^2 \right) + \\
 &\quad + \frac{\nu}{2} \sum_{1 \leq r < t \leq S} \left\| u_r - u_t + \frac{\rho_{r,t}}{\nu} \right\|_2^2 + \sum_{i=1}^p \|A_i v_i - b_i\|_2^2. \quad (5.2)
 \end{aligned}$$

For solving the Lagrangian (5.2) we apply ADMM, briefly presented in Sect. 2.1.1.4

### 5.1.1 Minimizing gradient directions

We consider the minimization of the restricted augmented Lagrangian (5.2) with respect to the split variables  $u_s$ :

$$\begin{aligned}
 \operatorname{argmin}_{u_s} L &= \operatorname{argmin}_{u_s} \gamma \omega_s \|\nabla_{d_s} u_s\|_1 + \\
 &\quad + \frac{\mu}{2} \sum_{i=1}^p \left\| v_i - u_s + \frac{\lambda_{i,s}}{\mu} \right\|_2^2 + \frac{\nu}{2} \sum_{1 \leq r < s} \left\| u_r - u_s + \frac{\rho_{r,s}}{\nu} \right\|_2^2 + \frac{\nu}{2} \sum_{s < t \leq S} \left\| u_s - u_t + \frac{\rho_{s,t}}{\nu} \right\|_2^2.
 \end{aligned}$$

Making use of Lemma 5.1.1, the minimization now reads

$$\operatorname{argmin}_{u_s} L = \operatorname{argmin}_{u_s} \frac{2\alpha\gamma_s}{p\mu_k + \nu_k(S-1)} \|\nabla_{d_s} u_s\|_1 + \|u_s - w_s\|_2^2,$$

$$\text{where } w_s = \frac{\mu_k \sum_{i=1}^p v_i + \sum_{i=1}^p \lambda_i + \sum_{1 \leq r < s} (\nu_k u_r + \rho_{r,s}) + \sum_{s < t \leq S} (\nu_k u_t - \rho_{s,t})}{p\mu_k + \nu_k(S-1)}$$

### 5.1.2 Minimizing projection directions

We now turn our attention to the minimization of the restricted augmented Lagrangian (5.2) with respect to the projection blocks  $v_i$ :

$$\operatorname{argmin}_{v_i} L = \operatorname{argmin}_{v_i} \sum_{i=1}^p \|A_i v_i - b_i\|_2^2 + \sum_{s=1}^S \sum_{i=1}^p \left( \frac{\mu}{2} \|v_i - u_s + \frac{\lambda_{is}}{\mu}\|_2^2 \right). \quad (5.3)$$

Using Lemma 5.1.1, this reads:

$$\operatorname{argmin}_{v_i} \|A_i v_i - b_i\|_2^2 + \frac{\mu S}{2} \|v_i - \frac{1}{S} \sum_{s=1}^S (u_s - \frac{\lambda_{i,s}}{\mu})\|_2^2.$$

Lastly, we update the Lagrangian parameters by a gradient descent approach:

$$\begin{aligned} \lambda_{i,s}^{k+1} &= \lambda_{i,s}^k + \mu_k (v_i^{k+1} - u_s^{k+1}); \\ \rho_{r,t}^{k+1} &= \rho_{r,t}^k + \nu_k (u_r^{k+1} - u_t^{k+1}), \forall 1 \leq r < t \leq S. \end{aligned}$$

All of the above are summarized in Alg. 6.

---

#### Algorithm 6 ADMM with proximal operator splitting

---

**Require:**  $\nu_k = 0, \mu_k = 10^{-6} k^\tau, \tau = 2.01, u_i, \lambda_{i,s}, v = 0, i \in [p], k = \text{iteration counter}$

**Minimize for each *gradient* direction {1}**

$$u_1^{k+1} = \operatorname{argmin}_{u_1} \frac{2\alpha\gamma_1}{p\mu_k + \nu_k(S-1)} \|\nabla_{d_1} u_1\|_1 + \|u_1 - w_1^k\|_2^2$$

$\vdots$

$$u_S^{k+1} = \operatorname{argmin}_{u_S} \frac{2\alpha\gamma_S}{p\mu_k + \nu_k(S-1)} \|\nabla_{d_S} u_S\|_1 + \|u_S - w_S^k\|_2^2$$

**Minimize for each *projection* direction {2}**

$$v_1^{k+1} = \operatorname{argmin}_{v_1} \|A_1 v_1 - b_1\|_2^2 + \frac{\mu_k S}{2} \|v_1 - \frac{1}{S} \sum_{s=1}^S (u_s - \frac{\lambda_{1,s}}{\mu_k})\|_2^2$$

$\vdots$

$$v_p^{k+1} = \operatorname{argmin}_{v_p} \|A_p v_p - b_p\|_2^2 + \frac{\mu_k S}{2} \|v_p - \frac{1}{S} \sum_{s=1}^S (u_s - \frac{\lambda_{p,s}}{\mu_k})\|_2^2$$

**Update Lagrangian parameters**

$$\lambda_{i,s}^{k+1} = \lambda_{i,s}^k + \mu_k (v_i^{k+1} - u_s^{k+1}), \quad i = 1, 2, \dots, p; \quad s = 1, 2, \dots, S$$

$$\rho^{k+1} = \rho^k + \nu_k (u_i^{k+1} - u_j^{k+1}), \quad \forall 1 \leq i < j \leq S.$$

$$\text{where } w_s = \frac{\mu_k \sum_{i=1}^p v_i + \sum_{i=1}^p \lambda_i + \sum_{1 \leq r < s} (\nu_k u_r + \rho_{r,s}) + \sum_{s < t \leq S} (\nu_k u_t - \rho_{s,t})}{p\mu_k + \nu_k(S-1)}.$$


---

## 5.2 Numerical Experiments

We tested our approach on two synthetic  $50 \times 50$  images and the well known Shepp-Logan phantom image, of the same size. The gradient direction minimization problems  $u_1, \dots, u_s$ ,  $s = 1, \dots, S$ , are solved by using 1D TV proximal operators. We rely on the work introduced in Barbero et. al. [3], where they present a new approach of computing 1D proximal operators, referred to as "Taut String" method (Fig. 5.1), whereas for the projection direction case, a series of

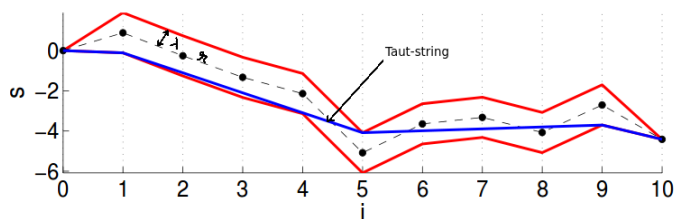


Figure 5.1: Illustration of taut-string method. The principle behind it is to determine the minimum length polyline (taut-string) crossing a tube of height  $\lambda$  with center the cumulative sum  $r$  and with fixed points  $(s_0, s_n)$ . The blue line in the picture above represents the taut string solution. For more details, we refer the reader to [3].

simple unconstrained least squares problems solved using L-BFGS<sup>1</sup>, returns the end result.

Conveniently enough, the recovery algorithm scales up to large problem sizes and can be adequately implemented on various architectures, i.e. parallelized, due to its iterative nature.

<sup>1</sup><http://www.di.ens.fr/~mschmidt/Software/minFunc.html>

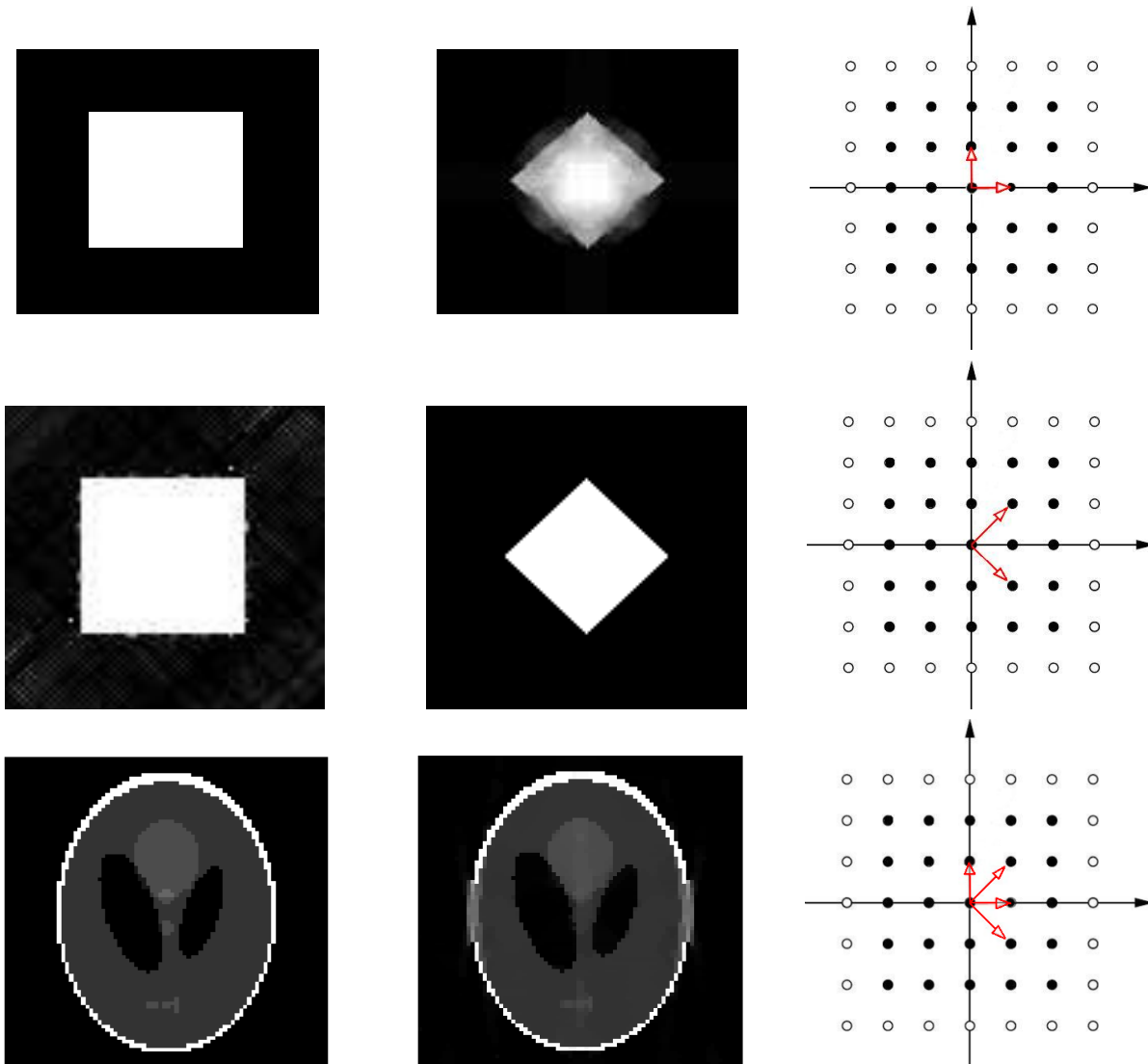


Figure 5.2: Structure aware regularization: **First row:** Reconstructed images from 4 projections using only horizontal and vertical directional derivatives, see image top right. **Second row:** Reconstruction from 4 projections using directional derivatives along diagonals orientated at  $45^\circ$  and  $-45^\circ$ , see image bottom right. Our general analysis operator penalises jumps along all  $p$  projection directions. **Third row:** Shepp Logan reconstructed from 10 equiangular projections chosen over a 360 degrees range, using vertical and diagonal gradient directions.

---

---

# CHAPTER 6

---

## CONCLUSION

Work comprised in this thesis hopes to have improved and shed a new perspective over the problem of image reconstruction from reduced sparse tomographic data in industrial applications. By entailing gradient priors subject to non-negativity constraints we raised the difficulty of the problem at hand (e.g. compared to typical  $\ell_1$  minimization, basis pursuit), but on the other side we are closer in detailing specific object properties.

By making use of *cosparsity*, an alternative viewpoint to the notion of *sparsity*, and modelling the tomographic acquisition matrix with properties of expander graphs, we were able to devise in Chapter 3 theoretical bounds relating objects' cosparsity and number of measurements required for accurate reconstruction of objects in 2D and 3D. We backed-up our theoretical results with extensive empirical tests, through the display of phase transitions obtained from solving the total variation problem subject to equality and non-negativity constraints as a linear program with the help of the commercially available software, MOSEK. These bounds represent a novelty point in our work and in this research domain.

A closer look in solving large-scale problems, volumes, was given in Chapter 4. We approached the reconstruction problem via entropic and quadratic perturbations of the linear program studied in Chapter 3 and notions of functional duality from convex analysis. Conclusive for this section is that perturbation brings additional information to the reconstruction problem, although the main drawback lies in the dependency of parameters, that need to be fine tuned. This is an open problem that still needs to be addressed. Along the lines of perturbation, we turned our view towards a continuous / discrete approach where we incorporate quantization levels. That is, in every step we refine the continuous reconstruction by an instance of graph cuts, representing the discrete minimization step, where we know beforehand the number of materials we have to reconstruct. Graph cuts has shown to be reliable and to return promising results in a multitude of

---

applications regarding image segmentation.

Lastly, in Chapter 5 we briefly exploited the spatial structure of sparsity. Considering the gradient and projection directions individually and not as a conglomerate, we have illustrated that this approach brings along extra image information if taken into consideration as "stand-alone" minimization problems.

Tomographic image reconstruction is still a vast research field and by no means, did the content of this thesis solve one specific problem entirely. There are still open problems that need to be addressed, among which we mention:

- Clarify quantitatively the scale factor mentioned in Chapter 3 and its origins.
- Conduct a probabilistic analysis as in the work of [95]), for the present scenarios. The expectation is that the refinement of a probabilistic version of the cosparsity model, in connection with distributions of cosupports learned from relevant collections of signals, may have an impact both theoretically and practically beyond aspects of limited-angle tomography.
- Deviation bounds for the average case analysis regarding the  $\ell_0/\ell_1$  equivalence of the analysis model, are still lacking.
- Devise approaches that are robust against high levels of noise.

---

## BIBLIOGRAPHY

- [1] D. Amelunxen, M. Lotz, M. B. McCoy, and J. A. Tropp. Living on the edge: Phase Transitions in Convex Programs with Random Data. *arxiv preprint: <http://arxiv.org/pdf/1303.6672v2.pdf>*, 2014.
- [2] R. Baraniuk. Compressive Sensing. *IEEE Signal Processing Magazine*, 24(4):118–121, 2007.
- [3] A. Barbero and S. Sra. Modular Proximal Optimization for Multidimensional Total-Variation Regularization. *Preprint at <http://arxiv.org/abs/1411.0589>*.
- [4] K.J. Batenburg. An evolutionary algorithm for discrete tomography. *Discrete Applied Mathematics*, 151:36–54, 2006.
- [5] K.J. Batenburg. A network flow algorithm for reconstructing binary images from discrete X-rays. *Journal of Mathematical Imaging and Vision*, 27(2):175–191, 2007.
- [6] K.J. Batenburg and J. Sijbers. DART: A practical reconstruction algorithm for discrete tomography. *IEEE Transactions on Image Processing*, 20:2542–2553, 2011.
- [7] A. Beck and M. Teboulle. A Fast Iterative Shrinkage-Thresholding Algorithm for Linear Inverse Problems. *Journal of Imaging Sciences*, 2(1):183–202, 2009.
- [8] M. Bergounioux and A. Srour. A relaxation method for smooth tomographic reconstruction of binary axially symmetric objects. *Pacific Journal of Optimization*, 5:39–51, 2009.

- 
- [9] F. Bleichrodt, F. Tabak, and K.J. Batenburg. SDART:an algorithm for discrete tomography from noisy projections. *Journal of Computer Vision and Image Understanding*, 129:63–74, 2014.
- [10] B. Bollobás and I. Leader. Edge-Isoperimetric Inequalities in the Grid. *Combinatorica*, 11(4):299–314, 1991.
- [11] J. F. Bonnans, Gilbert, C. Lemaréchal, and C. Sagastizábal. *Numerical Optimization – Theoretical and Practical Aspects*. Springer Verlag, Berlin, 2006.
- [12] S. Boyd and L. Vandenberghe. *Convex Optimization*. Cambridge University Press, 2004.
- [13] Stephen Boyd, Neal Parikh, Eric Chu, Borja Peleato, and Jonathan Eckstein. Distributed Optimization and Statistical Learning via the Alternating Direction Method of Multipliers. *Foundations and Trends in Machine Learning*, 3(1):1–122, 2011.
- [14] Y. Boykov and V. Kolmogorov. An Experimental Comparison of Min-Cut/Max-Flow Algorithms for Energy Minimization in Vision. *IEEE Transactions on Pattern Analysis and Machine Intelligence*, 26:1124–1137, 2004.
- [15] Y. Boykov, O. Veksler, and R. Zabih. Fast Approximate Energy Minimization via Graph Cuts. *IEEE Transactions on Pattern Analysis and Machine Intelligence*, 23:1222–1239, 2001.
- [16] E. J. Candès. Compressive Sampling. In *Int. Congress of Math.*, volume 3, Madrid, Spain, 2006.
- [17] E. J. Candès. The Restricted Isometry Property and its Implications for Compressed Sensing. *Comptes Rendus Mathématique*, 346(9-10):589–592, 2008.
- [18] E. J. Candès, Y. C. Eldar, and D. Deanna Needell. Compressed Sensing with Coherent and Redundant Dictionaries. *Applied and Computational Harmonic Analysis*, 31(1):59–73, 2010.
- [19] E. J. Candès and B. Recht. Simple Bounds for Low-complexity Model Reconstruction. *CoRR*, abs/1106.1474, 2011.
- [20] E. J. Candès, J. Romberg, and T. Tao. Robust Uncertainty Principles: Exact Signal Reconstruction from Highly Incomplete Frequency Information. *IEEE Transactions on Information Theory*, 52(2):489–509, February 2006.

- [21] E. J. Candès, J. K. Romberg, and T. Tao. Stable Signal Recovery from Incomplete and Inaccurate Measurements. *Communications on Pure and Applied Mathematics*, 59(8):1207–1223, 2006.
- [22] E. J. Candès and M. Wakin. An Introduction to Compressive Sampling. *IEEE Signal Processing Magazine*, 25(2):21–30, 2008.
- [23] S. Carmignato. Computed Tomography as a Promising Solution for Industrial Quality Control and Inspection of Castings. *Metallurgical Science and Technology*, 30-1:5–14, 2012.
- [24] Y. Censor, D.M. Altschuler, and D.W. Powlis. On the use of Cimmino’s simultaneous projections method for computing a solution of the inverse problem in radiation therapy treatment planning. *Journal of Inverse problems*, 4:607–623, 1988.
- [25] Y. Censor, T. Elfving, T.G Herman, and T. Nikazad. On Diagonally Relaxed Orthogonal Projection Methods. *Journal of Scientific Computing*, 30:473–504, 2008.
- [26] Y. Censor, D. Gordon, and R. Gordon. Component averaging: An efficient iterative parallel algorithm for large and sparse unstructured problems. *Journal of Parallel Computing*, 27:777–808, 2001.
- [27] Y. Censor and G. T. Herman. Block-Iterative Algorithms with Underrelaxed Bregman Projections. 2002.
- [28] A. Chambolle, R.A. DeVore, N.Y Lee, and B.J. Lucier. Nonlinear wavelet image processing: Variational problems, compression and noise removal through wavelet shrinkage. *IEEE Transactions on Image Processing*, 7:319–335, 1998.
- [29] A. Chambolle and T. Pock. A First-Order Primal-Dual Algorithm for Convex Problems with Applications to Imaging. *Journal of Mathematical Imaging and Vision*, 40:120–145, 2011.
- [30] V. Chandar. A Negative Result Concerning Explicit Matrices with the Restricted Isometry Property. 2008. Preprint [http://dsp.rice.edu/files/cs/Venkat\\_CS.pdf](http://dsp.rice.edu/files/cs/Venkat_CS.pdf).
- [31] R. Cominetti and J.P. Dussault. Stable Exponential-Penalty Algorithm with Superlinear Convergence. *J. Optim. Theory Appl.*, 83(2):285–309, 1994.
- [32] R. Cominetti and J. San Martin. Asymptotic analysis of the exponential penalty trajectory in linear programming. *Math. Progr.*, 67:169–187, 1994.

- 
- [33] I. Daubechies, M. Defrise, and C. de Mol. An iterative thresholding algorithm for linear inverse problems with a sparsity constraint. *Communications on Pure and Applied Mathematics*, 57:1413–1457, 2004.
- [34] A. Denițiu, S. Petra, C. Schnörr, and C. Schnörr. Phase Transitions and Cospase Tomographic Recovery of Compound Solid Bodies from Few Projections. *ArXiv e-prints*, November 2013.
- [35] D. Donoho. Compressed Sensing. Technical report, Department of Statistics, Stanford Univerisity, 2004.
- [36] D. Donoho. Neighborly Polytopes and Sparse Solutions of Underdetermined Linear Equations. Technical report, 2005.
- [37] D. Donoho. Compressed Sensing. *IEEE Transactions on Information Theory*, 52:1289–1306, 2006.
- [38] D. Donoho and M. Elad. Optimally sparse representation in general (non-orthogonal) dictionaries via l1 minimization. In *Proceedings of the National Academy of Sciences*, volume 100, pages 2197–2202, 2003.
- [39] D. Donoho and J. Tanner. Sparse nonnegative solutions of underdetermined linear equations by linear programming. In *Proceedings of the National Academy of Sciences*, pages 9446 – 9451, 2005.
- [40] D. Donoho and J. Tanner. Observed universality of phase transitions in high-dimensional geometry, with implications for modern data analysis and signal processing. *Philosophical Transactions of the Royal Society A: Mathematical, Physical and Engineering Sciences*, 367(1906):4273–4293, 2009.
- [41] D. L. Donoho and J. Tanner. Counting the Faces of Randomly-Projected Hypercubes and Orthants, with Applications. *Discrete & Computational Geometry*, 43(3):522–541, 2010.
- [42] D.L. Donoho and J. Tanner. Counting Faces of Randomly Projected Polytopes when the Projection Radically Lowers Dimension. *Journal of American Mathematical Society*, 22:1–53, 2009.
- [43] J. Douglas and H.H. Rachford. On the numerical solution of heat conduction problems in two and three space variables. *Transactions of the AMS* 82, pages 421–439, 1956.
- [44] M. Elad. Sparse Representations Are Most Likely to Be the Sparsest Possible. *EURASIP J. Adv. Sig. Proc.*, 2006:1–12, 2006.

- [45] M. Elad, P. Milanfar, and R. Rubinstein. Analysis versus synthesis in signal priors. *Inverse Problems*, 23:947–968, 2007.
- [46] H. Erdoğan and J.A. Fessler. Ordered subsets algorithms for transmission tomography. *Physics in Medicine and Biology*, 44:2835–2851, 1999.
- [47] J.R. Eriksson. A note on solution of large sparse maximum entropy problems with linear equality constraints. *Math. Programm.*, 18:146154, 1980.
- [48] S. Erlander. Entropy in linear programs. *Math. Programm.*, 21:137–151, 1981.
- [49] S. C. Fang and H. S. J. Tsao. Linear programming with entropic perturbation. *Math. Meth. of OR*, 37(2):171–186, 1993.
- [50] S. C. Fang and H. S. J. Tsao. On the entropic perturbation and exponential penalty methods for linear programming. *J. Optim. Theory Appl.*, 89:461–466, 1996.
- [51] M. C. Ferris and O. L. Mangasarian. Finite perturbation of convex programs. *Appl. Math. Optim*, 23:263–273, 1991.
- [52] M.A.T. Figueiredo and R.D. Nowak. An EM algorithm for wavelet-based image restoration. *IEEE Transactions on Image Processing*, 12:906–916, 2003.
- [53] L.R. Ford and D.R. Fulkerson. *Flows in Networks*. Princeton University Press, 1974.
- [54] Simon Foucart and Holger Rauhut. *A Mathematical Introduction to Compressive Sensing*. Birkhäuser Basel, 2013.
- [55] Michael P. Friedlander and Paul Tseng. Exact Regularization of Convex Programs. *SIAM J. on Optimization*, 18(4):1326–1350, November 2007.
- [56] R.J. Gardner and P. Gritzmann. Discrete Tomography: Determination of Finite Sets by X-Rays. *Transactions of the American Mathematical Society*, 349(6):2271–2295, 1997.
- [57] B. Goris, W. Van den Broek, K.J. Batenburg, H.H. Mezerji, and S. Bals. Electron Tomography Based on a Total Variation Minimization Reconstruction Techniques. *Ultramicroscopy*, 113:120–130, 2012.
- [58] C. Grünzweig, D. Mannes, A. Kaestner, F. Schmid, V. Vontobel, J. Hovind, S. Hartmann, S. Peetermans, and E. Lehmann. Progress in Industrial Applications using Modern Neutron Imaging Techniques. *Physics Procedia*, 43:231–242, 2013.

- 
- [59] Yin W. Hale, E. and Y. Zhang. A Fixed-Point Continuation Method for  $\ell_1$ -Regularized Minimization with Applications to Compressed Sensing. Technical Report TR07-07, Rice University, Houston, Texas, 2007.
- [60] P. C. Hansen and M. Saxild-Hansen. AIR Tools - A MATLAB Package of Algebraic Iterative Reconstruction Methods. *Journal of Computation and Applied Mathematics*, 236:2167–2178, 2012.
- [61] B. He and X. Yuan. On convergence rate of the Douglas-rachford operator splitting method.
- [62] G. T. Herman and R. Davidi. Image Reconstruction from a Small Number of Projections. *Inverse Problems*, 24(4):45011–45028, 2008.
- [63] G. T. Herman and A. Kuba. *Discrete Tomography: Foundations, Algorithms and Applications*. Birkhäuser, 1999.
- [64] S. Jafarpour, M. F. Duarte, and A. R. Calderbank. Beyond Worst-Case Reconstruction in Deterministic Compressed Sensing. In *ISIT*, pages 1852–1856. IEEE, 2012.
- [65] T. L. Jensen, J. H. Jørgensen, P. C. Hansen, and S. H. Jensen. Implementation of an Optimal First-Order Method for Strongly Convex Total Variation Regularization. *BIT Numerical Mathematics*, 52:329–356, 2012.
- [66] J. H. Jorgensen, C. Kruschel, and D. Lorenz. Testable uniqueness conditions for empirical assessment of undersampling levels in total variation-regularized X-ray CT. *Inverse Problems in Science and Engineering*, 8, 2014.
- [67] J. H. Jorgensen, E. Y. Sidky, P. C. Hansen, and P. Xiaochuan. Quantitative Study of Undersampled Recoverability for Sparse Images in Computed Tomography. <http://arxiv.org/abs/1211.5658v1>, Nov 2012. submitted SIAM Journal on Scientific Computing.
- [68] J. H. Jorgensen, E. Y. Sidky, P. C. Hansen, and P. Xiaochuan. Quantifying Admissible Undersampling for Sparsity-Exploiting Iterative Image Reconstruction in X-Ray CT. *IEEE Transactions on Medical Imaging*, 32(2):460–473, 2013.
- [69] J. S. Jorgensen, Y. Emil Sidky, Per Christiansen Hansen, and Xiaochuan Pan. Empirical average-case relation between undersampling and sparsity in X-ray CT. *Inverse Problems and Imaging*, 9(2):431–446, 2015.

- [70] J. S. Jrgensen and E. Y. Sidky. How Little Data Is Enough? Phase-Diagram Analysis of sparsity-regularized x-ray computed tomography.. *Philosophical transactions. Series A, Mathematical, physical, and engineering sciences* 373.2043 (2015): 20140387. PMC. Web. 23 Oct. 2015., 373.2043, 2015.
- [71] Maryia Kabanava and Holger Rauhut. Cosparsity in Compressive Sensing.
- [72] Willi A. Kalender. *Computed tomography: fundamentals, system technology, image quality, applications*. Publicis -MCD-Verl., 2000.
- [73] J.H. Kappes, S. Petra, C. Schnörr, and M. Zisler. TomoGC: Binary Tomography by Constrained Graph Cuts. In *In proceedings GCPR*, 2015.
- [74] M.E Kazemi and S.N. Nediakov. An empirical study of algebraic-reconstruction techniques. *Computational Vision and Medical Image Processing IV*, 2014.
- [75] M.A. Khajehnejad, A.G. Dimakis, W. Xu, and B. Hassibi. Sparse recovery of nonnegative signals with minimal expansion. *IEEE Transactions on Signal Processing*, 59:196–208, 2011.
- [76] V. Kolmogorov and R. Zabih. What Energy Functions Can Be Minimized via Graph Cuts? *IEEE Transactions on Pattern Analysis and Machine Intelligence*, 26:147–159, 2004.
- [77] L. Landweber. An Iteration Formula for Fredholm Integral Equations of the First Kind. *American Journal of Mathematics*, 73:615–624, 1951.
- [78] K. Lange and R. Carson. EM reconstruction algorithms for emission and transmission tomography. *Journal of Computer Assisted Tomography*, 8(2):306–316, 1984.
- [79] F. Lim and V. M. Stojanovic. On U-Statistics and Compressed Sensing I: Non-Asymptotic Average-Case Analysis. *IEEE Transactions on Signal Processing*, 61(10):2473–2485, 2013.
- [80] F. Lim and V. M. Stojanovic. On U-Statistics and Compressed Sensing II: Non-Asymptotic Worst-Case Analysis. *IEEE Transactions on Signal Processing*, 61(10):2486–2497, 2013.
- [81] P.L. Lions and B. Mercier. Splitting algorithms for the sum of two nonlinear operators. *SIAM J. on Numerical Analysis*, 16(6):964–979, 1979.
- [82] Y. M. Lu and M. N. Do. A Theory for Sampling Signals From a Union of Subspaces. *IEEE Transactions on Signal Processing*, 56(6):2334–2345, 2008.

- 
- [83] S. Maeda, W. Fukuda, A. Kanemura, and S. Ishii. Maximum a posterior X-ray computed tomography using graph cuts. *Journal of Physics: Conference Series*, 233:12–23, 2010.
- [84] O. L. Mangasarian. Uniqueness of Solution in Linear Programming. *Linear Algebra and its Applications*, 25(0):151–162, 1979.
- [85] O. L. Mangasarian and B. Benjamin Recht. Probability of Unique Integer Solution to a System of Linear Equations. *European Journal of Operational Research*, 214(1):27–30, 2011.
- [86] M. Minoux. *Mathematical Programming: Theory and Algorithms*. Wiley, 1986.
- [87] S. Nam, M. E. Davies, M. Elad, and R. Gribonval. The Cospase Analysis Model and Algorithms. *Applied and Computational Harmonic Analysis*, 34(1):30–56, 2013. Preprint available on arXiv since 24 Jun 2011.
- [88] F. Natterer. *The Mathematics of Computerized Tomography*. SIAM, 2001.
- [89] F. Natterer and F. Wübbeling. *Mathematical Methods in Image Reconstruction*. SIAM, 2001.
- [90] D. Needell and R. Ward. Near-Optimal Compressed Sensing Guarantees for Total Variation Minimization. *IEEE Transactions on Image Processing*, 22:3941–3949, October 2013.
- [91] D. Needell and R. Ward. Stable Image Reconstruction Using Total Variation Minimization. *SIAM Journal on Imaging Sciences*, 6(2):1035–1058, 2013.
- [92] V.Y. Panin, G.L. Zeng, and G.T. Gullberg. Total Variation Regulated EM Algorithm. *IEEE Transactions on Nuclear Science*, 46(6):2202–2210, 1999.
- [93] V. M Patel, R. Maleh, Gilbert A. C., and Chellappa R. Gradient-Based Image Recovery Methods From Incomplete Fourier Measurements. *IEEE Transactions on Image Processing*, 21(1):94–105, 2012.
- [94] S. Petra and C. Schnörr. TomoPIV meets Compressed Sensing. *Pure Mathematics and Applications*, 20(1-2):49–76, 2009.
- [95] S. Petra and C. Schnörr. Average Case Recovery Analysis of Tomographic Compressive Sensing. *Linear Algebra and its Applications*, 441:168–198, 2014. Special Issue on Sparse Approximate Solution of Linear Systems.

- [96] S. Petra, C. Schnörr, and A. Schröder. Critical Parameter Values and Reconstruction Properties of Discrete Tomography: Application to Experimental Fluid Dynamics. *Fundamenta Informaticae*, 125:285–312, 2013.
- [97] S. Petra, A. Schröder, and C. Schnörr. 3D Tomography from Few Projections in Experimental Fluid Mechanics. In W. Nitsche and C. Dobriloff, editors, *Imaging Measurement Methods for Flow Analysis*, volume 106 of *Notes on Numerical Fluid Mechanics and Multidisciplinary Design*, pages 63–72. Springer, 2009.
- [98] H. Raguet, J. Fadili, and G. Peyré. A Generalized Forward-Backward Splitting. April 2012. Preprint arXiv:1108.4404.
- [99] R.T. Rockafellar and R. J.-B. Wets. *Variational Analysis*. Springer, 2nd edition, 2009.
- [100] L.I. Rudin, S. Osher, and E. Fatemi. "n"online total variation based noise removal algorithms. *Physica D. Nonlinear Phenomena*, 60:259–268, 1992.
- [101] O. Scherzer, editor. *Handbook of Mathematical Methods in Imaging*. Springer, 2011.
- [102] T. Schüle, C. Schnörr, S. Weber, and J. Hornegger. Discrete tomography by convex-concave regularization and D.C. programming. *Discrete Applied Mathematics*, 151:229–243, 2005.
- [103] Hoory Shlomo, Nathan Linial, and Avi Wigderson. Expander graphs and their applications. *Bulleting of the American Mathematical Society*, 43(4):439–561, 2006.
- [104] E. Y. Sidky, J. Joergensen, and X. Pan. Convex optimization problem prototyping for image reconstruction in computed tomography with the chambolle-pock algorithm. <http://arxiv.org/pdf/1111.5632.pdf>, 2012.
- [105] E. Y. Sidky and X. Pan. Image Reconstruction in Circular Cone-Beam Computed Tomography by Constrained, Total-Variation Minimization. *Physics in Medicine and Biology*, 53(17):47–77, 2008.
- [106] E.Y. Sidky, M.A. Anastasio, and X. Pan. Image reconstruction exploiting object sparsity in boundary - enhanced X-ray phase-contrast tomography. *Optics Express*, 18(10):10404–10422, 2010.
- [107] M. Slawski and M. Hein. Sparse Recovery by Thresholded Non-Negative Least Squares. In J. Shawe-Taylor, R.S. Zemel, P. Bartlett, F.C.N. Pereira, and K.Q. Weinberger, editors, *Advances in Neural Information Processing Systems 24*, pages 1926–1934. 2011.

- 
- [108] SPIE, editor. *Filter design for filtered back-projection guided by interpolation method*, volume 4684 of *Medical Imaging*, 2002.
- [109] M. Stojnic. Recovery thresholds for  $\ell_1$  optimization in binary compressed sensing. In *ISIT*, pages 1593–1597, 2010.
- [110] A. Friel, J. Storath, M. Weinmann and M. Unser. Joint Image Reconstruction and Segmentation using the Potts Model. *To appear in Inverse Problems*, Preprint at <http://arxiv.org/abs/1405.5850>.
- [111] D. G. Tian and Q. Fei. An extension of the entropic perturbation method of linear programming. *Math. Meth. of OR*, 50(1):17–25, 1999.
- [112] P. Tseng. Convergence and Error Bound for Perturbation of Linear Programs. *Computational Optimization and Applications*, 13(1-3):221–230, 1999.
- [113] Turbell. *Forward Projection through Voxel Volumes, Ch.5*. PhD thesis.
- [114] M. Vauhkonen, Vadász D., PA. Karjalainen, E. Somersalo, and JP. Kaipio. Tikhonov regularization and prior information in electrical impedance tomography. *IEEE Transactions on Medical Imaging*, 17(2):285–293, 1998.
- [115] M. Wang, W. Xu, and A. Tang. A Unique "Nonnegative" Solution to an Underdetermined System: From Vectors to Matrices. *IEEE Transactions on Signal Processing*, 59(3):1007–1016, 2011.
- [116] S. Weber, C. Schnörr, and J. Hornegger. A Linear Programming Relaxation for Binary Tomography with Smoothness Priors. *Electronic Notes in Discrete Mathematics*, 12:243–254, 2003.
- [117] W. Xu and B. Hassibi. Efficient compressive sensing with deterministic guarantees using expander graphs. *Proceedings IEEE Information Theory Workshop*, pages 414–419, 2007.
- [118] Ming Yan and Luminita A. Vese. Expectation maximization and total variation based model for computed tomography reconstruction from undersampled data. In *In: Proceedings of SPIE, Vol. 7961, Medical Imaging 2011, Physics of Medical Imaging*, 2011.
- [119] D.F. Yu and J.A. Fessler. Edge-Preserving Tomographic Reconstruction with Nonlocal Regularization. *IEEE Transactions on Medical Imaging*, 21(2):159–173, 2002.
- [120] W.P. Ziemer. *Weakly Differentiable Functions*. Springer, 1989.

- [121] Matthias Zisler. Discrete Multilabel Optimization for MAP Estimation of Class Regions in CT Images. Master's thesis, Hochschule Muenchen, 2014.